Influence of 2D Soil Nonlinearity on Basin and Site Responses

AWARD No. **08HQGR0068**

Daniel R.H. O'Connell, Ph.D.
Fugro William Lettis & Associates, Inc.
433 Park Point Drive, Suite 250
Golden, CO 80401
720-836-4880 ext 116 (phone)
720-836-4881 (fax)
oconnell@lettis.com

in collaboration with
Dr. Pengcheng Liu (Bureau of Reclamation, Denver, Colorado)
and
Dr. Luis Fabian Bonilla (Institut de Radioprotection et de Sûreté Nucléaire, B.P.17, 92262 Fontenay-aux-Roses, France, fabian.bonilla@irsn.fr)
03/01/08 through 09/30/09

3 February 2010

Abstract

Basin-edge waves constructively interfere with direct and converted intrabasinal S-waves to produce regions of strongly amplified ground shaking. To investigate how soil nonlinearity might modify basin amplification, 2D P-SV nonlinear horizontal and vertical component ground motions are simulated. The calculations focus on basin and basin-margin regions within several km of the basin-edge, where the largest short-period amplifications are likely to occur. Deep basins (4 km) exhibit strong linear and nonlinear damping of basin-edge waves and relatively small amplification near basin margins. A basin thickness of 1 km is thus used to obtain results relevant for typical shallow urban basins including the San Fernando, Sylmar, and Wasatch-fault-bounded basins. We use the IWTH25 borehole and surface strong motion recordings of the **M** 6.9 2008 Iwate-Miyagi earthquake to show that the 2D P-SV nonlinear model of Bonilla et al. (2006) reproduces the horizontal and vertical peak ground motions and acceleration response spectra of this 4g surface ground motion (Aoi et al., 2008). For moderate input motions (< 0.2 g), the position of basin-edge amplifications are comparable to 2D linear estimates, indicating that 2D and 3D linear basin response calculations combined with 1D nonlinear post-processing can provide realistic estimates of basin-edge responses for distant earthquakes. However, for near-fault motions (> ~0.3-0.5 g), nonlinearity sometimes produces multiple (2-4) regions of horizontal acceleration amplification within 1-2 km of the basin edge, where linear 2D calculations predict only a single region of acceleration amplification. Nonlinear basin-edge amplification can be very sensitive to basin-edge dips and plane-wave incident angles, suggesting that realistic near-fault 3D-basin ground motion simulations need to explicitly incorporate 3D soil nonlinearity. An exception appears to be thin very-low velocity (Vs = 100 m/s) basins, where strong soil nonlinearity for even modest input motions produces responses that are adequately approximated with 1D nonlinear analyses using 3D inputs. Consequently, it appears feasible to remove very-low-velocity basins from 3D calculations and restrict the 3D nonlinear calculations to

portions of the model with stiffer less nonlinear soils. Adaptive mesh refinement (AMR) combined with a 3D linear-nonlinear finite-difference implementation represents a reasonable approach to efficiently and accurately calculate 3D responses in regions containing relatively shallow basins and sedimentary wedges that contain stiff soils.

Acknowledgements

The results of this project were made possible through generous assistance of the following people and organizations that we gratefully acknowledge. Fabian Bonilla developed the original 2D nonlinear finite-difference code and provided the code to the project. Pengcheng Liu modified NOAH2D to include perfectly-matched layer (PML) absorbing boundary conditions and to allow input of incident plane waves over a range of incident angles. The National Information Center for Earthquakes and Disasters, National Research Institute for Earth Science and Disaster Prevention in Japan provided the digital strong-motion data for station IWTH25. Clifford Plumb of the Los Angeles Department of Water and Power (LADWP) provided access and equipment for the acquisition of the surface wave profiles within the Van Norman Complex in northern San Fernando Valley and additional LADWP data documenting San Fernando Valley basin-margin structure. Craig Davis of LADWP authorized and encouraged publication of the Van Norman Complex surface wave investigations. Data were obtained from the ROSRINE website that is sponsored by the Earthquake Hazard Mitigation program of NSF and the California Department of Transportation (Caltrans).

Table of Contents

Abstract i
Acknowledgements ii
1 Introduction 1
1.1 Objectives and Approach 3
2 2D Nonlinear P-SV Wave Propagation Implementation 4
3 Nonlinear Analysis of Soil Station IWTH25 with > 4g PGA 5
3.1 NOAHW 1D SH Analyses 6
3.2 NOAH2D 2D P-SV Analyses 7
3.3 IWTH25 Analysis Conclusions 8
4 2D Nonlinear Basin Responses for ~1 Km-Deep Basins 9
4.1 Influence of Basin-Edge Dip and Plane-Wave Incident Angle 9
4.1.1 Horizontal Responses 11
4.1.2 Vertical Responses 13
5 2D Shallow Low-Velocity Nonlinear Basin Responses 14
5.1.1 2D Peak Velocity and Acceleration Responses 15
6 Conclusions 16
References 17
Project Bibliography 21

1 Introduction

Numerous studies of 3D wave propagation in complex media have focused on calculating the ground motion responses in low-velocity sedimentary basins. Basin-edge waves induced by body and surface waves impinging on basin boundaries can constructively interfere with direct and converted S-waves within basins to produce regions of strongly amplified ground shaking. None of the 3D numerical simulations to date have accounted for soil nonlinearity in basins. There are several reasons nonlinearity has been omitted from 3D calculations of basin responses. First, it's a difficult challenge to integrate linear and nonlinear calculations within a common computational mesh (grid), where the nonlinearity precludes simple post-processing steps like low-pass filtering to eliminate the influences of grid dispersion. Second, such 3D calculations would require large amounts of memory and compute time to obtain ground motion simulations to sufficiently high frequencies of interest (the 1-10 Hz frequency band). However, the large peak horizontal velocities often calculated near the edges of low-velocity sedimentary basins of the order of 100 cm/s imply sufficiently large shear strains (~1% strain) to induce modulus degradation and increased damping in near-surface basin materials.

Linear 3D calculations predict that basin-edge surface and S-waves will strongly interact at critical distances with incident direct S-waves to produce concentrated regions of strong amplification, such as inferred for concentrated regions of damage in the Kobe basin produced by the 1995 Hyogo-ken Nanbu (Kobe) earthquake (Pitarka et al, 1998) and basin-edge focusing in Santa Monica from the 1994 Northridge earthquake (Graves et al., 1998). However, soil nonlinearity can substantially reduce basin amplification and change the locations in a basin were maximum amplifications will occur.
Ignoring pore-pressure effects, there are several ways nonlinear basin soil responses will modify ground motions observed in low-velocity basins. At frequencies <0.5-1 Hz, ground motions are amplified. Thus, it's important to understand nonlinear soil response influences on basin ground motions to obtain appropriate seismic loads for tall buildings and longer-period structures like large bridges. At intermediate frequencies (1-10 Hz), ground accelerations are generally reduced and S-wave propagation velocities reduce with increasing shear strain. These nonlinear soil responses produce variations in S-wave and surface wave propagation velocities in low-velocity sedimentary basins: amplifications vary as a function of frequency and change the positions within the basin where the strongest amplifications occur from the constructive interference of direct and basin-edge shear and surface waves.

Figure 1 schematically illustrates the primary situations of interest in this project. A low-velocity basin is embedded in a higher-velocity rock crustal velocity structure and subject to incident P-SV motion at a range of angles of incidence relative to the basin edge (Figures 1a and 1b). For simplicity, Figure 1 considers the Rayleigh wave generated at the basin edge and incident plane-P-SV wavefields, but ignores basin-edge-generated shear waves. Maximum horizontal-component amplification occurs at the distance from the basin edge where the travel time for the direct shear-wave ($t_{SB}+t_{SRB}$) equals the travel time basin-edge Rayleigh wave ($t_{SRS}+t_R$ in Figure 1a and $t_{SRS}+t_{SRR}+t_R$ in Figure 1b).

One might hope that in the case of waves dominantly incident from the left (Figure 1a), there may be a sufficiently large region within the basin close to the basin edge where maximum short-period amplification occurrence (distances < d_{crit} in Figure 1a) remains relatively linear such that the position of maximum amplification accounting for nonlinear basin responses is quite similar to the position obtained from linear 3D calculations. Then, an efficient strategy could use the 3D linear incident ground motions in 1D or 2D nonlinear site response calculations to calculate realistic 3D nonlinear basin-edge ground shaking responses. In the case of a P-SV wavefield dominated by waves incident from the right in Figure 1b, the size of the basin-edge region where substructure analyses would work is reduced because the direct-shear-wave arrival would precede the basin-edge Rayleigh wave throughout most of the basin. The direct S-wave induces dynamic soil softening and nonlinearity prior to the arrival of basin-edge waves and significantly altering short-period Rayleigh-wave propagation velocities and amplitudes.

Bonilla et al. (2006) presented 2D linear and nonlinear modeling of the responses of the Grenoble basin to vertically incident shear-waves using total stress and the nonlinear soil formulation of Iai et al. (1990). This model follows a multi-mechanism description of the nonlinear soil behavior with its backbone characterized by the hyperbolic equation (Hardin and Drnevich, 1972). The hysteresis follows the Masing criteria (Masing, 1926) with the rheology implemented into a second order staggered grid P-SV finite-difference code. Bonilla et al. (2006) concluded that that the combination of a 2D or 3D basin geometry with nonlinear soil behavior produces a complex basin response, which cannot be predicted by 1D nonlinear studies. Bonilla et al. (2006) focused on a specific, complex basin geometry, so it is difficult to generalize their results to address the specific issues identified in Figure 1. Consequently, we have developed simplified basin geometries and modified the 2D nonlinear P-SV code to propagate horizontal and vertical incident motions over a range of incident angles to specifically evaluate the issues illustrated in Figure 1.

A second class of nonlinear soil issues was recently identified by Aoi et al. (2008). Aoi et al. (2008) analyzed ground motions recorded by the Kyoshin Network (Kik-net) during the **M** 6.9 2008 Iwate-Miyagi earthquake, that included one soil-surface site that recorded a vertical acceleration of 3.8g (station IWTH25). The horizontal borehole and surface motions reported in Aoi et al. (2008) for station IWTH25 are generally consistent with the soil reducing surface horizontal accelerations at high frequencies, as is widely observed at soil sites (Field et al., 1997; 1998; Seed and Idriss, 1970; Beresnev et al., 1995, 2002) and reproducible using 1D nonlinear site response modeling (O'Connell, 2008). However, the surface vertical peak acceleration exceeded 3.8g, exceeding the maximum expected amplification, based on the site velocity profile between the borehole and the surface accelerometers, and current 1D linear or nonlinear theories of soil behavior (O'Connell, 2008). In particular, application of the nonlinear approach of shear-modulus reduction advocated and tested by Bersenev et al. (2002) to predict nonlinear vertical responses, failed to predict peak vertical accelerations in excess of 2g (O'Connell, 2008). Further, Aoi et al. (2008) observed largest upward accelerations at the surface that were 2.27 times larger than the largest downward accelerations, a result not

reproduced using 1D approaches to approximate soil nonlinearity. Since the 2D nonlinear wave propagation implementation of Bonilla et al. (2006) using a plane-strain model (Iai et al., 1990), we investigated if this model could explain the first-order soil responses observed at station IWTH25 using appropriate site-specific estimates of nonlinear soil properties. This investigation is important in the context of the project to determine if the nonlinear implementation of Bonilla et al. (2006) is likely to produce realistic horizontal and vertical ground shaking estimates over the entire range of incident motion amplitudes. In particular, Aoi et al. (2008) reported a change of nonlinear response that was previously unknown. It is possible that there may also be situations where nonlinear horizontal responses depart from current experience (Field et al., 1997; 1998; Seed and Idriss, 1970; Beresnev et al., 1995, 2002) as incident amplitudes increase for particular soil types. Thus, we investigate the station IWTH25 horizontal and vertical ground motions in detail using explicit nonlinear 1D and 2D approaches to evaluate the capabilities of various approaches to reproduce horizontal and vertical soil responses under extreme incident motion amplitudes.

1.1 Objectives and Approach

Our primary objective is to determine computationally-feasible numerical 3D wave propagation strategies that are likely to produce realistic (unbiased) estimates of basin-edge ground shaking responses over the frequency bandwidth of primary engineering interest (0.1-10 Hz). We focus on basin and basin-margin regions within several km of the basin-edge for several reasons. First, the largest short-period (peak acceleration) amplifications are likely to occur near basin margins, in part for the reasons shown in Figure 1. Second, in large deep basins strong linear damping reduces short-period responses of basin-edge Rayleigh and shear-waves as they propagate more than several km from the basin-edge. In large, deep basin strong amplification near the center of the basin occurs at lower frequencies than in shallow basins and peak accelerations are generally limited toward the center of the basin by strong linear and nonlinear shallow damping. Third, smaller basins are more frequently encountered than very large deep basins, so the results of the investigations provide some direct indication of the significance of nonlinear soil responses for a wide range of basins in urban areas including the San Fernando and Wasatch-fault-bounded basins, that typically only extend to 1-3 km depth, as well as other basin regions of interests, such as the basin-edge region near the Seattle fault.

The investigations are organized into three specific calculations sets. The first set if calculations uses 1D and 2D nonlinear approaches to analyze the Kik-net station IWTH25 soil strong motion recording of the 2008 **M** 6.9 2008 Iwate-Miyagi earthquake with a peak vertical acceleration of 3.8 g. A pair of three-component borehole (260 m depth in rock) and surface (in soil) strong motion recordings are available at station IWTH25 as well as a P- And S-wave velocity model between the borehole instrument and the surface (Aoi et al., 2008). Consequently, analysis of this record provides a well-constrained dataset to evaluate the predictive performance of the 2D nonlinear code, particularly the code's ability to reproduce realistic surface horizontal and vertical seismograms and response spectra for soil site conditions under extreme inputs loads.

Results of these calculations show that a standard clay modulus reduction response with a plasticity index of 20-25 can explain both the peak accelerations and acceleration response spectra observed on the horizontal and vertical components at station IWTH25. Consequently, the 2D nonlinear approach of Bonilla et al. (2006) provides a reasonable basis to calculate horizontal and vertical basin response and is used to calculate horizontal and vertical responses for two classes of basins.

In the second set of calculations, we construct 2D basin velocity models with a range of basin-edge dips and plane wave incident angles and calculate horizontal- and vertical-component responses for a wide range of incident P-SV incident amplitudes. Interpretations of these calculations focus on evaluating the feasibility of using simplified combined 3D linear wave propagation with 1D or 2D shallow nonlinear post-processing to accurately predict peak horizontal velocities and accelerations within and outside basins. The third set of calculations uses the results of the IWTH25 investigation to evaluate the response of shallow very low-shear-wave velocity clay-dominated shallow basins than tend to be embedded within larger scale basins like the Salt Lake and Utah Lake basins (Stephenson et al., 2007) to a wide range of incident motion amplitudes. We find that there is a threshold incident wave motion amplitude where peak vertical accelerations begin to become large (> 1g) and continue to increase with increased incident motion amplitude while horizontal peak accelerations become bounded on the order of 0.5 g, indicating that extreme ground shaking behavior similar to that observed at station IWTH25 may occur in other regions. Finally, we outline an integrated 3D numerical approach to efficiently calculate accurate nonlinear ground motion responses in basins. But first, we describe the 2D nonlinear P-SV wave propagation approach that is used in all three sets of investigations.

2 2D Nonlinear P-SV Wave Propagation Implementation

The P-SV nonlinear rheology developed by Iai et al. (1990) was used in the Bonilla et al. (2006) implementation of 2D nonlinear wave propagation. The constitutive equation implemented corresponds to the strain space multishear mechanism model developed by Towhata and Ishihara (1985) and Iai et al. (1990) with its backbone characterized by the hyperbolic equation (Hardin and Drnevich, 1972). The multishear mechanism model is a plane strain formulation to simulate cyclic mobility of sands under undrained conditions. For the calculations in this report, a total stress rheology (pore pressure was ignored) was used in the second order staggered grid P-SV plane-strain finite difference code. Perfectly matched layer (PML) absorbing boundary conditions were used to approximate elastic (transmitting) boundary conditions at the bottom and side edges using an implementation adapted for finite differences from Ma and Liu (2006). Linear hysteretic damping (Q) was implemented using the method of Liu and Archuleta (2006). The horizontal- and vertical component plane waves are inserted in the linear viscoelastic portion of the 2D with a user-selectable range of incident angles.

The San Fernando basin region is one of the focuses of the second set of investigations. A notable characteristic of the M 6.7 1994 Northridge ground motions in the San Fernando basin region is that soil nonlinearity was not as strong as might be expected (Hartzell, 1998; Culterra et al., 1999). Bonilla et al. (2006) performed all their 2D nonlinear basin

calculations using a parameterization for clays with a plastic index (PI) of 20%. They noted that an interesting property of clays is that their dynamic properties depend on the plastic index. Thus, they could use the same shear modulus reduction curve at all depths within basin sediments. We employ the same approach and use a depth-independent clay parameterization with a PI of 20% because it produces basin soil amplifications ratios relative to rock that are consistent with Northridge earthquake estimates of nonlinear amplification (Hartzell, 1998; Field et al., 1997; 1998) and the observations of generally less nonlinear soil response than as might be expected based on standard models of depth-dependent modulus degradation and damping (Silva et al., 1998; Culterra et al., 1999). Ironically, a PI of 20% depth-independent nonlinear parameterization also appears to explain the large, asymmetric vertical peak accelerations observed at station IWTH25, as is further discussed in Section 3. Finally, this parameterization is also used to evaluate extremely low-velocity (Vs of 100 m/s) shallow basin responses; if strong nonlinear damping is observed for this nonlinear scenario, then it is likely to be observed for most nonlinear soils.

3 Nonlinear Analysis of Soil Station IWTH25 with > 4g PGA

The 1994 M 6.7 Northridge earthquake has been the focus of numerous evaluations of nonlinear soil responses (Trifunac and Todorovska, 1996, 1998; Beresnev et al., 1998; Field et al., 1997, 1998; Hartzell, 1998; Silva et al., 1998; Hartzell et al., 2004). While there have been extensive shallow investigations in support of nonlinear soil response research (ROSRINE), the Northridge strong motion data set lacks the combination of deep downhole and surface recordings required to separate nonlinearity from apparently nonlinearity associated with scattering (O'Connell, 1999; Hartzell et al., 2005). In contrast, the Kyoshin Network, or Kik-net, in Japan (Fujiwara et al., 2005), has recorded numerous earthquakes with ground motion data recorded at surface and at depth in underlying rock and soil. Of particular interest for these nonlinear investigations is the recording at Kik-net station IWTH25, where a 3.8g peak vertical acceleration was recorded (Aoi et al., 2008). Analyses of the combined downhole and surface ground motions from IWTH25 provide an opportunity to evaluate several strategies to estimate vertical ground motions since a P- and S-wave velocity profile is available to the bottom of the borehole at 260m (Aoi et al., 2008).

Station IWTH25 is located in a region of rugged topography adjacent to a high-gradient stream channel on a fluvial terrace (Figure 2). The topography reflects the station's hangingwall location relative to the fault (Figure 3). Station IWTH25 is located near a region of large slip along strike and updip of the hypocenter (Figure 3). Consequently, IWTH25 is subjected to significant rupture directivity and near-fault radiation associated with strong gradients of slip and rupture velocity on the portions of the fault close to the station (Miyazaki et al., 2009). The IWTH25 ground motion has been of particular interest because of the extreme peak vertical acceleration (3.8g) and peculiar asymmetric amplitudes distribution of the vertical accelerations (Aoi et al., 2008; O'Connell, 2008; Hada et al., 2009; Miyazaki et al., 2009; Yamada et al, 2009a); the upward vertical acceleration is much larger than the downward direction, although in the borehole record at a depth of 260 m at the same site, the upward and downward accelerations have symmetric amplitudes (Aoi et al., 2008). Aoi et al. (2008) propose a conceptual model for

this asymmetry. Their model uses a loose soil with nearly zero confining pressure near the surface. The soil particles separate under large downward acceleration, and in this quasi free-fall state, the downward accelerations at the surface only modestly exceed gravity. Conversely, large upward accelerations compact the soil and produce much larger upward accelerations. Aoi et al. (2008) report three cases of these anomalous large vertical acceleration amplifications in a search of 200,000 strong motion recordings. Hada et al. (2009) successfully reproduce the strong vertical asymmetric accelerations at IWTH25 with a simple 1D discrete element model, a model that is not a rigorous model of wave propagation. Yamada et al. (2009a) interpret the large upward spikes in acceleration as slapdown phases, which are also typically observed in near-field recordings of nuclear explosion tests. Our focus here is not the asymmetry of the IWTH25 vertical accelerations recorded at the surface, but determining if the simple total stress plane-strain model of soil nonlinearity in Bonilla et al. (2006) can reproduce both the first-order peak horizontal and vertical velocities and accelerations and acceleration response spectra at station IWTH25 using the borehole motions at 260 m depth as inputs.

We perform three sets of calculations. First we use the NOAHW 1D SH nonlinear finite-difference code (Hartzell et al., 2004) to evaluate if a simple 1D model obtained by perturbing the 1D model from Aoi et al., 2008) (Figure 4) combined with standard soil curves from EPRI (1993) (Figure 5) reproduces the observed horizontal-component surface responses using the borehole motions at 260 m depth as inputs. Second we use an approach similar to Beresnev et al. (2002) with the NOAHW 1D nonlinear finite-difference code (Hartzell et al., 2005) to evaluate if vertical motions can be modeled as nonvertically propagating SV waves. In the case of station IWTH25, this strategy is not successful because a substantial proportion of the vertical accelerations are associated with frequencies > 10 Hz, a frequency band where Beresnev et al. (2002) conclude that acoustic waves dominate vertical responses. In the third and final set of IWTH25 calculations we use the plane-strain P-SV 2D modeling approach of Bonilla et al. (2006) to propagate the borehole horizontal and vertical component motions from 260 m depth to the surface.

3.1 NOAHW 1D SH Analyses

The NOAHW 1D SH calculations provide a good fit to the horizontal acceleration response spectra and acceleration seismograms for the north component (Figure 6). The synthetic north and east responses in the 0.5-2 Hz frequency range exceed the observed responses suggesting that the EPRI (1993) curves (Figure 5) are not the best choice to reproduce broadband nonlinear responses at the site. The synthetic east response does not reproduce the peak responses in the 8-10 Hz range and also overpredict the 0.5-2 Hz responses (Figure 7). However, the NOAHW 1D synthetic surface horizontal motions reasonably reproduce the reduction in dominant amplitude frequency responses from the borehole motion to the surface and the overall horizontal surface spectral shapes and amplitudes reasonably well (Figures 6b and 7B). In particular, the synthetic horizontal acceleration seismograms reproduce the peak amplitudes and amplitude duration characteristics of the observed horizontal accelerations quite well (Figures 6a and 7a). In contrast, the NOAHW synthetic results for the vertical component show that the surface vertical motions are not dominated by shear-wave responses, since 1D SH nonlinear

synthetic vertical approximation substantially underpredicts high-frequency spectral accelerations and overall seismogram amplitudes, and overestimates the frequency shift as the vertical motions propagate from the base of the borehole to the surface (Figure 8). This vertical synthetic result is expected because of the proximity of IWTH25 to a reverse-fault (Figure 3) that produced a wavefield that is P-SV dominated and incident on a shallow velocity structure that would produce strong SV-P conversions (Beresnev et al., 2002). Consequently, the P-SV 2D calculations are performed to further evaluate the IWTH25 vertical responses.

3.2 NOAH2D 2D P-SV Analyses

Yamada et al. (2009b) conducted geophysical investigations at the site and found lower velocities in the top several meters than reported in Aoi et al. (2008). The trail-and-error modeling used to obtain the refined velocity model in Figure 3 is consistent with the results of Yamada et al. (2009b); the lower-velocity first layer in Figure 4 was required to produce the maximum horizontal spectral responses observed near 10 Hz in Figures 6a and 7a. The geologic environment at station IWTH25 will clearly produce lateral changes in shallow velocity structure. In particular, the hangingwall uplift associated with repeated faulting similar to the 2008 earthquake will produce a series of uplift terraces adjacent to the stream in Figure 2, with the lowest shallow velocities being found on the lowest terrace adjacent to the stream, where station IWTH25 is located. The width of the stream and lowest terrace is about 100m near station IWTH25 (Figure 2).

We constructed a 2D velocity model by including a region 100 m wide with velocity layer 1 in Figure 4 and then extending velocity layer 2 to the free surface in the region surrounding the 100 m low-velocity surface layer 1. Station IWTH25 is assumed to be located relatively close (4-5 m) to the lateral velocity change within the low-velocity layer 1 portion of the 2D velocity model because the geologic log from station IWTH25 indicates a only 1-2 m of young terrace deposits (Aoi et al., 2008), but the youngest terrace probably extends across and encompasses the stream channels and their margins (Figure 2). The dominant large-amplitude arrivals in the borehole motions are associated with large slip regions below and just south of station IWTH25 (Figure 3). Consequently, a plane-wave incident at 80 degrees from the south was used to propagate the borehole motion to the surface in the 2D model. In the context of Figure 1, the simulated surface motions at IWTH25 correspond to the case of Figure 1b, where the plane wave is incident from the far side of the lateral velocity change closest to the station.

The NOAHW 1D results suggested that the EPRI (1993) curves may be too nonlinear (Figures 6 and 7). For the NOAH2D calculations the nonlinear properties were simplified to a depth-independent PI of 20%. The less nonlinear parameterization tended to reduce the large synthetic amplification at lower frequencies (0.5-2 Hz) obtained using the EPRI (1993) curves, but resulted in moderate underdamping at frequencies > 10 Hz on the horizontal components (Figures 9 and 10). Overall the 2D synthetic nonlinear horizontal motions provide a good fit to the acceleration response spectra (Figures 9a and 10a) and acceleration seismograms (Figures 9b and 10b). The 2D synthetic horizontal velocities match the observed velocity seismograms well, except in the early portion of the record

where the translation ("fling") associated with permanent displacement that dominates early portions of the observed seismograms (Figures 9c and 10c).

Synthetic vertical responses were calculated for each horizontal-vertical component pair which is a crude approximation to total 3D wavefield. The east component is nearly fault-normal and has the largest peak accelerations and velocities of the two horizontal components, so the east-vertical combination probably best corresponds to the dominant P-SV responses. Except for the obvious asymmetry in both the acceleration and velocity vertical seismograms, both the north-vertical and east-vertical 2D nonlinear synthetic vertical surface motions provide a good fit to the observed acceleration response spectra (Figures 11a and 12a), acceleration seismograms (Figures 11b and 12b), and velocity seismograms (Figures 11c and 12c). Figures 13 and 14 illustrate that somewhat reduced fitting quality is observed the incident angle is switched to correspond to energy from the north, with increasing misfits in the spectral accelerations and velocity seismograms. While this scenario does not correspond to the direction of dominant energy (Figure 3), it illustrates the sensitivity of the synthetic responses to moderate changes in incident angle and direction. Since station IWTH25 is located in the deformed hangingwall of a reverse fault in rugged topography, it is clear that even these 2D nonlinear calculations are a crude approximation to the field conditions and complex incident wavefield associated with the finite fault rupture. However, the 2D nonlinear calculations summarized in Figures 9-12 for station IWTH25 clearly show that the 2D P-SV nonlinear approach of Bonilla et al. (2006) provide a sound basis to evaluate first-order nonlinear horizontal and vertical nonlinear responses, even for cases of extremely large incident accelerations and velocities.

3.3 IWTH25 Analysis Conclusions

It is important to mention some factors that are not explicitly accounted for in the approach of Bonilla et al. (2006). Goldberg (1960) was among the first to theoretically show the interaction between P and S waves in an elastic medium for large-amplitude seismic waves. His solution yielded the following results: (1) P- and S-waves couple, (2) S waves induce P waves, (3) the induced waves have a dominant frequency twice the S-wave frequency, (4) the induced P waves propagate ahead with P-wave velocity. Loukachev et al. (2002) develop a mechanism to explain the frequency dispersion in the P-wave spectra relative to S-wave spectra due to the interaction between compressional (P) and shear (S) waves in granular materials. Shear waves induce dilatancy and contractancy in granular materials which produces longitudinal dilatancy waves (so-called D waves) with approximately double frequency. The results of Goldberg (1960) are sufficient to partially explain the frequency doubling of the dominant vertical resonance frequency even if the IWTH25 material does not exhibit granular dilatancy and is dominated by relatively clay responses. However, it appears more likely that the IWTH25 responses reflect a combination of large-amplitude P-S-wave linear coupling combined with the nonlinear dilatant material responses predicted by Loukachev et al. (2002) for granular soils. This may explain the broad frequency bandwidth (9-18 Hz) of large vertical spectral response. Even with these caveats, the synthetic results illustrated in Figures 9-12 show that the approach of Bonilla et al. (2006) clearly provides a sound basis to evaluate first-order nonlinear horizontal and vertical response in basins.

4 2D Nonlinear Basin Responses for ~1 Km-Deep Basins

Initial investigations indicated that the basin-edge nonlinear responses of deep basins (> 3 km) were dominated by shallow 1D nonlinear responses. In general it does not appear necessary to consider 3D nonlinear basin responses for deep basins. However, there are many instances of shallower basins in urban areas (as noted in Section 1.1) that have total low-velocity basin depths on the order of 1-2 km, including the San Fernando, Salt Lake, and Utah Lake basins. The 2D nonlinear basin response investigations in this section focus on 2D velocity models constructed with a 1 km total basin depth.

4.1 Influence of Basin-Edge Dip and Plane-Wave Incident Angle

We construct several simple basin geometries and velocity structures (Figure 15) to span a range of reverse and normal-faulting basin-edge configurations. The reverse-faulting basin-edge configurations were constructed based on data from the San Fernando basin. Inspection of multiple 60-fold proprietary seismic reflection data and water well logs (Cliff Plumb, pers. comm., 2009) showed that the Verdugo fault along the northeastern margin of the San Fernando Basin juxtaposes basement rocks similar in composition to the rocks downstream of Paicoma Dam against Quatenary Saugus basin sediments and soft rock over a depth range of 0.5-1 km with nearly a vertical interface over portions of the basin. In addition to providing a good representation of the northeast San Fernando Valley structure adjacent to the Verdugo fault, the vertical basin edge is used as the simplest case and a base of reference (Figure 15a). The 60-degree-dip reverse faulting configuration is based on the northern edge of the San Fernando basin, where the Mission Hills reverse fault has at least 1.6 km of throw (Tsutsumi and Yeats, 1999; Figures 15b and 16b), which juxtaposes higher-velocity basement and Tertiary rocks in the hangingwall against lower-velocity Quaternary Saugus basin sediments and soft rock (Figure 16).

A total of 16 new surface wave surveys that imaged shear-wave velocities to depths of 100-200 m were obtained in the Los Angeles Department of Water and Power (LADWP) Van Norman Complex (An example is shown in Figures 16a and 17). The surface wave data were acquired with a linear geophone array using active seismic sources located just beyond each of the geophone arrays. This data acquisition approach was designed to exploit seismic interferometric methods (O'Connell, 2007; Snieder et al., 2009) to extract broadband surface wave waveforms from noise and active source data. The interferometric multi-channel analysis of surface waves (IMASW) approach constructs noise correlation function (NCF) waveforms from the multiple recordings of background noise and random impact sources. The NCFs are processed with narrow-band filters to allow picking of phase velocities using constant phase tracking of peaks, zero crossings, and troughs across record sections and narrow-band quadrature filters to create envelope functions to pick group arrival times and estimate group velocities. The NCF waveform processing improves resolution of low-frequency phase and group velocities relative to slowness-frequency image processing, which increases the maximum depth resolution of shear-wave velocities (Figures 16a and 17). The frequency bandwidth of well-resolved phase velocities varies over the frequency range of 2Hz to 80 Hz, with most IMASW lines obtaining good resolution of phase and group velocities in the 4 Hz to 40 Hz frequency band. One profile (IMASW Line 16) constrained shear-wave velocity contrasts

across the Mission Hills fault (Figures 16a and 17) and the upper member of the Quaternary Saugus Formation in the San Fernando basin (Figure 16).

These IMASW data were used to construct the velocity profiles for the basin portions of the 2D velocity models shown in Figure 15. For simplicity, we omitted the thin surficial sediments from the hangingwall of the Mission Hills fault to provide a clear distinction between linear and nonlinear responses across the basin edge. The shallow rock velocities from the Paicoma Dam downstream suspension logging where used to define the linear rock velocity portion of the 2D model (red regions in Figure 15). A constant velocity linear rock region was used to focus on the influence of basin edge geometries on surface ground motion responses. The reverse-faulting basin edge model (Figure 15b) is also similar to the basin-edge model developed by Graves et al. (1998) to model amplification near Santa Monica from the 1994 Northridge earthquake. The velocity structure in Figure 15b is also quite similar to the base-edge velocity structure used by Hallier et al. (2008) to model base-edge waves from the 1995 Hyogo-Ken Nanbu earthquake, with the same basin surface shear-wave velocity (300 m/s) used in Figure 15 and in Hallier et al. (2008).

The normal-faulting basin velocity model (Figure 15c) is also a reasonable approximation to the shallow basin-edge shear-wave velocity structure for the Salt Lake and Utah Lake basins measured by Stephenson et al. (2007) for several sites, including their sites FFT, SD, SFCE, SOGC, although Figure 15c omits the slowest top 5-10 m of material with shear-wave velocities < 300 m/s measured at some of these sites in Stephenson et al. (2007); the influence of these lowest velocity regions is considered in Section 5. An average basin depth of 1 km is a reasonable approximation for these two basins (Olsen et al., 1995). In Figure 15, near-surface shear-wave attenuation was approximated with a Q model based on low-strain damping estimated by Gibbs et al. (1999) from borehole sites in the Van Norman Complex that did not have bedding dips exceeding 45 degrees (to avoid biases associated with strong direct shear-wave refraction/reflection in the interpretation of the borehole data).

The downstream Paicoma Dam strong motion recording of the M 6.7 Northridge earthquake provides good horizontal and vertical motions to use as incident motions (Figure 18). The waveforms are relatively simple (Figures 18a to 18d) with two main pulse of energy and a relatively short duration of shaking, consistent with measured site shear-wave velocities > 2 km/s (ROSRINE site PAC). The 275 degree horizontal component has the dominant directivity response and wave selected along with the vertical component from station PAC as the inputs for all P-SV calculations. Both components have there dominant amplitude responses at frequencies < 3 Hz (Figures 18e and 18f), which make the motions in Figure 18 particularly well suited as inputs to evaluate basin-edge responses that are generally dominated by < 4 Hz shear- and surface-wavefields, and in particular by the maximum frequency of the basin Rayleigh-wave Airy phase (Hallier et al., 2008).

The 2D velocity models in Figure 15 were discretized using a 4 m grid spacing to obtain results free of significant grid dispersion to maximum frequency of < 6 Hz for the linear calculations and to < 2 Hz for the most nonlinear calculations. The grid spacing was

reduced to 1 m for one of the most nonlinear calculations to check and ensure that the overall spatial and amplitude patterns obtained using the 4 m grid spacing were not significantly influenced by grid dispersion for frequencies < 25 Hz. Consequently, a 25-Hz low-pass filter was used to post-process all the 4-m grid results to determine peak velocities and accelerations. Peak velocities and accelerations are plotted as a function of amplitude color-coded by the corresponding linear rock amplitudes and as amplitude ratios relative to linear rock as a function of amplitude color-coded by the corresponding linear rock amplitudes.

4.1.1 Horizontal Responses

Peak horizontal velocity (PHV) exhibits a significant dependence on basin-edge dip and plane-wave incident angle. For instance, the maximum basin PHV occurs at about the same position of ~0.5 km for the vertical basin edge (Figure 19a); nonlinearity has the strongest amplification influence furthest from the basin edge (Figure 20a). In contrast, for the 60-degree dipping reverse-fault basin-edge geometry, the position of maximum PHV moves from ~0.2 km to ~0.4 km from the basin edge as incident amplitude increases (Figure 21a); nonlinearity has a stronger influence on PHV amplification closer to the basin edge (Figure 22a). As basin edge dip decreases for the normal-faulting basin edge configuration, the position of maximum PHV moves further from the basin edge (Figures 23a, 25a, and 27a). The 35-degree basin edge exhibits stronger nonlinear amplification within 0.5 km of the basin edge (Figure 28a) than either the 45-degree (Figure 26a) or 60-degree (Figure 24a) basin-edge configurations.

The influence of incident angle on PHV amplitudes is illustrated for a vertical basin-edge by the difference in basin edge PHV variations between a plane-wave incident from the left or linear basin-edge side (Figure 29a) and a plane-wave incident from the right or the nonlinear basin side (Figure 31a) for the basin region with 0.5 km of the basin edge. The plane-wave incident from the linear edge of the basin exhibits much stronger nonlinear PHV amplification close to the basin edge (Figure 30a) than the plane-wave incident from the basin side (Figure 32a), consistent with the first-order influence of incident wave direction in Figure 1. For the 60-degree-dipping reverse fault basin edge, plane-wave incident direction strongly influences nonlinear PHV distribution near the basin margin with the largest PHV located 0.8-0.9 km from the basin edge when the plane-wave is incident from the basin side (on the right) although a second region of large PHV develops with 0.1 km from the basin margin as incident amplitude increases (Figure 33a). The vertically-incident plane wave produces maximum PHV within 0.2 km of the basin edge for linear and small amplitudes but shifts the region of maximum PHV to ~0.5 km from the basin edge as amplitude increases (Figure 21a). The strongest nonlinear amplification occurs for vertical incidence with 0.2-0.3 km of the basin margin (Figure 22a), but occurs 0.8-0.9 km from the basin margin when the plane-wave is incident from the basin side (Figure 34a), a result that is inconsistent with the postulated influence of incident wave direction on nonlinear amplification outlined in Figure 1. Thus, while the first-order amplification behavior illustrated in Figure 1 explains nonlinear PHV amplification patterns for a vertical basin edge, it makes an incorrect prediction for the case of a 60-degree reverse faulting basin edge geometry.

Peak horizontal acceleration (PHA) nonlinear responses are more complex within 2 km of the basin edge than PHV nonlinear amplifications. For instance, for the vertical basin edge and vertical incidence, linear amplification produces two regions of local PHA amplification in the basin at distances of 0.2 km and 0.4-0.6 km, but as the linear rock PHA increases from 0.24g to 0.32g a third region of large basin amplitudes develops in the region < 0.1 km from the basin edge (Figure 19b). Nonlinear PHV amplification exceeds linear basin amplification close to the basin edge (Figure 20b). For the 60-degree dipping reverse fault basin-edge configuration and vertical incidence, the position of maximum PHA shifts toward the basin edge as incident amplitude increases (Figure 21b) and nonlinear PHA amplification is a stronger function of distance from the basin edge than incident amplitude (Figure 22b).

As basin edge dip decreases for the normal-faulting basin edge configuration, the position of maximum linear PHA moves further from the basin edge, but nonlinear PHA moves toward the basin edge as incident amplitudes increase (Figures 23b, 25b, and 27b). Nonlinear PHA amplification is quite sensitive to normal-faulting basin edge dip; the 35-degree nonlinear PHA amplification is nearly independent of distance from the basin edge (Figure 28b), but the 45-degree nonlinear PHA amplification is nearly linear in the 0.2-0.3 km distance from the basin edge (Figure 26b) where the maximum PHA occurs for linear rock accelerations > 0.24 g (Figure 25b). In contrast, the 60-degree dip normal faulting basin-edge configuration shows a rather smooth increase in amplification nonlinearity with increase from the basin edge (Figure 24b).

Incident angle has a moderate influence on nonlinear PHA for the vertical basin edge geometry. In all three incident angles used (vertical, 77 degrees from the linear side, and 76 degrees from the nonlinear basin side) a characteristic pattern of three modes of large PHA develop as incident amplitude increases (Figure 19b, 29b, and 31b). The largest PHA occurs furthest from the basin edge for the plane wave incident from the basin edge (Figure 29b); the largest PHA occurs close to the basin edge for vertical incidence (Figure 19b) and incidence from the linear side (Figure 31b), consistent with the first-order hypothesis that waves incident from the basin side will have the earliest onset of nonlinear amplification and therefore somewhat lower overall PHA than for waves incident from the linear side of the basin edge (Figure 1). The PHA nonlinear amplifications exceed linear amplifications in the region < 0.1 km from the basin edge (Figures 20b and 30b) for vertical incidence and waves incident from the left linear region, but do not for waves incidence from the right nonlinear basin side (Figure 32b), consistent with the first-order predictions of Figure 1.

For the 60-degree-dipping reverse fault basin-edge geometry with the plane-wave incident at 76 degrees from the basin on the right the two main regions of large linear PHA separate into four regions of locally large PHA spread over a region extending about 1 km from the basin edge (Figure 33b). In contrast, the vertically-incident PHA distribution for the same basin edge configuration exhibits two large PHA regions within 0.6 km of the basin edge (Figure 21b). The basin position of PHA is a strong function of incident amplitude for the plane wave incident from the basin side on the right (Figure 34b) with the largest amplification occurring 0.8-0.9 km from the basin edge for linear

rock PHA < 0.25 g, but remains always close to the basin edge and moves toward the basin edge as incident amplitude increases for the vertically-incident plane wave (Figure 22b), which is consistent with the first-order approximation in Figure 1.

The overall horizontal nonlinear PHV and PHA basin-edge amplification results are sometimes consistent with the simple plane-wave incident angle dependence illustrated in Figure 1. However, there are significant exceptions that show that the overall nonlinear basin amplification characteristics are also quite sensitive to basin-edge dip geometry in sometimes complex ways. The three normal-faulting basin edge dip results illustrate the sometimes extreme sensitivity of PHA amplification on basin edge dip, with local regions of nearly linear amplification within the basin for all incident amplitudes for one dip (Figure 26b) that are not observed for steeper or shallower dips (Figures 24b and 28b). The PHV and PHA basin-edge amplification results (Figures 19-34) indicate that basin amplification within 1-2 km of the basin edge is a complex nonlinear function of basin-edge dip and plane-wave incident angle. Consequently, these results suggest that for shallow basins, a 3D nonlinear approach to estimate basin responses is necessary to predicted horizontal amplification in the basin edge region of relatively stiff soil shallow basins.

There are several configurations where nonlinear super amplification on the order of 20% occurs in the linear material within 0.3 km of the basin edge, particular for the vertical basin-edge configurations (Figure 20, 30, and 32) and to a smaller degree for the steeper (60-degree) dipping normal (Figure 24) and reverse (Figure 22) configurations. The 60-degree dip reverse-faulting basin-edge configuration primarily amplifies PHV (Figure 22). The 60-degree normal-faulting basin-edge configuration produces only small (< 10%) amplification on the linear side of the basin edge (Figure 24). However, there are clearly some basin-edge configurations where nonlinear basin responses may lead to significant amplification in high velocity, relatively linear sites adjacent to the nonlinear basins. For instance, a portion of the amplification (or alternatively less nonlinear amplification) observed at the Rinaldi (RIN) site located on the hangingwall several hundred meters from the Mission Hills reverse fault (Cultrera et al.,1999) may be a result of amplification introduced by the nonlinear responses in the adjacent basin (Figure 16b).

4.1.2 Vertical Responses

Vertical peak velocity (PVV) and peak acceleration (PVA) responses are substantially simpler than the horizontal PHV and PHA responses. Generally, in the region < ~0.3 km from the basin edge, nonlinearity moves the positions of maximum PVV and PVA toward the basin margin as incident amplitude increases (Figure 35). Relative to linear amplification, nonlinearity smoothes vertical PVV and PVA amplification patterns in the region > ~0.5 km from the basin margin (Figure 36). This behavior generally holds true independent of incident wave direction and basin-edge dip (Figures 35-50), with a mild exceptions for the normal-faulting basin-edge configurations, where the nonlinear amplifications become somewhat more complicated than the linear amplifications for small incident amplitudes (Figure 40, 42, and 44). Thus, almost everywhere in the basin except with 0.3-0.4 km from the basin edge, a smoothed linear amplification provides a reasonable approximation to PVV and PVA amplification. Within 0.3-0.4 km of the basin

edge, nonlinear PVA amplification is more pronounced than PVV amplification in most cases (Figure 36, 38, 40, 42, 44, 46, and 48), but in the case of the 60-degree-dipping reverse fault with the plane-wave incident from the basin side to the right PVV amplification exhibits more nonlinearity than PVA amplification (Figure 50).

Even though 2D vertical basin amplification responses are not as complex as the horizontal responses in Section 4.1.1, the model results of Section 3 suggest a 3D nonlinear modeling approach will appropriately account for nonlinear effects on vertical peak velocities and accelerations that are likely to be important near the edges of basins. In particular, the vertical nonlinear results show that the linear amplification approximation is likely to overestimate vertical velocity and acceleration amplifications near the edge of basin by 20-30% in some cases and actually underestimate vertical peak velocities near steeply-dipping basin-edge configurations. Thus, although the 2D vertical nonlinear results do not in themselves argue strongly for considering 3D nonlinear ground motion modeling, in combination with the horizontal nonlinear amplification results of Section 4.1.1, a 3D nonlinear basin modeling approach is clearly necessary for shallow basins with relatively stiff soils to estimate realistic basin amplifications within 1-2 km of the basin edge.

5 2D Shallow Low-Velocity Nonlinear Basin Responses

The previous 2D calculations did not consider basins with very low shear-wave velocities on the order of 100 m/s. Lomnitz et al. (1999) showed that long duration monochromatic ground motions may be produced in basins that have low shear-wave velocities (0.1 to 0.2 km/s) and saturated sediments. To test the ability of such a long duration mode to persist in a basin with strong intrinsic attenuation, O'Connell and Ake (2010) constructed a model of a small (0.3 km wide and 0.1 km deep) glacial scour embedded in a 2D model with slightly higher shallow velocities outside the basin and higher velocities at depth to roughly correspond to conditions near Jackson Lake Dam in Wyoming (Figure 51a based on O'Connell et al., 2003). These linear 2D finite-difference calculations used values of Q=10 to simulate high-intrinsic attenuation in the near-surface, low-velocity materials. P-wave velocities were set to water velocities for the lowest velocity materials. The 2D version of the elastic finite-difference program E3D (Larsen and Grieger, 1998), which includes viscoelastic capabilities implemented using the approach of Robertsson et al. (1994), was used to calculate the seismic response of a SV plane-wave incident at 5 degrees from vertical upon the basin with a total moment of 10^{20} dyne-cm to roughly correspond to the amplitudes associated with microearthquakes recorded by three-component broadband seismographs near Jackson Lake Dam (O'Connell et al., 2003). The numerical model was 8 km long and 5 km deep with attenuating boundaries to minimize spurious internal reflections. The source-time function was a differentiated 0.75 s-duration Gaussian pulse. The incident horizontal velocity response is shown at the bottom of Figure 51b.

Constructive interference at the center of the basin produces maximum amplitudes that persist for ~7 s and a slow amplitude decay lasting about 20 s (Figure 51b). Sites offset from the center of the basin experienced long-duration monochromatic horizontal motions with slowly decaying amplitudes that persisted to the maximum calculation time

of 60 s. The long duration responses are produced by the interface modes propagating horizontally back and forth across the basin as they reflect off the vertical boundaries at the basin edges (Figure 51). Ground motion responses similar to the top time history in Figure 51b were observed for a M 3.7 earthquake recorded in very low-shear wave velocity sites near Jackson Lake, Wyoming (O'Connell et al., 2003). This mode can persist for relatively long durations with little attenuation, even though intrinsic attenuation is high.

To more realistically evaluate the lateral scale of extremely low-velocity deposits near Jackson Lake Dam, the lowest-velocity region in Figure 51 was expanded to have a width of 2 km. A constant PI of 20 with depth nonlinear parameterization, the same nonlinear parameterization used in Sections 3 and 4, was used to roughly represent the lacustrine clay-dominated sediment nonlinear properties near the dam within the portion of the velocity model that has shear-wave velocities < 0.5 km/s in Figure 51a. At Jackson Lake Dam pore pressure is likely to be a significant issue (O'Connell et al., 2003). However, for simplicity, all 2D nonlinear computations are total stress analysis, which means that pore pressure effects were neglected so first-order of effects of nonlinearity for typical near-fault incident motion can be evaluated. Initial NOAH2D calculations were performed with a grid spacing of 0.5 m to establish the influence of grid dispersion on estimated peak velocities and accelerations. These tests showed that a grid spacing of 2m combined with a lowpass filter corner frequency of 15 Hz provided peak amplitude results relatively unaffected by grid dispersion. Vertical incidence and incidence at 81 degrees were used with the scaled horizontal and vertical Paicoma Dam ground motions (Figure 18) as the input motions. 2D nonlinear results were computed for four different input motion scale factors to span the range from small to large near-fault loading levels.

5.1.1 2D Peak Velocity and Acceleration Responses

The vertical incidence horizontal responses exhibit strong nonlinear amplification even for input motions corresponding to linear rock responses of 0.08g and 9 cm/s (Figure 52). Where the linear 2D calculations indicate regions of large PHA nearly the basin edges as well as the central portion of the basin, the nonlinear responses reduce PHA to nearly constant levels on the order of 0.1g throughout most of the basin (Figure 52). Only for the smallest incident motion does any significant remnant PHA amplification persist, as indicated by the linear calculations near the basin edges (Figure 53). There are subtle differences in the horizontal PHV and PHA responses within the basin due to phase difference of the wave propagation along the two basin edges, but in general the horizontal PHV and PHA responses are nearly symmetric as expected for vertical incidence (Figures 52 and 53).

The corresponding vertical nonlinear PVV and PVA responses are substantially simpler than the corresponding linear variations of PVV and PVA within the basin (Figure 54). The strong PVV and PVA amplification near the basin edges in the linear calculations are replaced by nearly constant nonlinear amplification throughout most of the basin that is essentially independent of incident amplitude (Figure 55). Nonlinearity confines strong vertical amplification to the small regions at the basin margins (Figure 55). In contrast to the horizontal responses, vertical amplification within the basin near the margins is

sensitive to wave polarity relative to the basin margins, with higher and lower amplitudes (Figure 54) and amplification (Figure 55) located between the high-low-velocity and low-high-velocity margins.

The 81-degree incident plane-wave simulations show that non-vertical incidence produces only modest differences in PHV and PHA variations between the two basin-margin regions and that nonlinearity strongly limits peak amplitudes within most of the basin (Figure 56). The larger input motions are more heavily damped by nonlinearity, but overall nonlinear amplification symmetry within the basin is only slightly perturbed by the inclined incident plane-wave (Figure 57). In contrast, the vertical responses exhibit stronger asymmetry within the basin, with PVV exhibiting the strongest asymmetry (Figure 58). The strongest amplification asymmetry is only produced by the strongest incident motion and the primary impact is on PVV (Figure 59).

Overall, for soils comparable to or less linear than clays with a PI of 20, these nonlinear 2D results suggest that combining the outputs of 2D or 3D simulations that omit the very-low-velocity basin with 1D nonlinear analyses to account for the very-low-velocity basins using approaches like NOAHW would produce comparable amplifications within the basin to full nonlinear 2D or 3D analyses. Linear 1D P-SV vertical analyses in the center of the basin would provide appropriate vertical amplifications throughout most of the basin. Thus, it appears that it may be feasible in most cases to omit very-low-velocity basins from 3D linear or nonlinear analyses and use the outputs from these analyses with simplified 1D nonlinear SH and P-SV nonlinear amplification calculations to estimate realistic horizontal and vertical peak velocities and accelerations within very-low-velocity basins. For the immediate basin margin regions, linear 2D or 3D calculations appear to provide a good first-order estimate of horizontal and vertical amplifications.

6 Conclusions

For practical reasons, the calculations presented in this report represent only a small subset of possible nonlinear soil conditions, basin-edge geometries, and incident wave angles. Additional calculations were performed for each set of investigations represented in Sections 3-5 to evaluate the sensitivity of the results to changes in nonlinear soil properties that are not presented here. The primary findings from these calculations are that relatively stiff soils are required to produce the nonlinear response complexity illustrated in Section 4. When soils are relatively weak, nonlinear responses become less complex. Consequently, the primary conclusions presented here apply to stiff soils, like those found in significant portions of the urban environment of southern California (Silva et al., 1998; Cultrera et al., 1999) and portions of the basins adjacent to the Wasatch fault.

However, sufficient results are obtained to provide some important conclusions. For moderate input motions (< 0.2 g), the position of basin-edge amplifications are comparable to 2D linear estimates, indicating that 2D and 3D linear basin response calculations combined with 1D nonlinear post-processing can provide realistic estimates of basin-edge responses for distant earthquakes. However, for near-fault motions (> ~0.3-0.5 g), nonlinearity sometimes produces multiple (2-4) regions of horizontal acceleration amplification within 1-2 km of the basin edge, where linear 2D calculations predict only

a one or two region(s) of horizontal acceleration amplification. Nonlinear basin-edge amplification can be very sensitive to basin-edge dips and plane-wave incident angles, suggesting that realistic near-fault 3D-basin ground motion simulations need to explicitly incorporate 3D soil nonlinearity. An exception appears to be thin very-low velocity (Vs = 100 m/s) basins, where strong soil nonlinearity for even modest input motions produces responses that are adequately approximated with 1D nonlinear analyses using the outputs of 3D analyses that omit the lowest-velocity basins. Consequently, it appears feasible to remove very-low-velocity basins from 3D calculations and restrict the 3D nonlinear calculations to portions of the model with stiffer less nonlinear soils.

The specific issues and ground motion characteristics associated with the dilatant nature of cohesionless soils and dynamic pore pressure evolution were not considered in these investigations, although there are clearly situations where these factors have a significant influence on ground motion responses (Bonilla et al., 2005). NOAH2D is also capable of calculating nonlinear effective stress responses. While it might appear that the soil nonlinearity may be so strong in the typically soft soils associated with a characteristic waveform composed of intermittent high-frequency peaks riding on a low-frequency carrier that larger scale basin effects are dominated by local soil nonlinear responses, explicit investigation of this situation is warranted to resolve this issue.

Non-uniform implementations of linear 3D viscoelastic finite-difference methods have evolved rapidly (Pitarka, 1999; Moczo et al., 2007; Pei et al., 2009). Adaptive mesh refinement (AMR) has recently evolved to solve difficult nonlinear problems that require widely varying grid resolution as a function of space and time. For instance, George (2006) implemented AMR to solve the nonlinear tsunami propagation and inundation problem using a finite volume implementation that allowed the combination of modeling transoceanic tsunami propagation as well as coastal inundation in single global-scale simulations that achieves remarkable computational efficiency. Similar to the tsunami problem, nonlinear basin responses are confined to a relatively small portion of the grid near the free surface, but may require grid spacing to be dynamically adjusted to increase sampling by up to an order of magnitude in the top several hundred meters of a basin. An AMR implementation of 3D nonlinear finite-difference would allow the entire calculation grid to efficiently maintain a consistent dispersion frequency limit as nonlinear evolves in time and space.

References

Aoi, S., T. Kunugi, and H. Fujiwara, 2008, Trampoline Effect in Extreme Ground Motion, Science, 322, 727-730, doi:10.1126/science.1163113.

Beresnev, I. A., K. L. Wen, and Y. T. Yeh, 1995, Nonlinear soil amplification: its corroboration in Taiwan, *Bull. Seism. Soc. Am.*, **85**, 496 –515.

Beresnev, I. A., E. H. Field, K. V. Abeele, and P. A. Johnson, 1998, Magnitude of nonlinear sediment response in the Los Angeles basin during the 1994 Northridge, California, earthquake, *Bull. Seism. Soc. Am.*, **88**, 1079 –1084.

Beresnev, I.A., A.M. Nightengale, and W.J. Silva, 2002, Properties of vertical ground motions, *Bull. Seism. Soc. Am.*, **92**, 3152–3164.

Bonilla, L. F., 2000, Computation of linear and nonlinear response for near field ground motion, Ph.D. Dissertation, University of California, Santa Barbara.

Bonilla, L.F., R.J. Archuleta, and D. Lavallée, 2005, Hysteretic and dilatant behavior of cohesionless soils and their effects on nonlinear site response: Field data observations and modeling, *Bull. Seism. Soc. Am.*, **95**, 2373–2395.

Bonilla, L. F., P-C Liu, S. Nielsen, 2006, 1D and 2D linear and nonlinear site response in the Grenoble area, Third International Symposium on the Effects of Surface Geology on Seismic Motion, Grenoble, France, 30 August-1 September, 2006.

Cultrera, G., D. M. Boore, W. B. Joyner, and C. M. Dietel, 1999, Nonlinear soil response in the vicinity of the Van Norman complex following the 1994 Northridge, California, earthquake, *Bull. Seism. Soc. Am.*, **89**, 1214–1231.

Field, E. H., P. A. Johnson, I. A. Beresnev, and Y. Zeng, 1997, Nonlinear ground-motion amplification by sediments during the 1994 Northridge earthquake, Nature 390, 599-602

Field, E. H., Y. Zeng, P. A. Johnson, and I. A. Beresnev, 1998, Pervasive nonlinear sediment response during the 1994 Northridge earthquake: observations and finite-source simulations, J. Geophys. Res. 103, 26,869-26,883.

F-Net focal mechanisms for the 2008 earthquake http://www.fnet.bosai.go.jp/event/tdmt.php?LANG=en&ID=20080613234200&all=

George, D.L., 2006, Finite Volume Methods and Adaptive Refinement for Tsunami Propagation and Inundation, Ph.D. dissertation, Univ. Washington, Seattle, Washington.

Gibbs, J.F., Tinsley, J.C., Boore, D.M., and Joyner, W.B., 1999, Seismic velocities and geologic conditions at twelve sites subjected to strong ground motion in the 1994 Northridge, California, earthquake: a revision of OFR 96-740, U.S. Geological Survey Open-File Report 99-446, 142 pp.

Goldberg, S. A., 1960, About interaction of longitudinal and transversal elastic waves, *Acoustic Journal*, VI, 307 -310 (in Russian).

Graves, R. W., A. Pitarka, and P. G. Somerville, 1998, Ground-motion amplification in the Santa Monica Area: Effects of shallow basin-edge structure, Bull. Seism. Soc. Amer., 88, 1224-1242.

Hada, K., Y. Fujino, M. Yamada, 2009, Simulation of the strong ground-motion at IWTH25 for 2008 Iwate-Miyagi Nairiku Earthquake using distinct element method, Japan Geoscience Union (JPGU) Meeting, May 16-21, Chiba City, Japan, Abstract S152-011.

Hallier, S., E. Chaljub, M. Bouchon, and H. Sekiguchi, 2008, Revisiting the Basin-edge effect at Kobe during the 1995 Hyogo-Ken Nanbu Earthquake, Pure and Applied Geophysics, 165, 1751-1760.

Hardin, B.O., and V.P. Drnevich (1972). Shear modulus and damping in soil: design equations and curves, J. Soil Mech. Foundations Div. ASCE, 98, 667-692.

Hartzell, S., 1998, Variability in Nonlinear Sediment Response during the 1994 Northridge, California, Earthquake, Bull. Seism. Soc. Amer., 88, 1426-1437.

Hartzell, S., L. F. Bonilla, and R. A. Williams, 2004, Prediction of nonlinear soil effects, Bull. Seismol. Soc. Am. 94, 1609-1629.

Hartzell, S., M. Guatteri, P. M. Mai, P. Liu, and M. Fisk, 2005, Calculation of broadband time histories of ground motion, part II: kinematic and dynamic modeling using theoretical Green's functions and comparison with the 1994 Northridge earthquake, *Bull. Seismol. Soc. Am*., **95**, 614-645.

Iai, S., Y. Matsunaga, and T. Kameoka (1990). Strain Space Plasticity Model for Cyclic Mobility, Report of the Port and Harbour Research Institute, 29, 27-56.

Kawase, H., 1996, The cause of damage belt in Kobe: "The basin-edge effect", constructive interference of the direct S-waves with the basin induced diffracted/Rayleigh waves, Seism. Res. Lett. 67, 25-34.

Larsen, S., and J. Grieger, 1998, Elastic modeling initiative, part III: 3-D computational modeling, Expanded Abstracts, 68th Annual SEG meeting, 1803-1806.

Liu, P. C., and R. J. Archuleta, 2006, Efficient modeling of Q for 3D numerical simulation of wave propagation, *Bull. Seismol. Soc. Am.*, **96**, 1352-1358

Lomnitz, C., J. Flores, O. Novaro, T. H. Seligman, and R. Esquivel, 1999, Seismic coupling of interface modes in sedimentary bains: A recipe for distaster, Bull. Seism. Soc. Am. 89, 14-21.

Loukachev, I. , N. Pralle, and G. Gudehus, 2002, Dilatancy-Induced P Waves as Evidence for Nonlinear Soil Behavior, , Bull. Seism. Soc. Amer., 92, pp. 854–862.

Ma, S., and P. Liu, 2006, Modeling of the perfectly matched layer absorbing boundaries and intrinsic attenuation in explicit finite-element methods, *Bull. Seismol. Soc. Am.* **96**, 1779-1794, doi 10.1785/0120050219.

Masing, G., (1926). Eigenspannungen und Verfertigung beim Messing, Proceedings, 2nd International Congress on Applied Mechanics, Zurich, Switzerlandm 332-335.

Miyazaki, S., Y. Yokota, K. M. Larson, R. Kobayashi, K. Koketsu, K. Hikima, and A. Yamagiwa, 2008, Application of high-rate GPS to infer source processes of medium to large-scale earthquake rupture and early afterslip in Japan,

Moczo, P., J. Kristek, M. Galis, P. Pazak, and M. Balazovjech, 2007, The finite difference and finite-element modeling of seismic wave propagation and earthquake motion, *Acta Phys. Slovaca* 57, 177-406.

O'Connell, D.R.H., C. Wood, D. Ostenaa, L. Block, and R. LaForge, 2003, Ground Motion Evaluation for Jackson Lake Dam, Minidoka Project, Wyoming: Report 2003-2, prepared by Seismotectonics and Geophysics Group, Bureau of Reclamation, Denver, Colorado, 468 p.

O'Connell, D.R.H., 2007, Concrete dams as seismic imaging sources, Geophysical Research Letters, 34, L20307, doi:10.1029/2007GL031219.

O'Connell, D.R.H., 2008, Assessing ground shaking, Science, Vol. 322, pp. 686 – 687, DOI: 10.1126/science.1166149.

O'Connell, D.R.H., and J.P. Ake, 2010, Earthquake Ground Motion Estimation in "Earthquakes", C. Rodrigue, and E. Rovai, eds., Routledge, New York. 760 pages.

Olsen, K. B., J. C. Pechmann, and G. T. Schuster, 1995, Simulation of 3-D elastic wave propagation in the Salt Lake Basin, *Bull. Seismol. Soc. Am.*, **85**, 1688-1710.

Pei Z.-L., L.-Y. Fu, G.-X. Yu, and L. Zhang, 2009, A Wavelet-Optimized Adaptive Grid Method for Finite-Difference Simulation of Wave Propagation, *Bull. Seism. Soc. Am.*, 99, 302-313; DOI: 10.1785/0120080002.

Pitarka, A., K. Irikura, T. Iwata, and H. Sekiguchi, 1998, Three-dimensional simulation of the near-fault ground motion for the 1995 Hyogo-ken Nanbu (Kobe), Japan, earthquake, *Bull. Seism. Soc. Am.*, 88, 428-440.

Pitarka, A. (1999). 3D elastic finite-difference modeling of seismic motion using staggered grids with nonuniform spacing, *Bull. Seismol. Soc. Am.* 89, 54-68.

Robertsson, J. 0. A., J. 0. Blanch, and W. W. Symes, 1994. Viscoelastic finite-difference modcling, Geophysics 59, 1444-1456.

Seed, H. B., and I. M. Idriss, 1970, Analyses of ground motions at Union Bay, Seattle during earthquakes and distant nuclear blasts, *Bull. Seism. Soc. Am.*, **60** ,125 –136

Silva, W., C. Costantino, and S. Li, 1998, Quantification of nonlinear soil response for the Loma Prieta, Northridge, and Imperial Valley California earthquakes, in *The Effects of Surface Geology on Seismic Motion*, Irikura, Kudo, Okada, and Sasatani, eds., Balkema, Rotterdam.

Snieder, R., M. Miyazawa, E. Slob, I. Vasconcelos, and K. Wapenaar, A comparison of strategies for seismic interferometry, *Surv Geophys*, **30**, 503–523.

Stephenson, W.J., Williams, R.A., Odum, J.K., and Worley, D.M., 2007, Miscellaneous high-resolution seismic imaging investigations in Salt Lake and Utah Valleys for earthquake hazards: U.S. Geological Survey Open-File Report 2007-1152, 29 p.

Towhata, I., and K. Ishihara (1985). Modeling Soil Behavior Under Principal Axes Rotation, Fifth International Conference on Numerical Methods in Geomechanics, Nagoya, 523-530.

Trifunac, M. D., and M. I. Todorovska, 1996, Nonlinear soil response—1994 Northridge, California, earthquake, J. Geotech. Eng. 122, 725-735.

Trifunac, M. D., and M. I. Todoravska, 1998, Nonlinear soil response as a natural passive isolation mechanism—the 1994 Northridge, California, earthquake, Soil Dyn. Earthquake Eng. 17, 41-51.

Turner, J., and D.R.H. O'Connell (2009). Interferometric multichannel analysis of surface waves (IMASW), seismic surface wave survey report for the Los Angeles Department of Water and Power, Van Norman Complex.

Tsutsumi and Yeats, 1999, Tectonic Setting of the 1971 Sylmar and 1994 Northridge Earthquakes in the San Fernando Valley, California, Bull. Seism. Soc. Amer., 89, 5, pp. 1232-1249.

Wu, C., and J. M. Harris (2004). An optimized variable-grid finite-difference method for seismic forward modeling, J. Seism. Explor. 12, 343-353.

Yamada, M., J. Mori, and T. Heaton, 2009a, The slapdown phase in high-acceleration records of large earthquakes, *Seism Res. Lett.*, **80**, 559-564.

Yamada, M., K. Takezawa, M. Nakamura, K. Hada, M. Yamada, S. Ohmi, and T. Nagao, 2009b, Subsurface condition at the station IWTH25 of KiK-net, The 121st SEGJ Conference, Nagoyoa Univ., Nagoya, Japan, November 23-25, 2009.

Project Bibliography

O'Connell, D.R.H., 2008, Assessing ground shaking, Science, Vol. 322, pp. 686 – 687, DOI: 10.1126/science.1166149.

O'Connell, D.R.H., P.C. Liu, and L.F. Bonilla, in press, 2D P-SV nonlinear investigations of basin-edge amplification, Seism. Res. Lett.

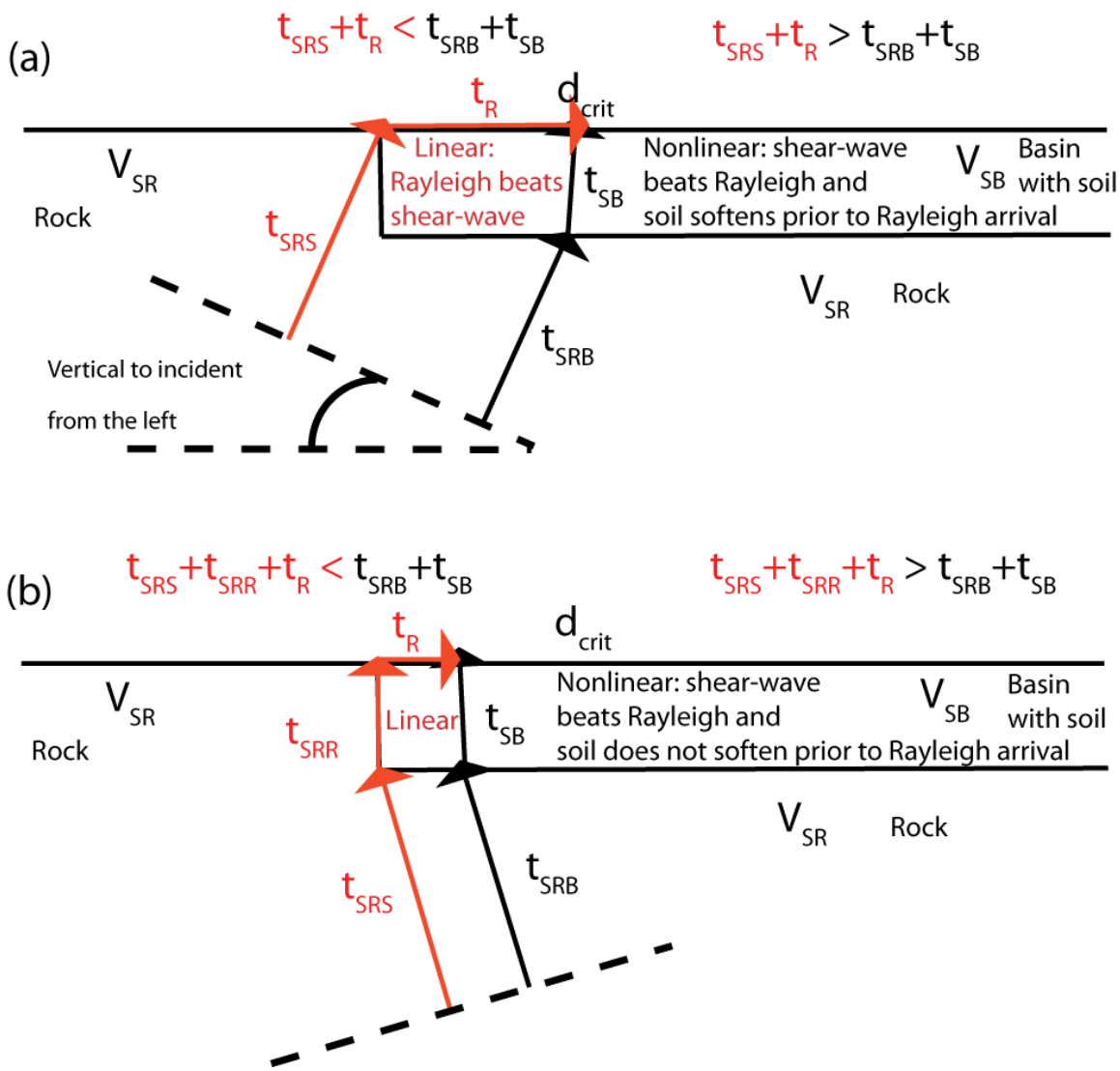

Figure 1. Schematic basin and incident wavefield geometries and first-order basin-edge amplification factors. The distance from the basin edge to the position in the basin where the travel time of the direct shear-wave and the basin-edge Rayleigh are equal, increases with decreasing incident angle from the left of the basin (a). When shear-wave are incident from the right (b), the direct shear wave arrives earlier than the basin-edge Rayleigh wave almost everywhere in the basin except close to the basin edge (b). Eventually as incident angles from the right decrease, the region of "linear" initial Rayleigh wave propagation is eliminated as direct shear waves precede the basin-edge Rayleigh wave and begin softening (degrading) the soil shear moduli prior to the arrival of the basin-edge Rayleigh wave.

Figure 2. Overview of the portion of the hangingwall region of the **M** 6.9 2008 Iwate-Miyagi earthquake containing station IWTH25, which is located adjacent to a high-gradient stream on a low terrace. IWTH25 is located about 3 km from the epicenter and on the hangingwall about 7 km from the near-surface fault tip.

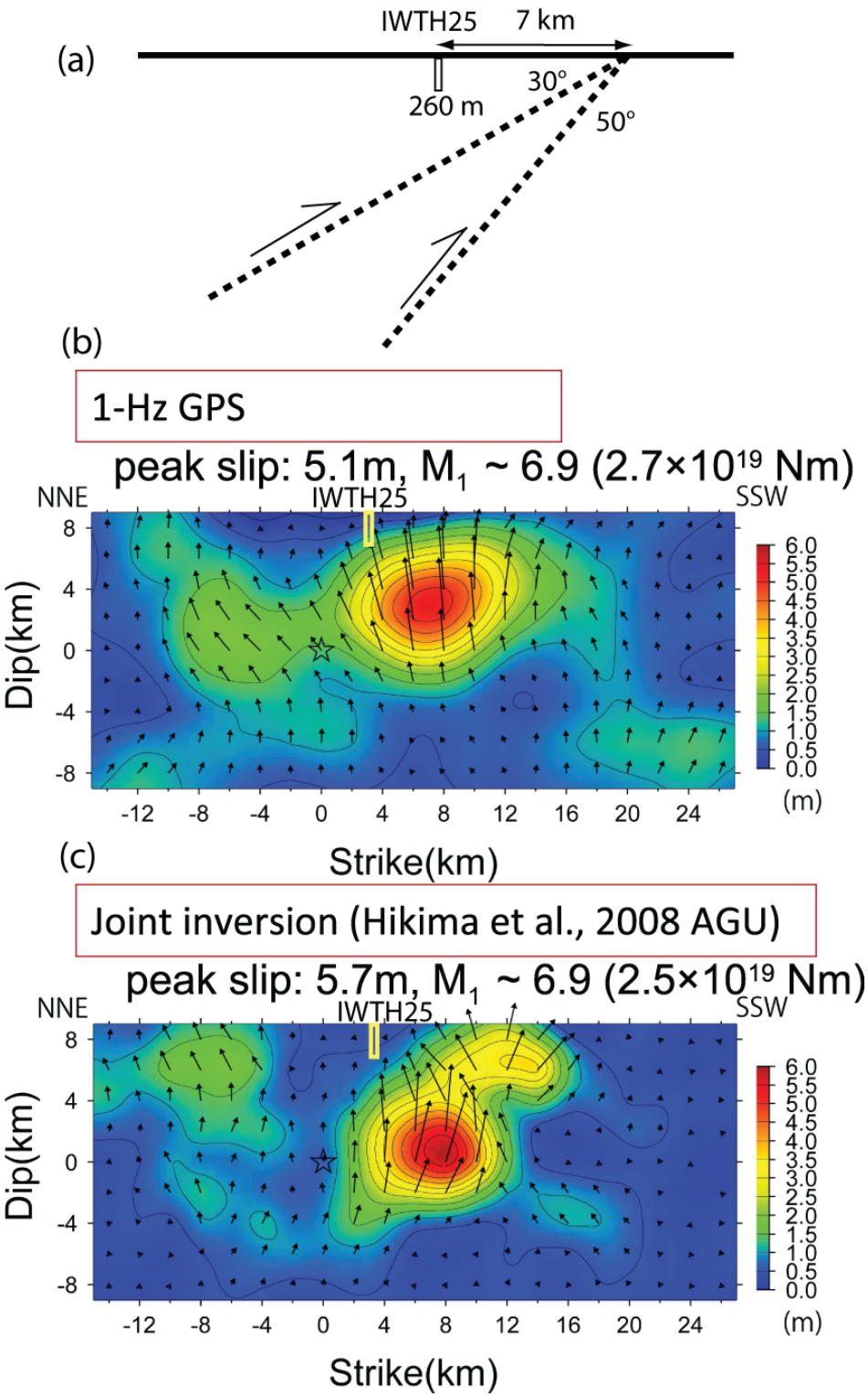

Figure 3. Position of station IWTH25 relative to the the **M** 6.9 2008 Iwate-Miyagi earthquake rupture plane (a) and comparison of GPS (b) with joint inversion from Miyazaki et al. (2009) (c). IWTH25 is located near a strike position of 3 km in (b) and (c).

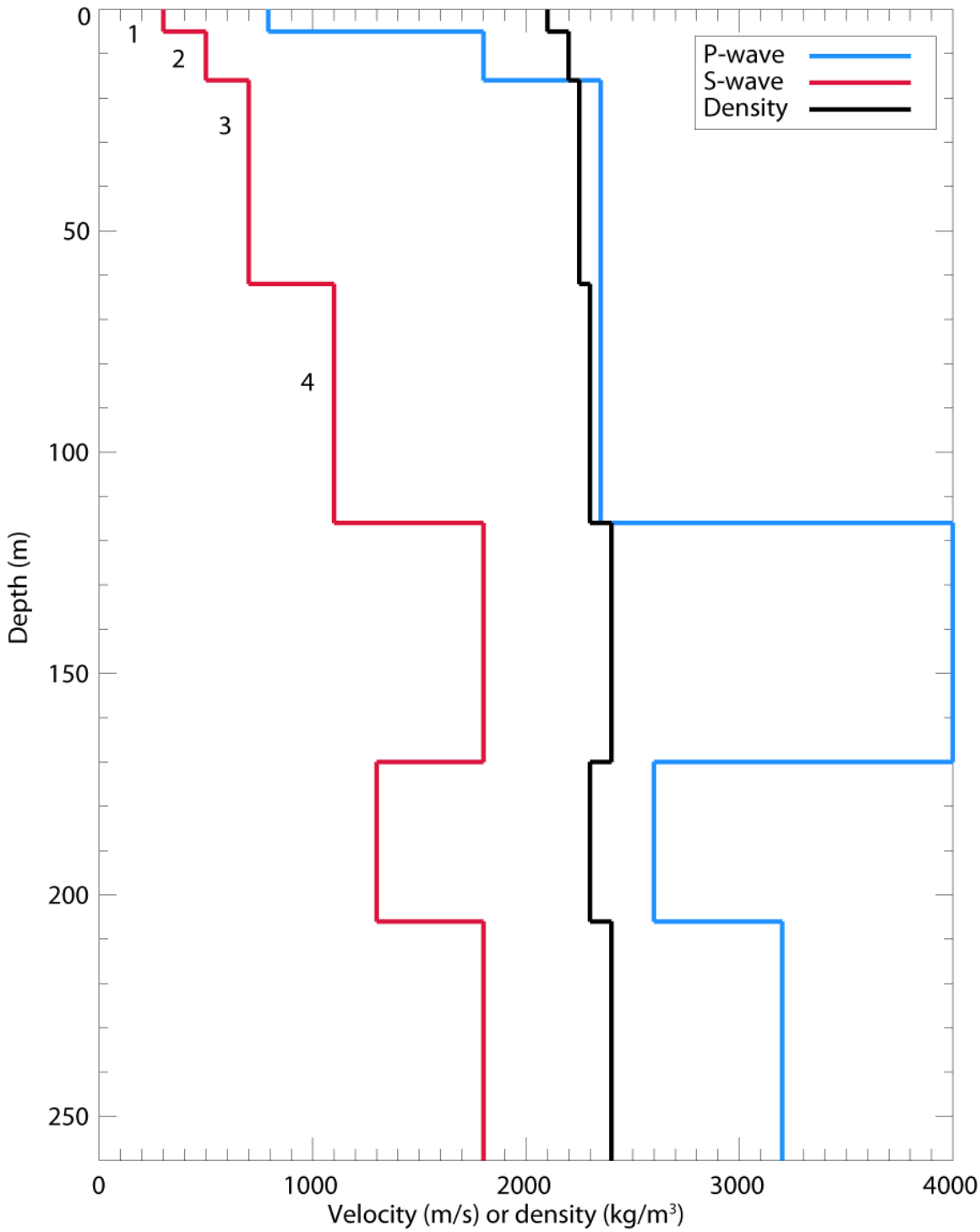

Figure 4. Station IWTH25 1D velocity model modified from Aoi et al. (2008) with a thin low-velocity surface layer added to better fit the observed surface responses. Corresponding nonlinear soil curves are shown in Figure 5 for the number layers.

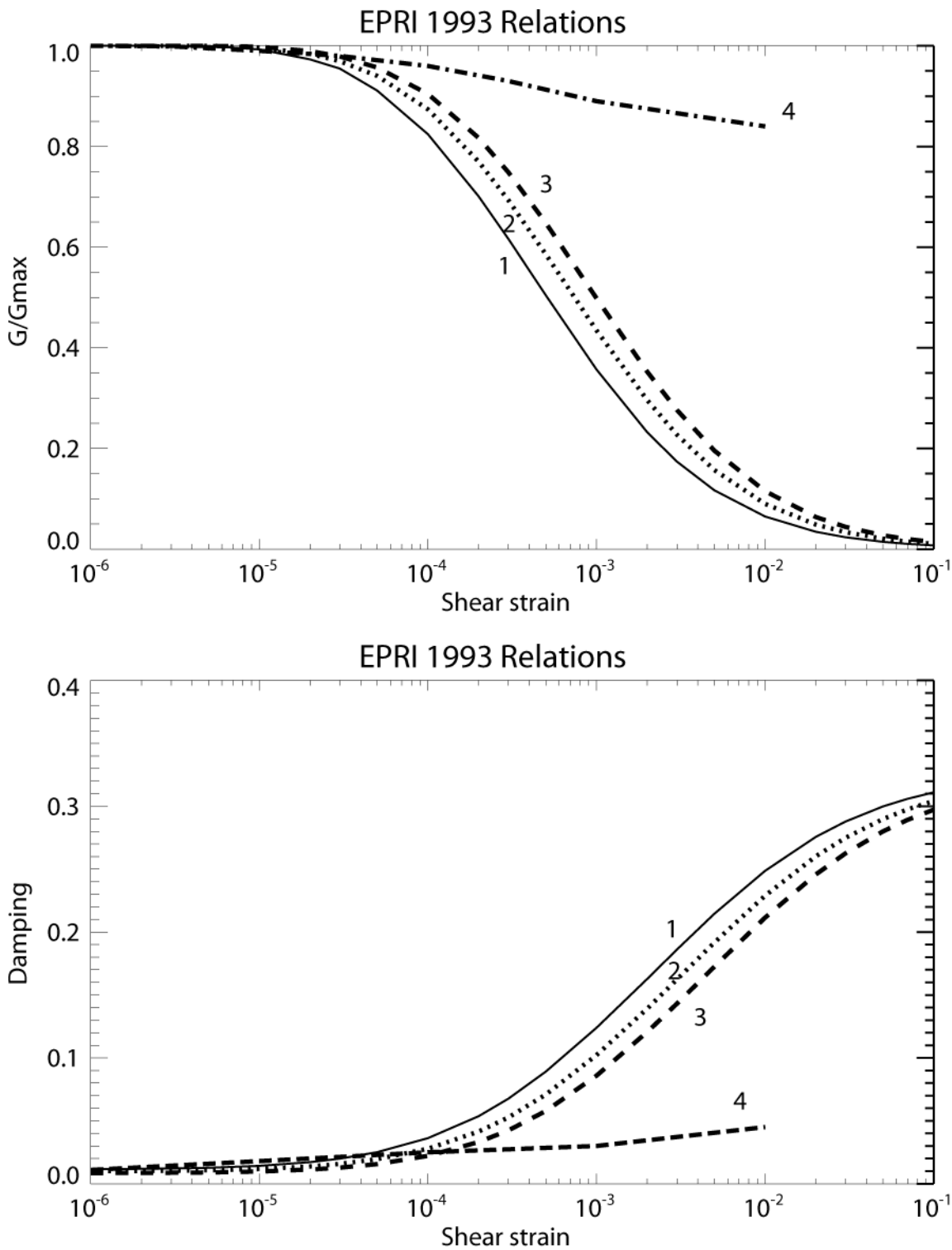

Figure 5. EPRI (1993) soil curves labeled to correspond to their corresponding velocity layers in the velocity model in Figure 3.

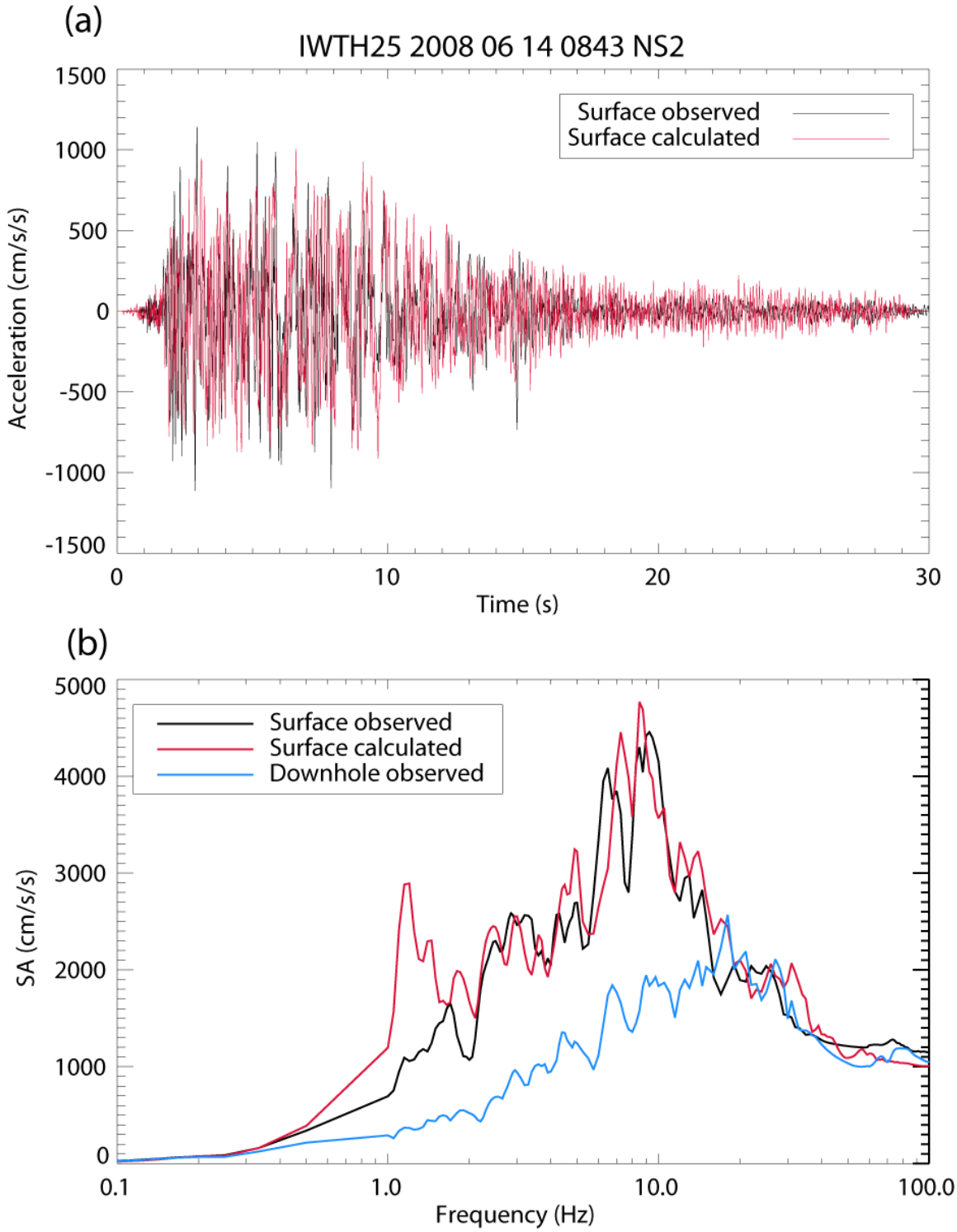

Figure 6. IWTH25 north-component observed (black) and NOAHW synthetic (red) surface acceleration (a) and corresponding acceleration response spectra for 5% damping (b).

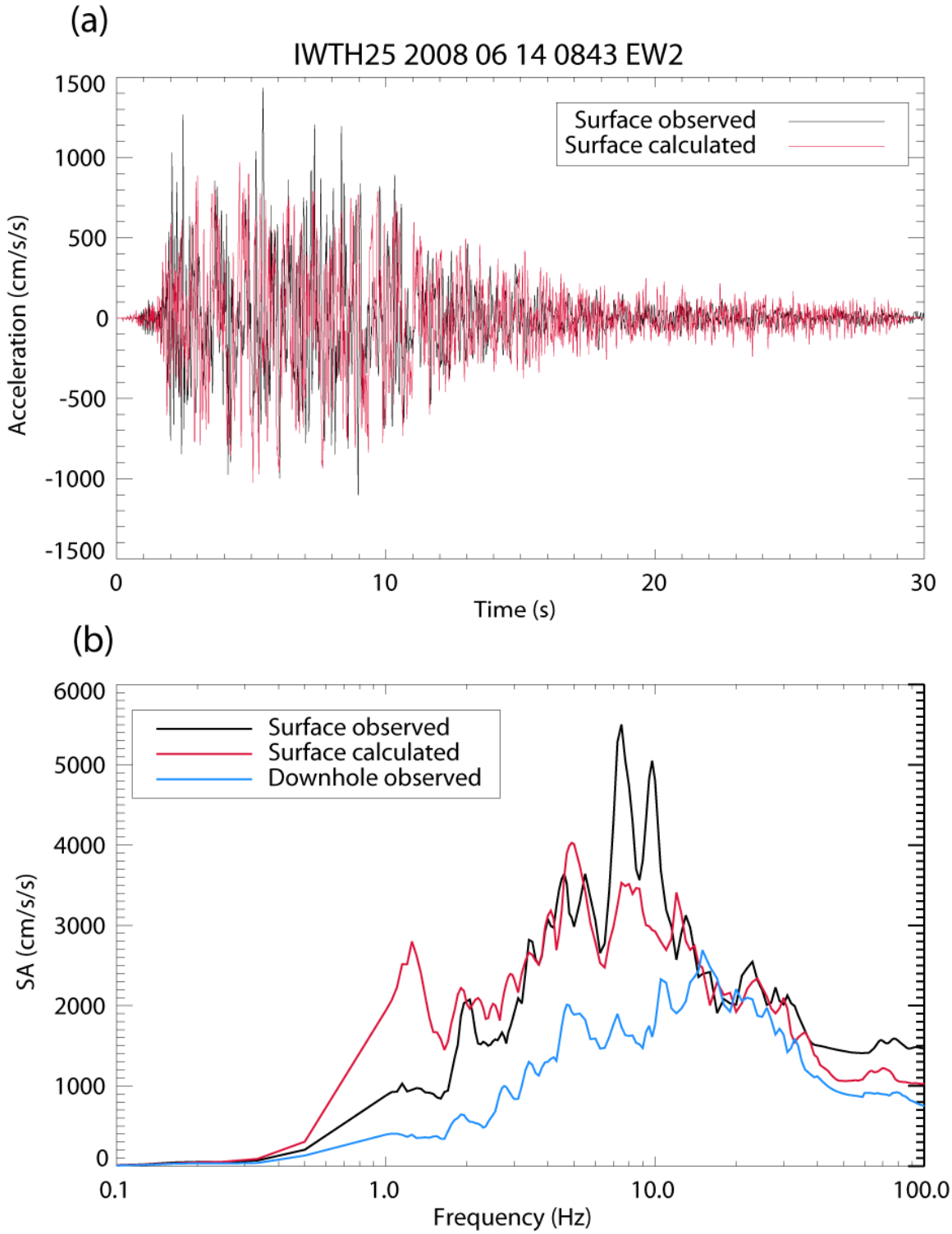

Figure 7. IWTH25 east-component observed (black) and NOAHW synthetic (red) surface acceleration (a) and corresponding acceleration response spectra for 5% damping (b).

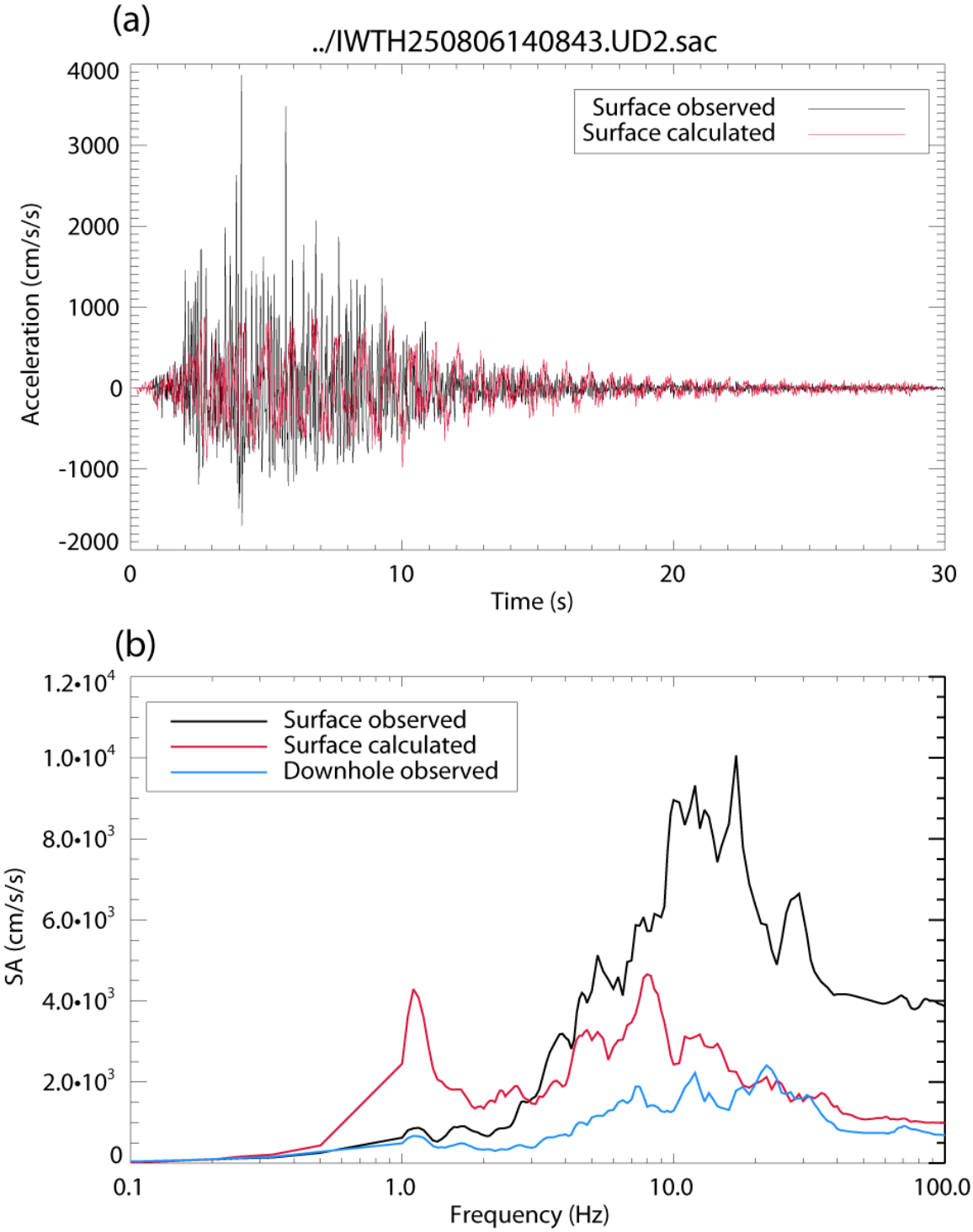

Figure 8. IWTH25 vertical-component observed (black) and NOAHW SH approximation synthetic (red) surface acceleration (a) and corresponding acceleration response spectra for 5% damping (b).

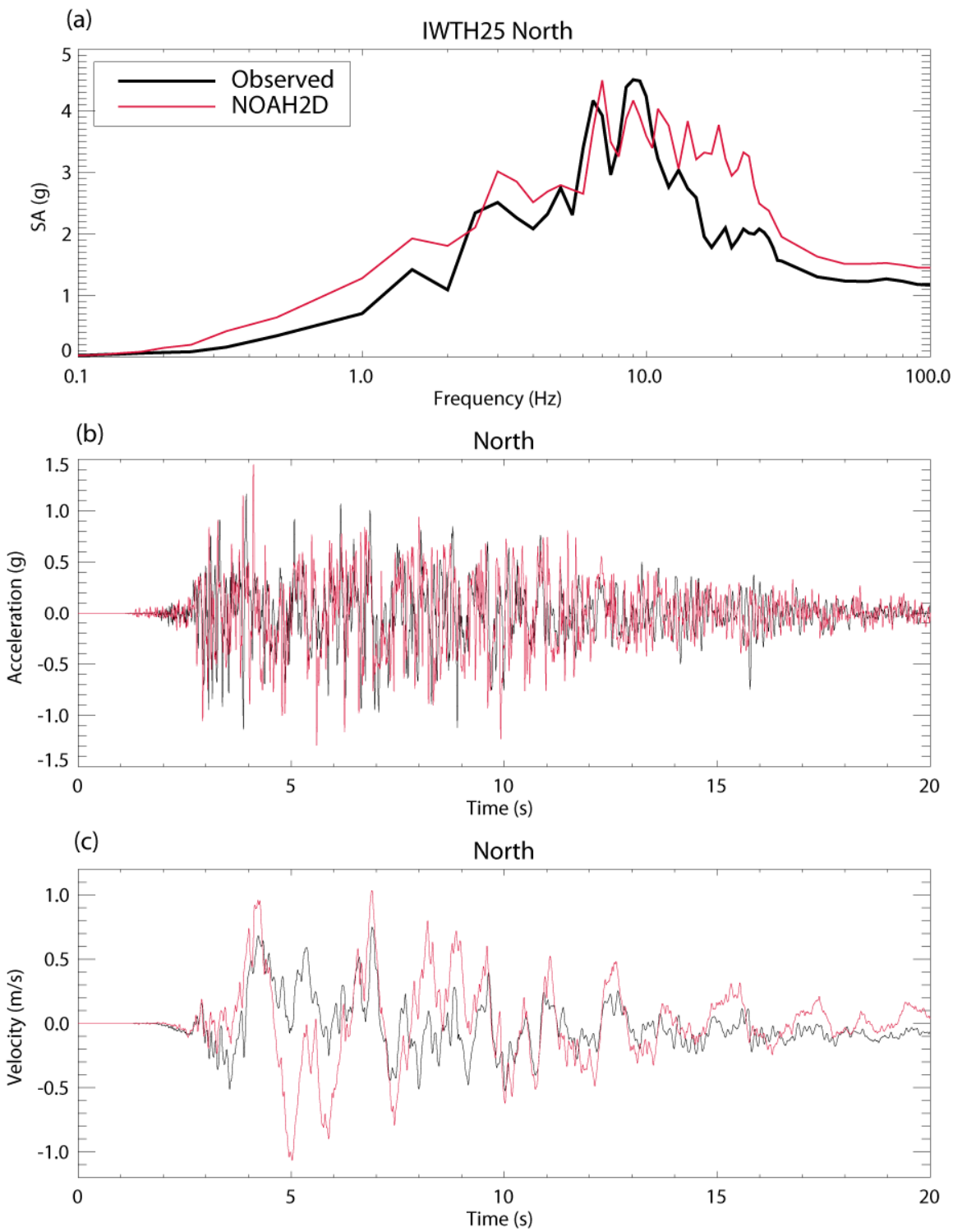

Figure 9. IWTH25 north-component observed (black) and NOAH2D P-SV synthetic (red) 5%-damping response spectra (a), surface acceleration (b), and surface velocity (c) for a site located 4m from the lateral velocity change in the low-velocity region with the plane wave incident at 80-degrees from the opposite (far end) of the low-velocity region.

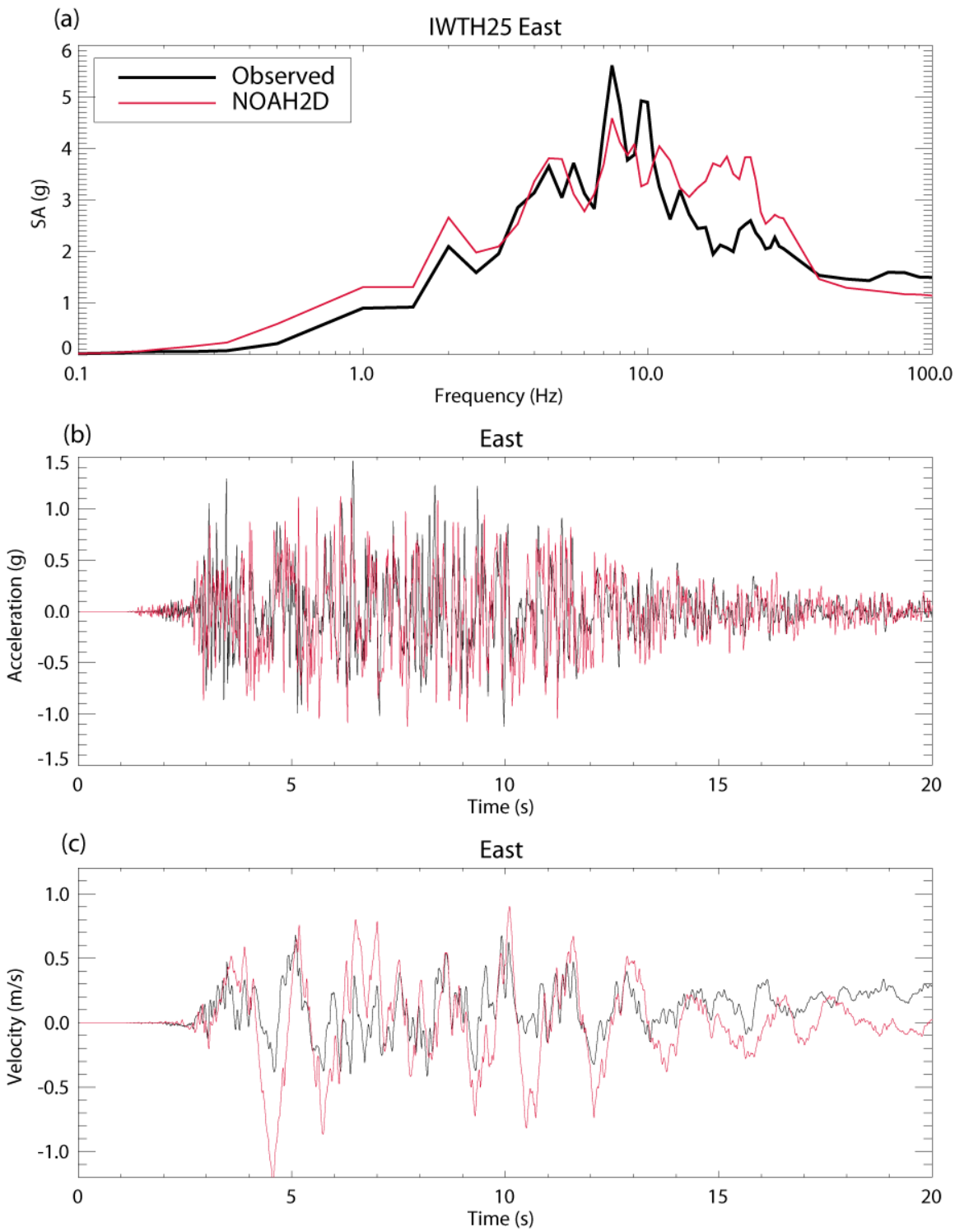

Figure 10. IWTH25 east-component observed (black) and NOAH2D P-SV synthetic (red) 5%-damping response spectra (a), surface acceleration (b), and surface velocity (c) for a site located 4m from the lateral velocity change in the low-velocity region with the plane wave incident at 80-degrees from the opposite (far end) of the low-velocity region.

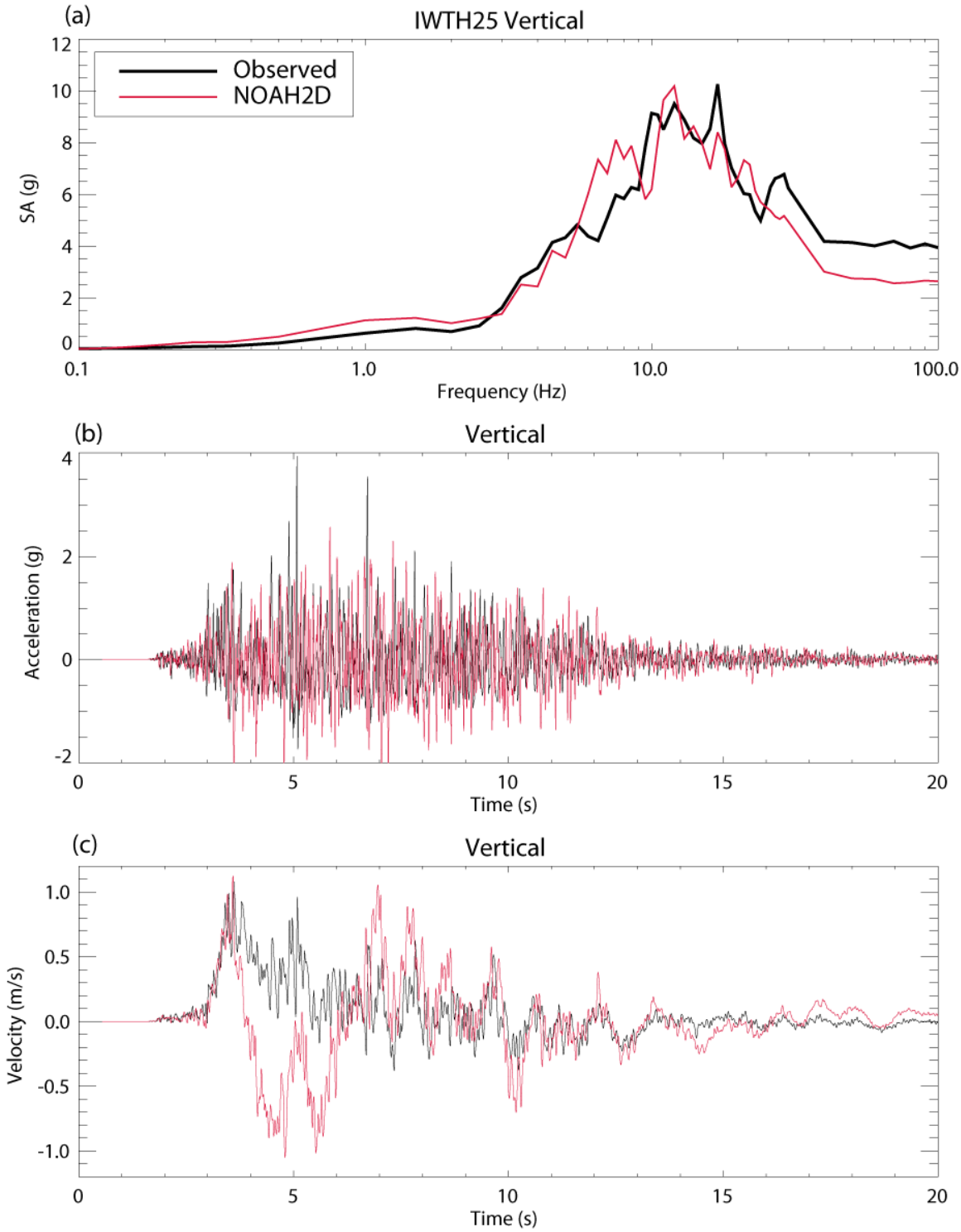

Figure 11. IWTH25 vertical-component observed (black) and NOAH2D P-SV north-vertical synthetic (red) 5%-damping response spectra (a), surface acceleration (b), and surface velocity (c) for the same site geometry as Figure 8.

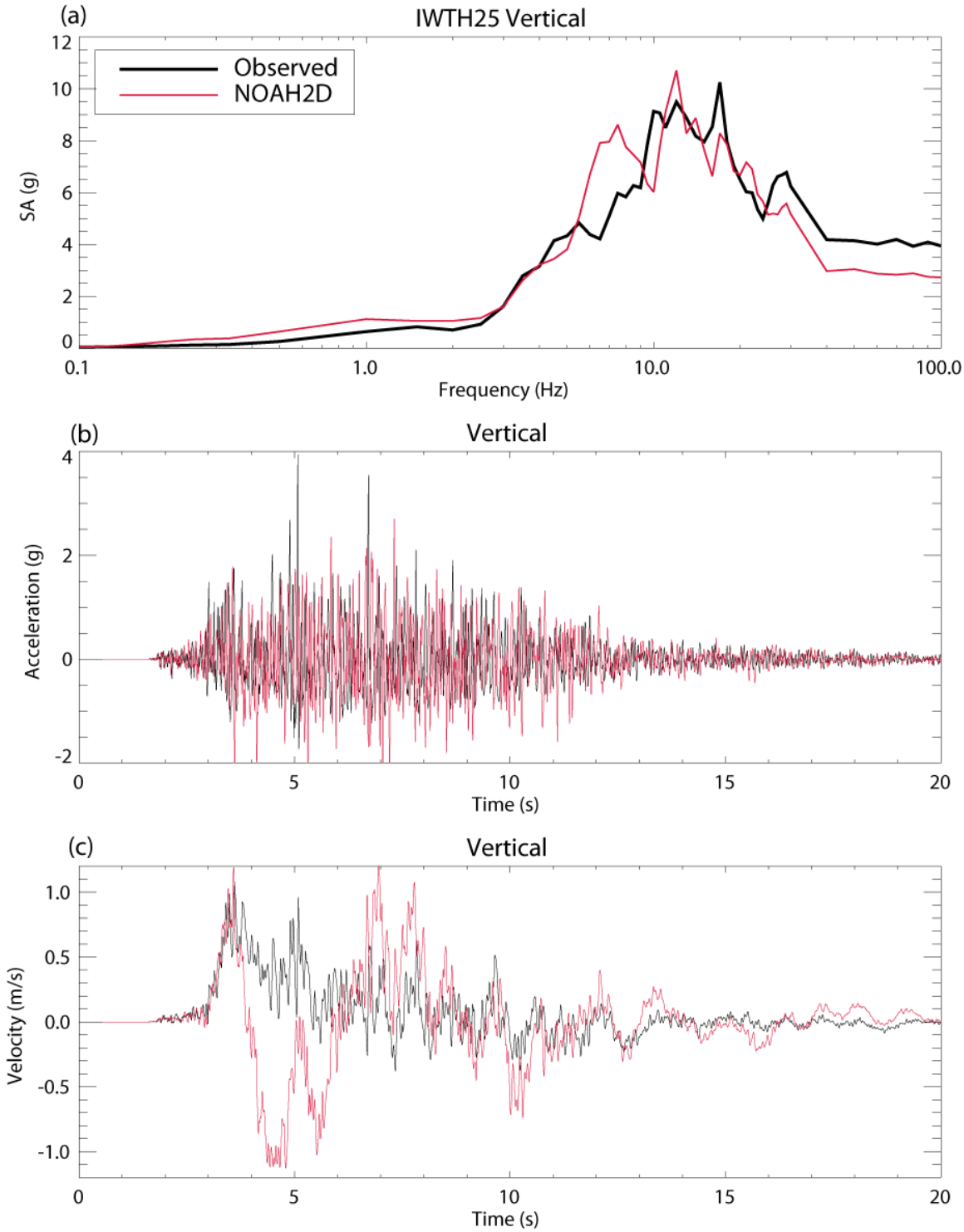

Figure 12. IWTH25 vertical-component observed (black) and NOAH2D P-SV east-vertical synthetic (red) 5%-damping response spectra (a), surface acceleration (b), and surface velocity (c) for the same site geometry as Figure 8.

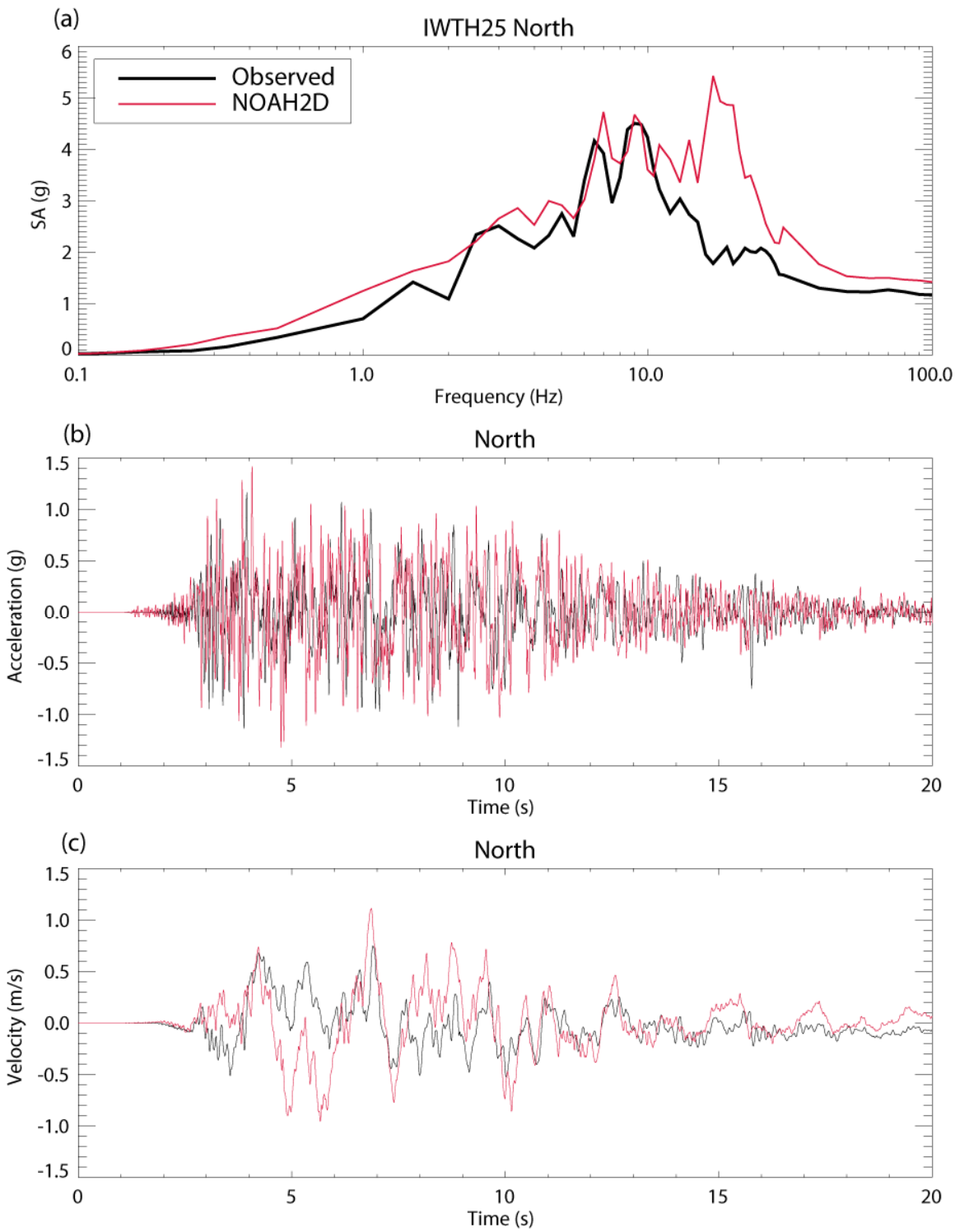

Figure 13. IWTH25 north-component observed (black) and NOAH2D P-SV synthetic (red) 5%-damping response spectra (a), surface acceleration (b), and surface velocity (c) for a site located 4m from the lateral velocity change in the low-velocity zone with the plane wave incident at 80-degrees from the near end of the low-velocity region.

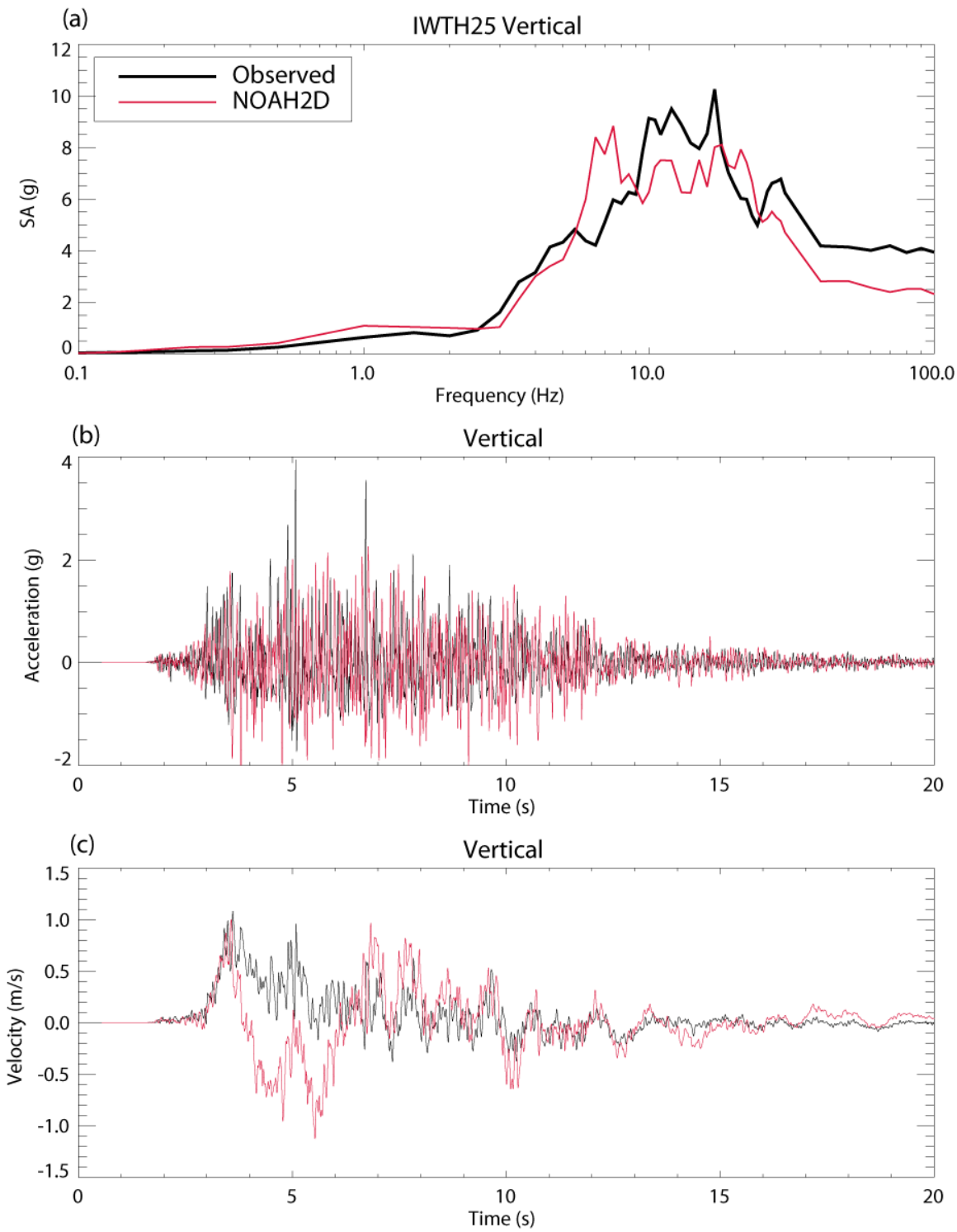

Figure 14. IWTH25 vertical-component observed (black) and NOAH2D P-SV north-vertical synthetic (red) 5%-damping response spectra (a), surface acceleration (b), and surface velocity (c) for the same site geometry as Figure 12.

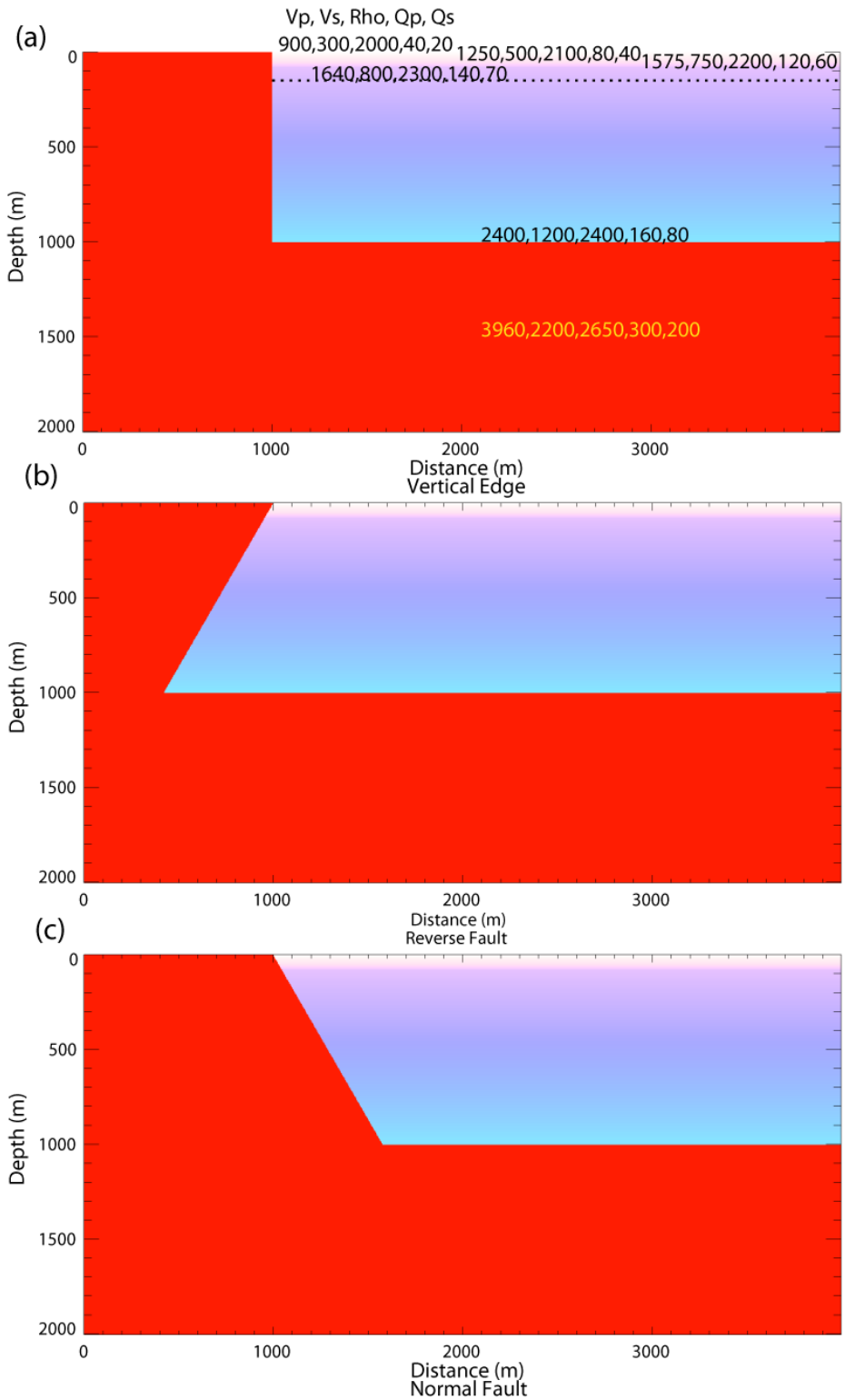

Figure 15. Three 2D velocity models, the vertical basin-edge interface (a), the reverse-faulting basin-edge interface with 60-degree dip (b), and the normal-faulting basin-edge interface with 60-degree dip (c). Nonlinear soil responses are computed from the surface to 148 m depth in the basin (as indicated by the dotted line in a). The tie points between gradients in the basin are shown at their depths with labeled values in (a).

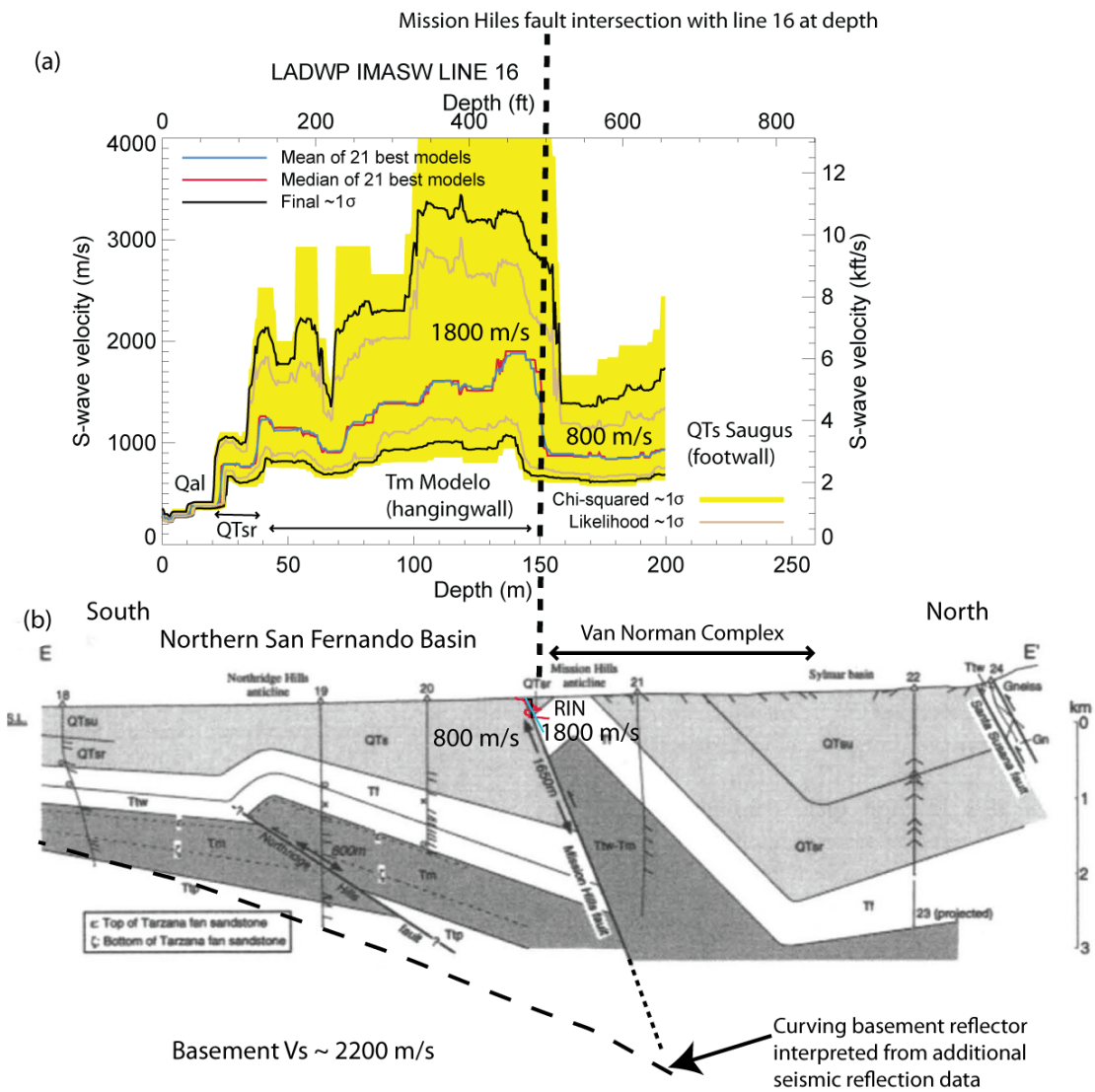

Figure 16. A surface wave shear-wave velocity profile (a) from the hanging wall of the Mission Hills fault (Turner and O'Connell, 2009), shown in cross section E-E' from Tsutsumi and Yeats (1999) (b) provides a first-order indication of the shallow shear-wave velocity contrast across the northern end of the San Fernando basin. Shear-wave velocity structure across the Mission Hill fault bounding the northern end of the San Fernando basin is primarily controlled by the velocity contrast between the ~1800 m/s Modelo (Monterrey) Formation (Tm) in the hanging wall and the ~800 m/s Saugus Formation (QTs) in the footwall (a). Thin (0-20m) Quaternary alluvium (Qal) with shear-wave velocities of ~ 300 m/s are intermittently present throughout the Van Norman Complex based on 16 surface wave surveys in the Van Norman Complex (Turner and O'Connell, 2009) and 5 borehole measurements (Gibbs et al, 1999) that included strong motion site RIN. The approximate position of RIN is shown in (b). Basement shear-wave velocity is assumed to be similar to the shear-wave velocities of basement rock at the ROSRINE site downstream of Paicoma Dam (site PAC).

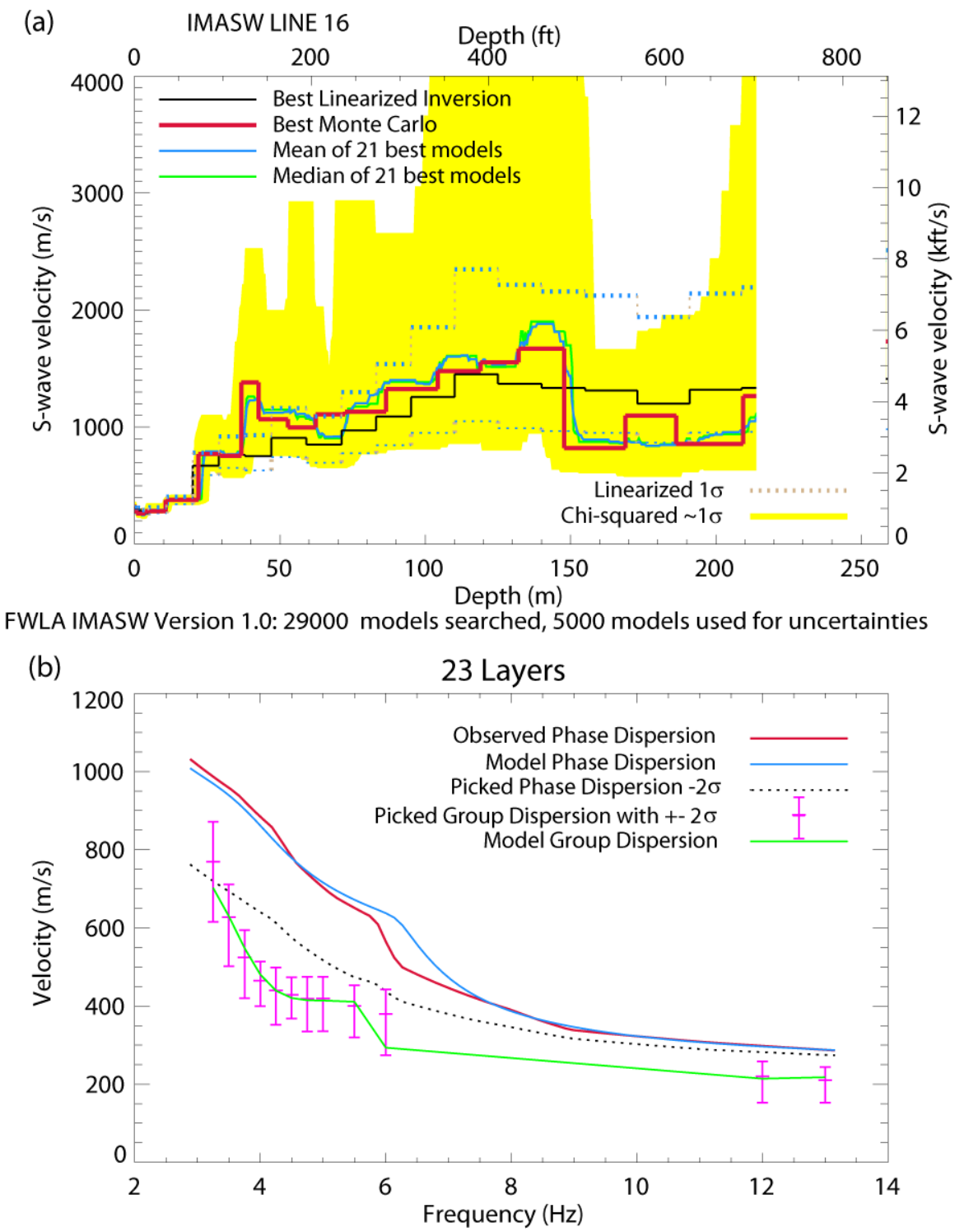

Figure 17. IMASW Line 16 survey near strong motion station RIN (Figure 16). IMASW Line 16 shear-wave velocity inversion results (a) and Rayleigh wave dispersion fits (b) indicate that the strong low-velocity zone at 150 m depth is well-resolved. In particular, well-constrained low-frequency group velocities are obtained from noise-correlation waveforms. Good low-frequency NCF signal-to-noise was produced from the traffic noise from nearby Interstate Highways 405 and 5.

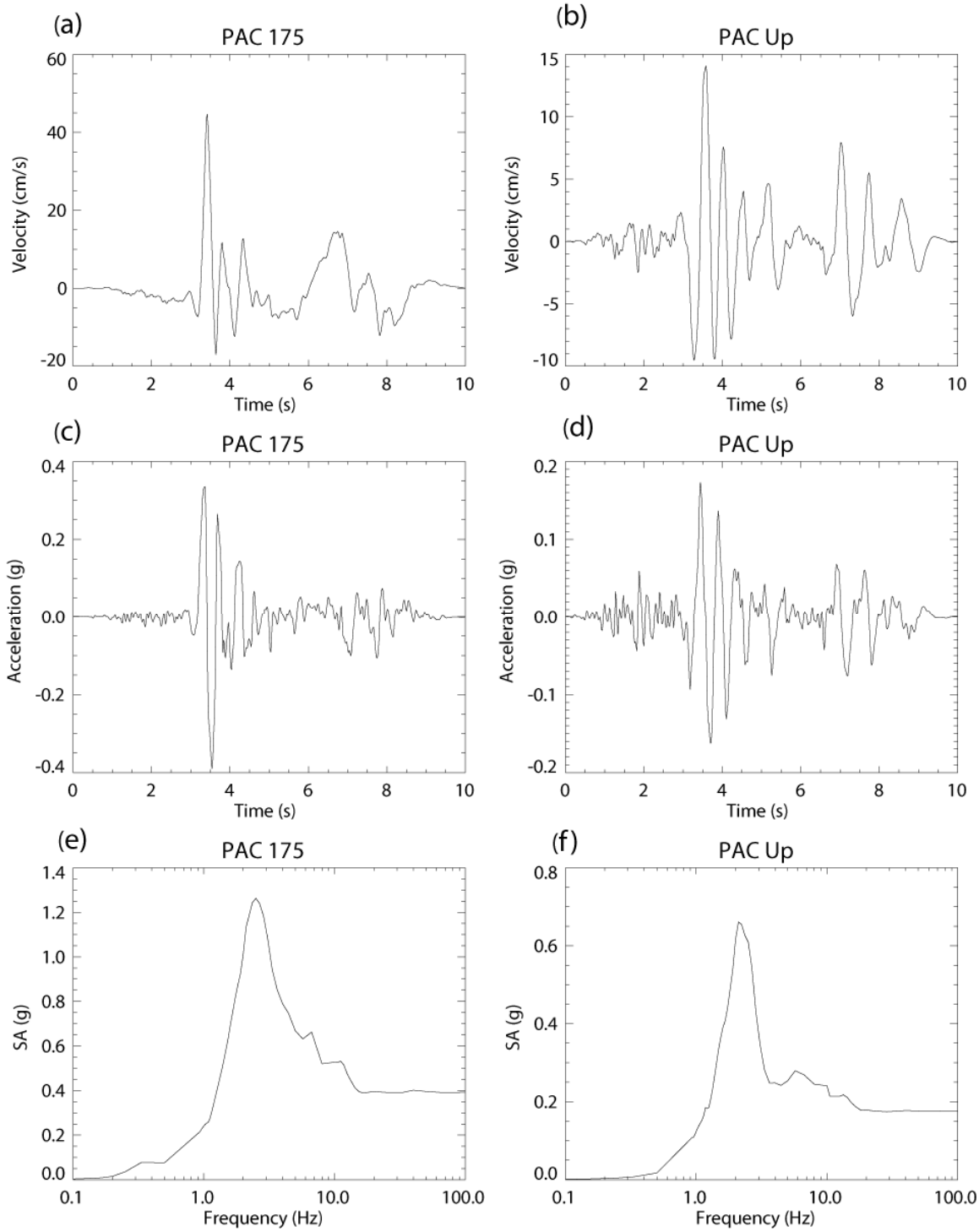

Figure 18. Pacoima Dam downstream horizontal- and vertical-component velocity (a and b) and acceleration (c and d) seismograms used as input ground motions with corresponding acceleration response spectra (5% damping) (e and f).

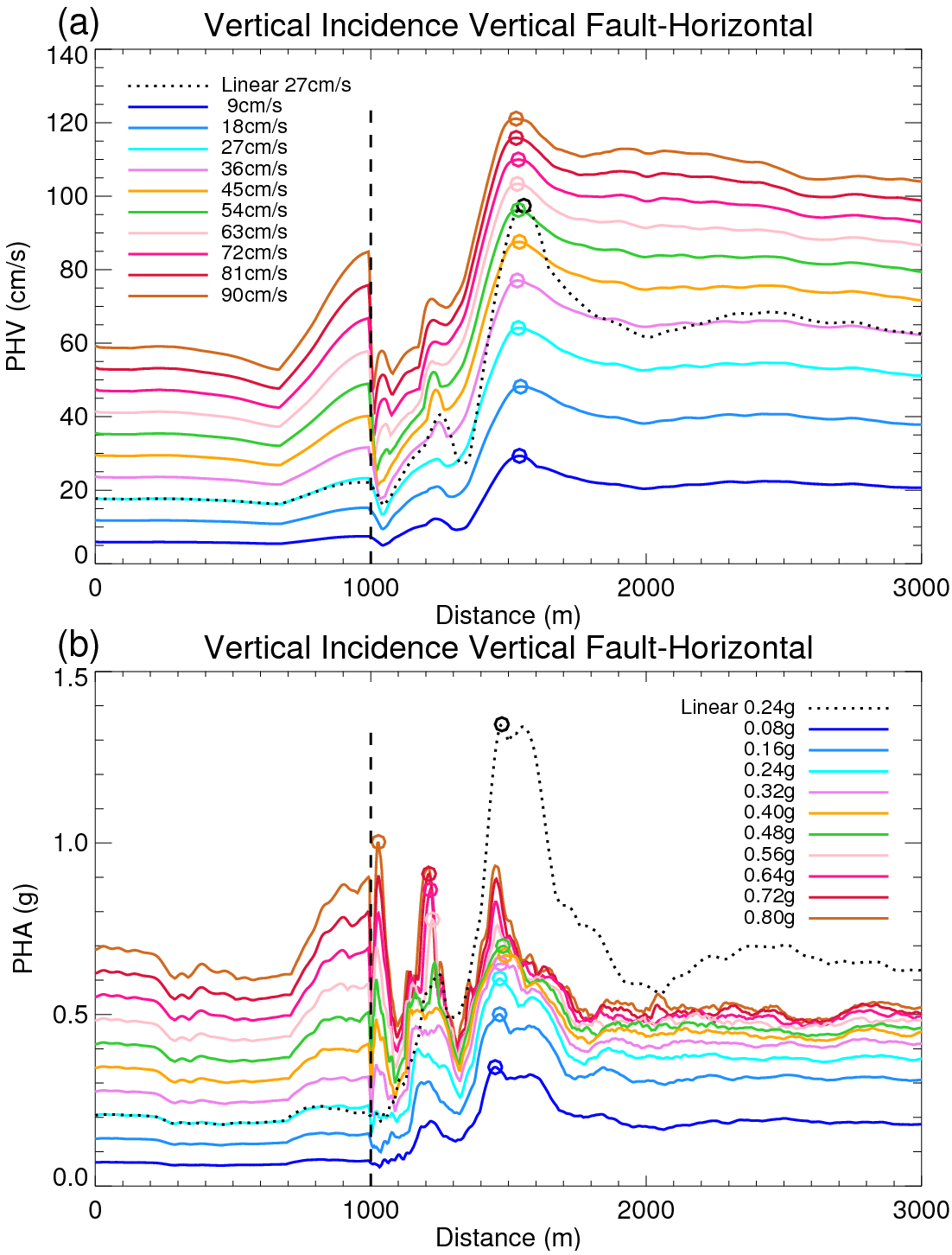

Figure 19. Vertically incident vertical-basin-edge 2D velocity model PHV (a) and PHA (b) as a function of horizontal position color-coded by corresponding uniform rock surface amplitude. The basin edge is located at 1000 m as indicated by the vertical dashed lines in (a) and (b), with the basin to the right. The maximum amplitude for each input amplitude curves within or close to the basin is indicated by circles color-coded by peak input amplitude.

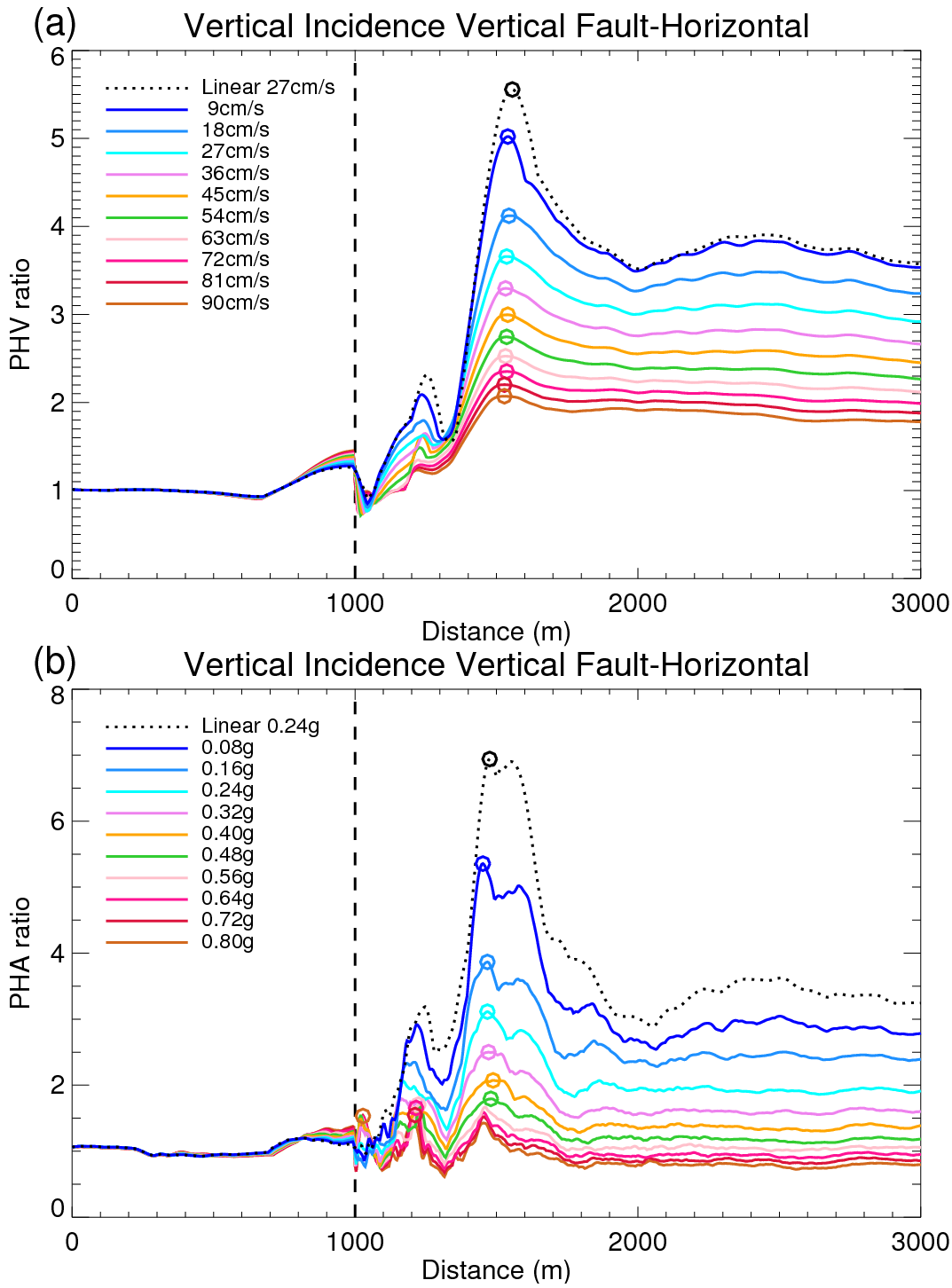

Figure 20. Vertically incident vertical-basin-edge 2D velocity model PHV ratio relative to linear rock (a) and PHA ratio relative to linear rock (b) as a function of horizontal position color-coded by corresponding uniform rock surface amplitude. The basin edge is located at 1000 m as indicated by the vertical dashed lines in (a) and (b), with the basin to the right. The maximum amplitude for each input amplitude curves within or close to the basin is indicated by circles color-coded by peak input amplitude.

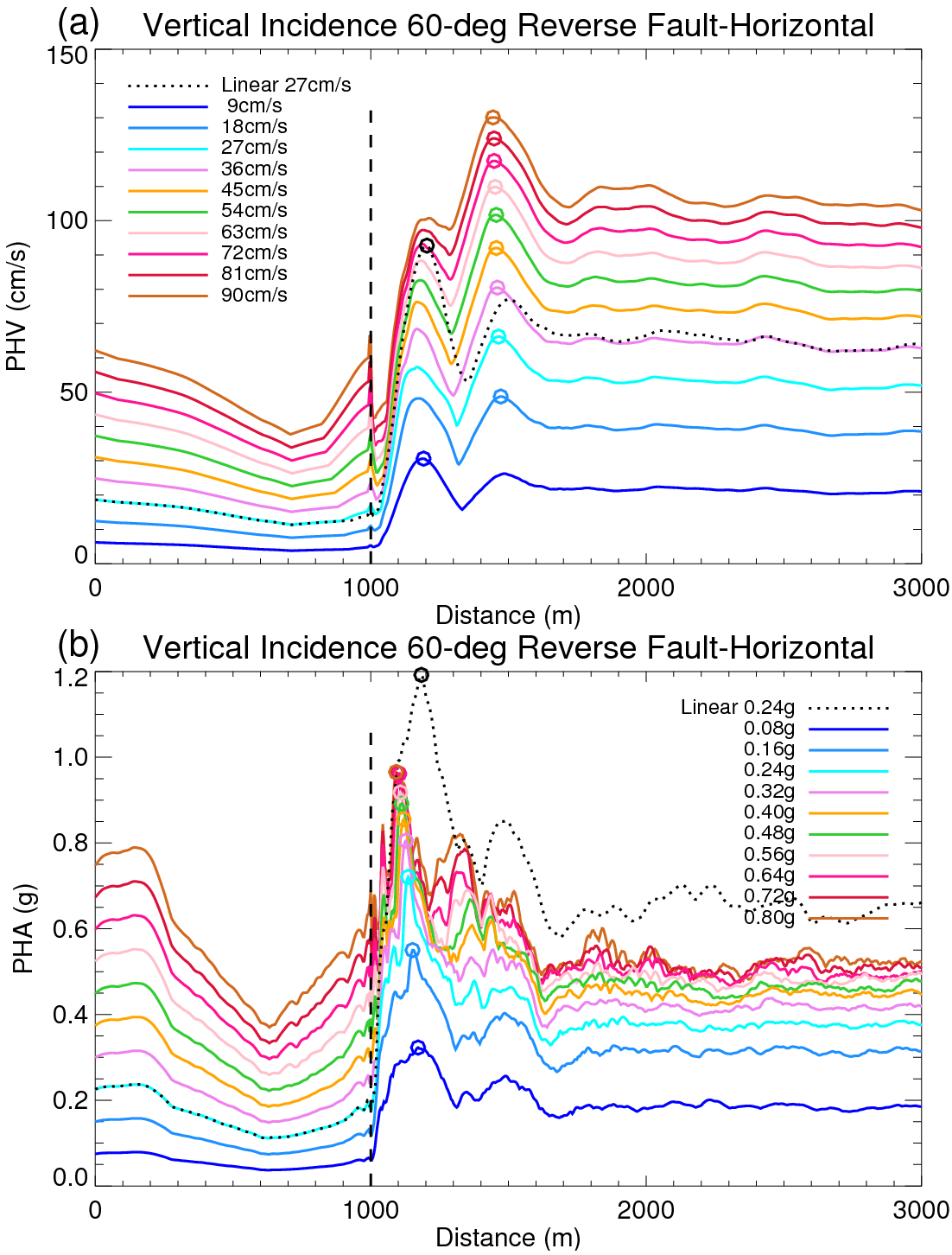

Figure 21. Vertically-incident 60-degree-dip reverse fault 2D velocity PHV (a) and PHA (b) as a function of horizontal position color-coded by corresponding uniform rock surface amplitude. The basin edge is located at 1000 m as indicated by the vertical dashed lines in (a) and (b), with the basin to the right. The maximum amplitude for each input amplitude curves within or close to the basin is indicated by circles color-coded by peak input amplitude.

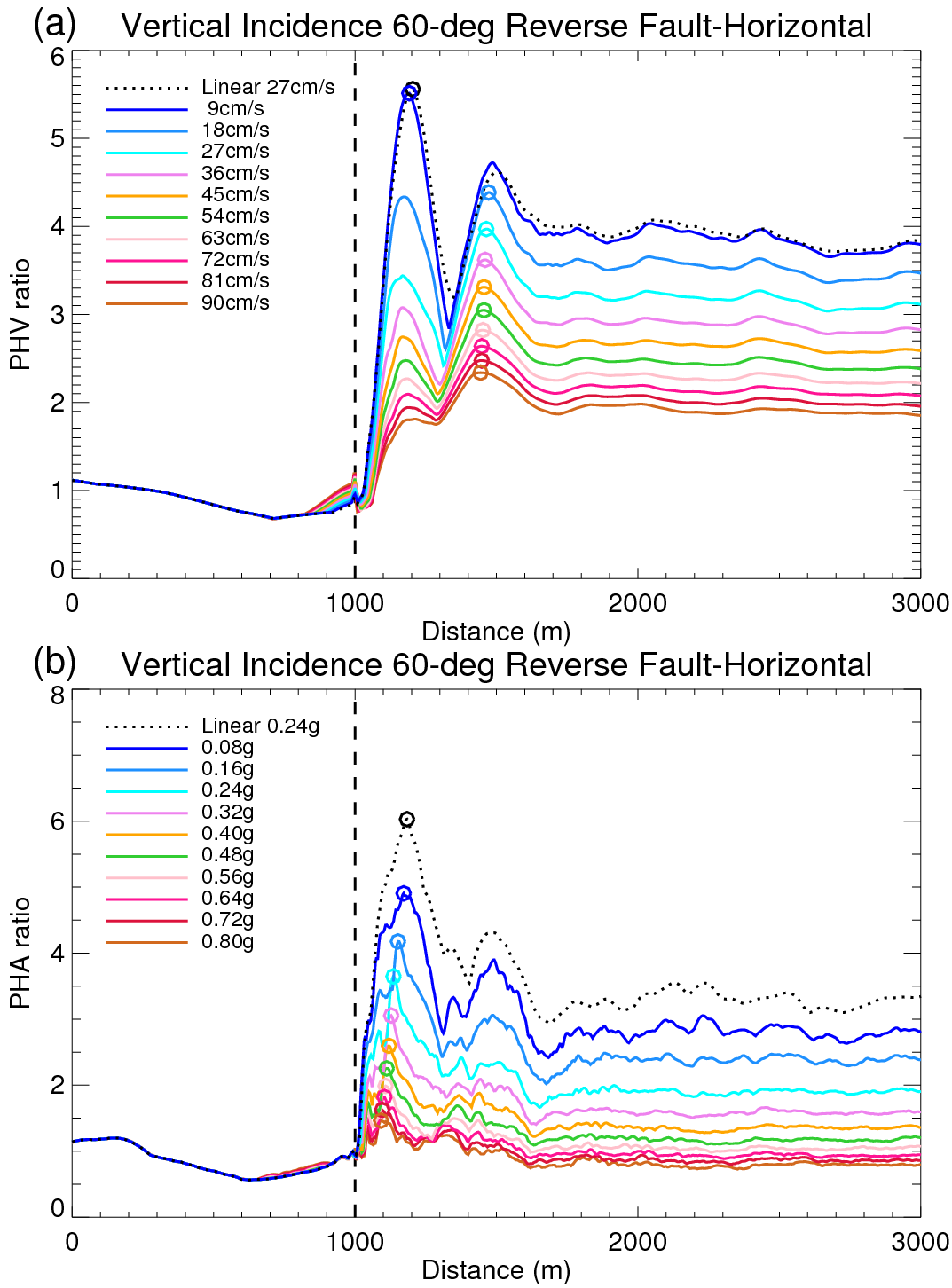

Figure 22. Vertically-incident 60-degree-dip reverse fault 2D velocity PHV ratio relative to linear rock (a) and PHA ratio relative to linear rock (b) as a function of horizontal position color-coded by corresponding uniform rock surface amplitude. The basin edge is located at 1000 m as indicated by the vertical dashed lines in (a) and (b), with the basin to the right. The maximum amplitude for each input amplitude curves within or close to the basin is indicated by circles color-coded by peak input amplitude.

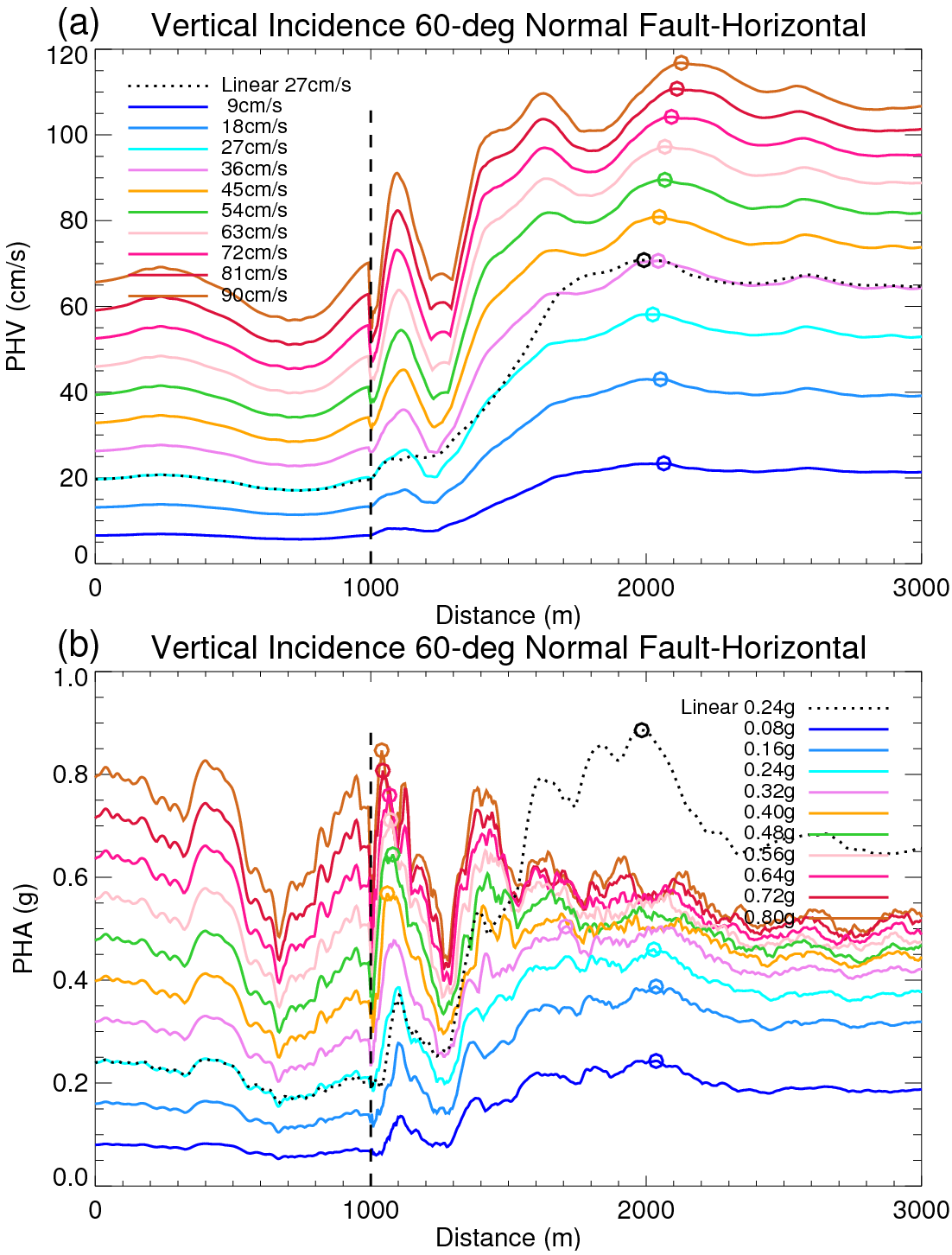

Figure 23. Vertically-incident 60-degree-dip normal fault 2D velocity model PHV (a) and PHA (b) as a function of horizontal position color-coded by corresponding uniform rock surface amplitude. The basin edge is located at 1000 m as indicated by the vertical dashed lines in (a) and (b), with the basin to the right. The maximum amplitude for each input amplitude curves within or close to the basin is indicated by circles color-coded by peak input amplitude.

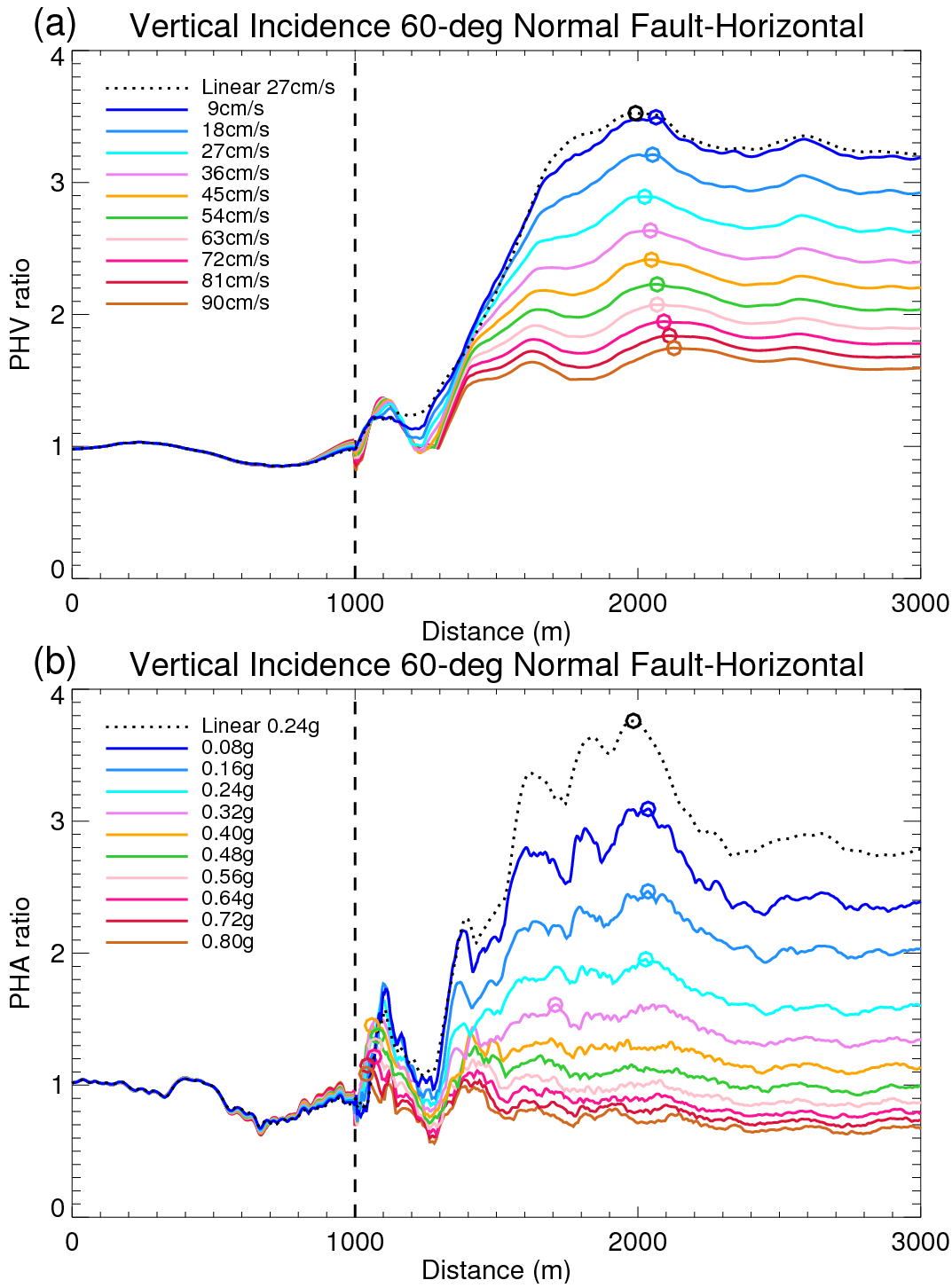

Figure 24. Vertically-incident 60-degree-dip normal fault 2D velocity model PHV ratio relative to linear rock (a) and PHA ratio relative to linear rock (b) as a function of horizontal position color-coded by corresponding uniform rock surface amplitude. The basin edge is located at 1000 m as indicated by the vertical dashed lines in (a) and (b), with the basin to the right. The maximum amplitude for each input amplitude curves within or close to the basin is indicated by circles color-coded by peak input amplitude.

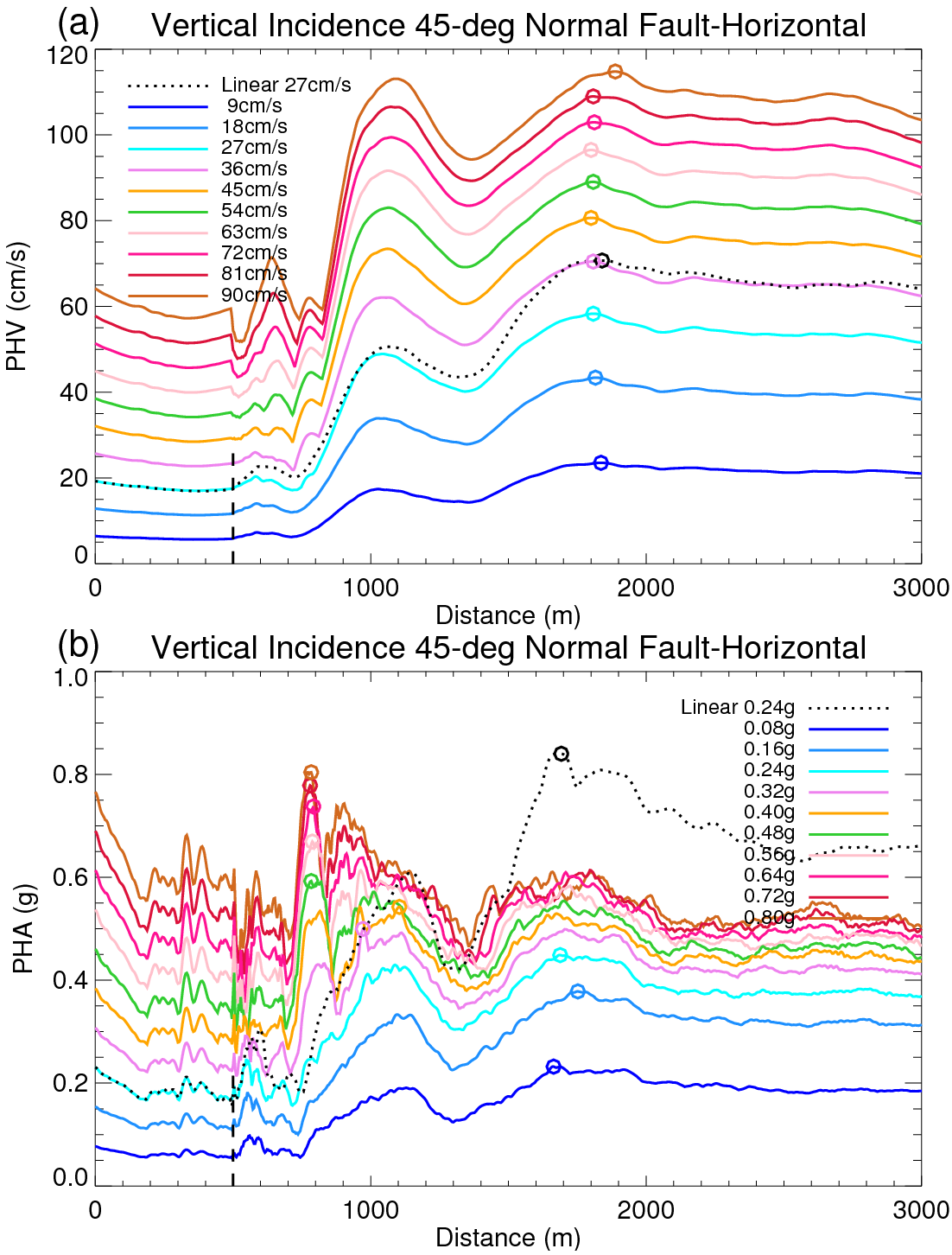

Figure 25. Vertically-incident 45-degree-dip normal fault 2D velocity model PHV (a) and PHA (b) as a function of horizontal position color-coded by corresponding uniform rock surface amplitude. The basin edge is located at 500 m as indicated by the vertical dashed lines in (a) and (b), with the basin to the right. The maximum amplitude for each input amplitude curves within the basin is indicated by circles color-coded by peak input amplitude.

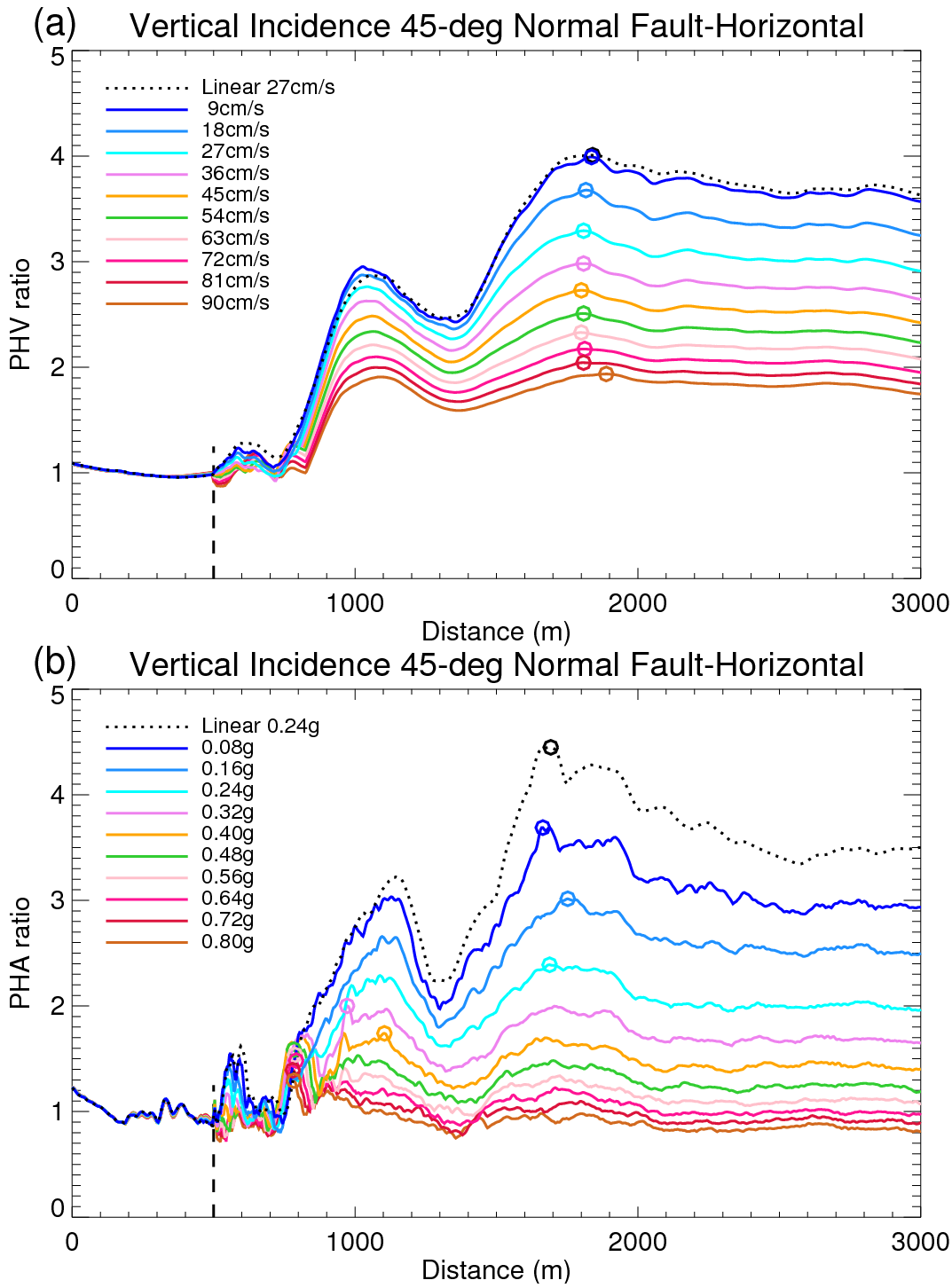

Figure 26. Vertically-incident 45-degree-dip normal fault 2D velocity model PHV ratio relative to linear rock (a) and PHA ratio relative to linear rock (b) as a function of horizontal position color-coded by corresponding uniform rock surface amplitude. The basin edge is located at 500 m as indicated by the vertical dashed lines in (a) and (b), with the basin to the right. The maximum amplitude for each input amplitude curves within the basin is indicated by circles color-coded by peak input amplitude.

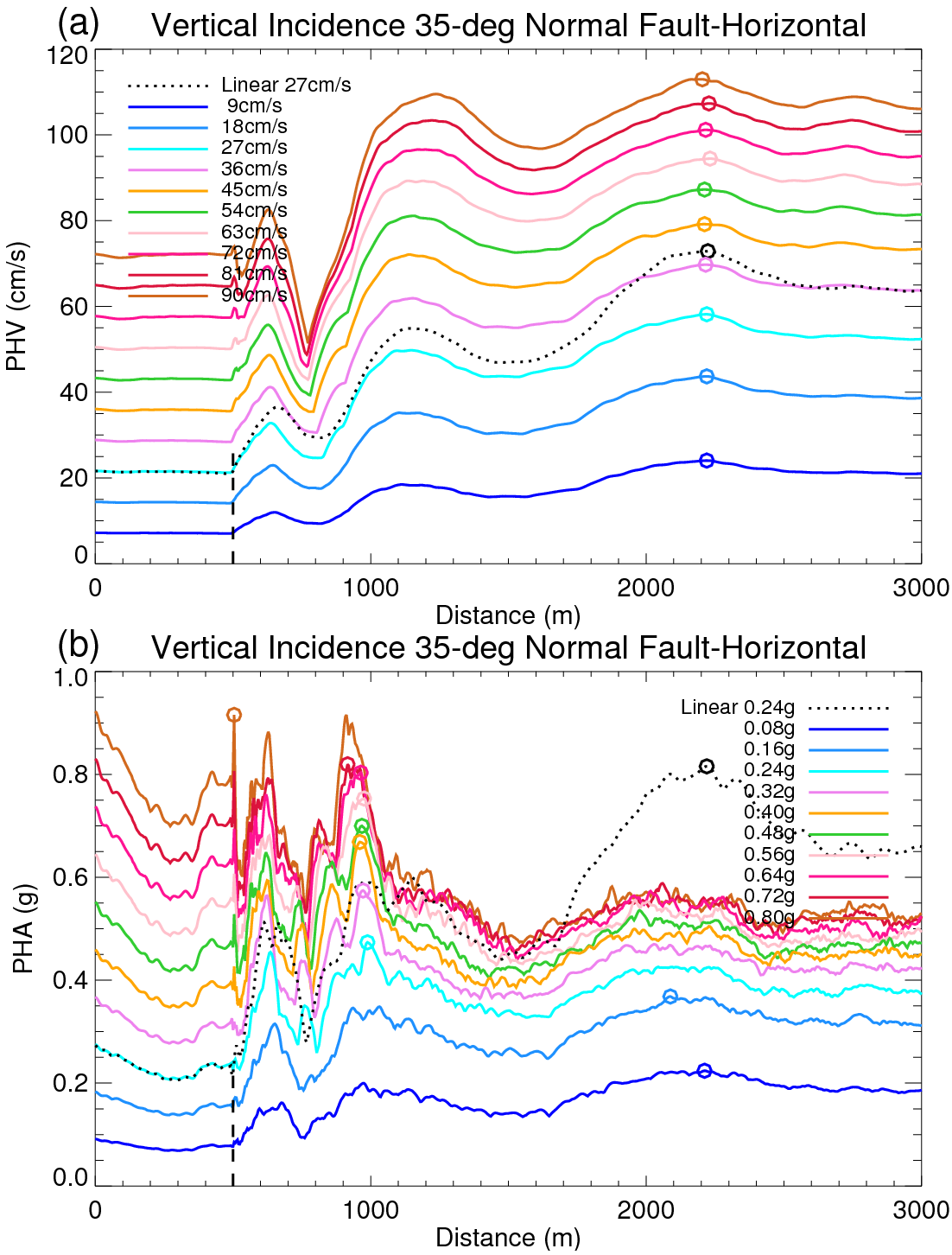

Figure 27. Vertically-incident 35-degree-dip normal fault 2D velocity model PHV (a) and PHA (b). See Figure 6 for details. The basin edge is located at 500 m as indicated by the vertical dashed lines in (a) and (b), with the basin to the right. The maximum amplitude for each input amplitude curves within the basin is indicated by circles color-coded by peak input amplitude. The maximum nonlinear PHA migrates toward the fault as input PHA increases in (b).

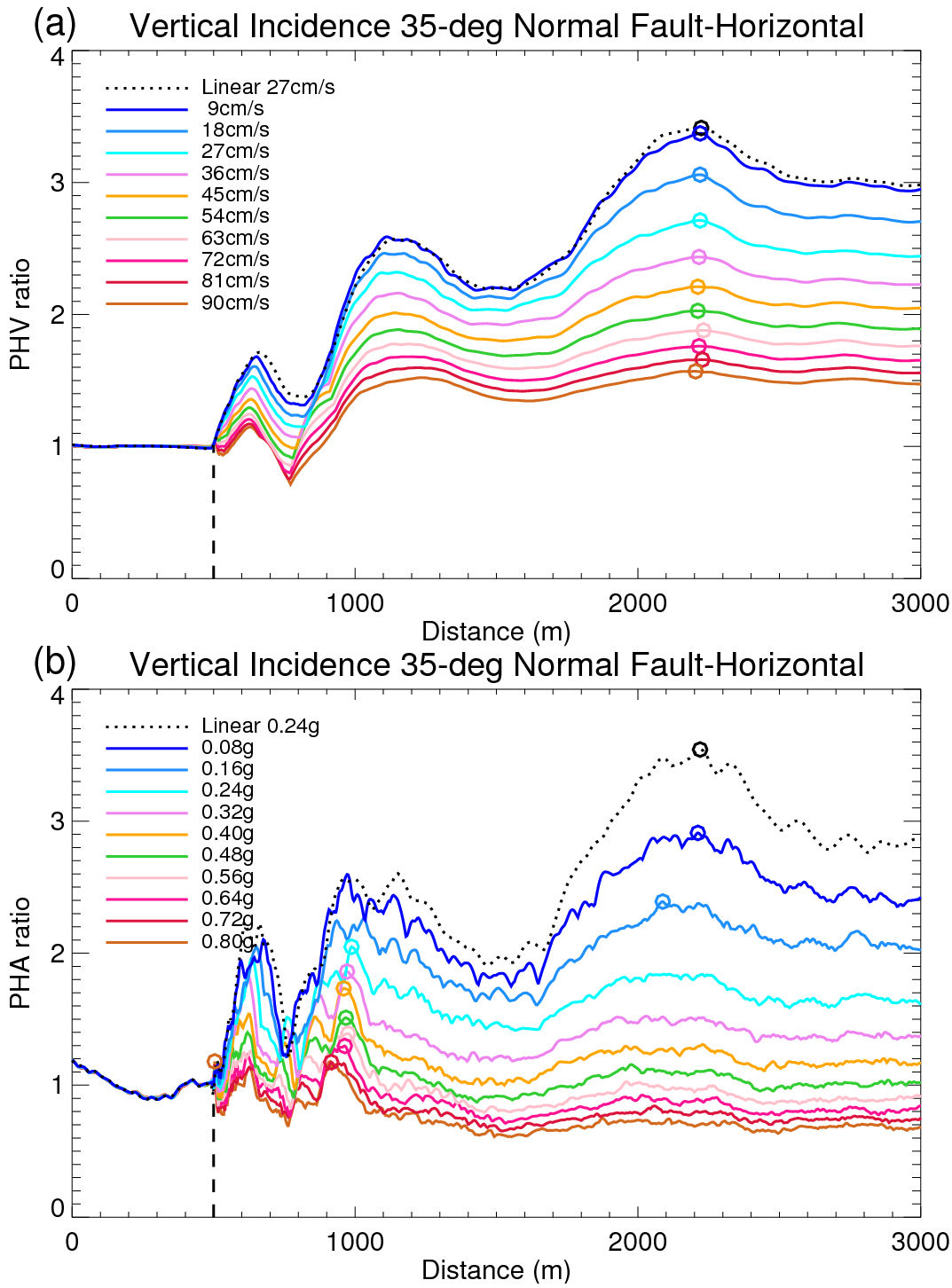

Figure 28. Vertically-incident 35-degree-dip normal fault 2D velocity model PHV ratio relative to linear rock (a) and PHA ratio relative to linear rock (b). The basin edge is located at 500 m as indicated by the vertical dashed lines in (a) and (b), with the basin to the right. The maximum amplitude for each input amplitude curves within the basin is indicated by circles color-coded by peak input amplitude.

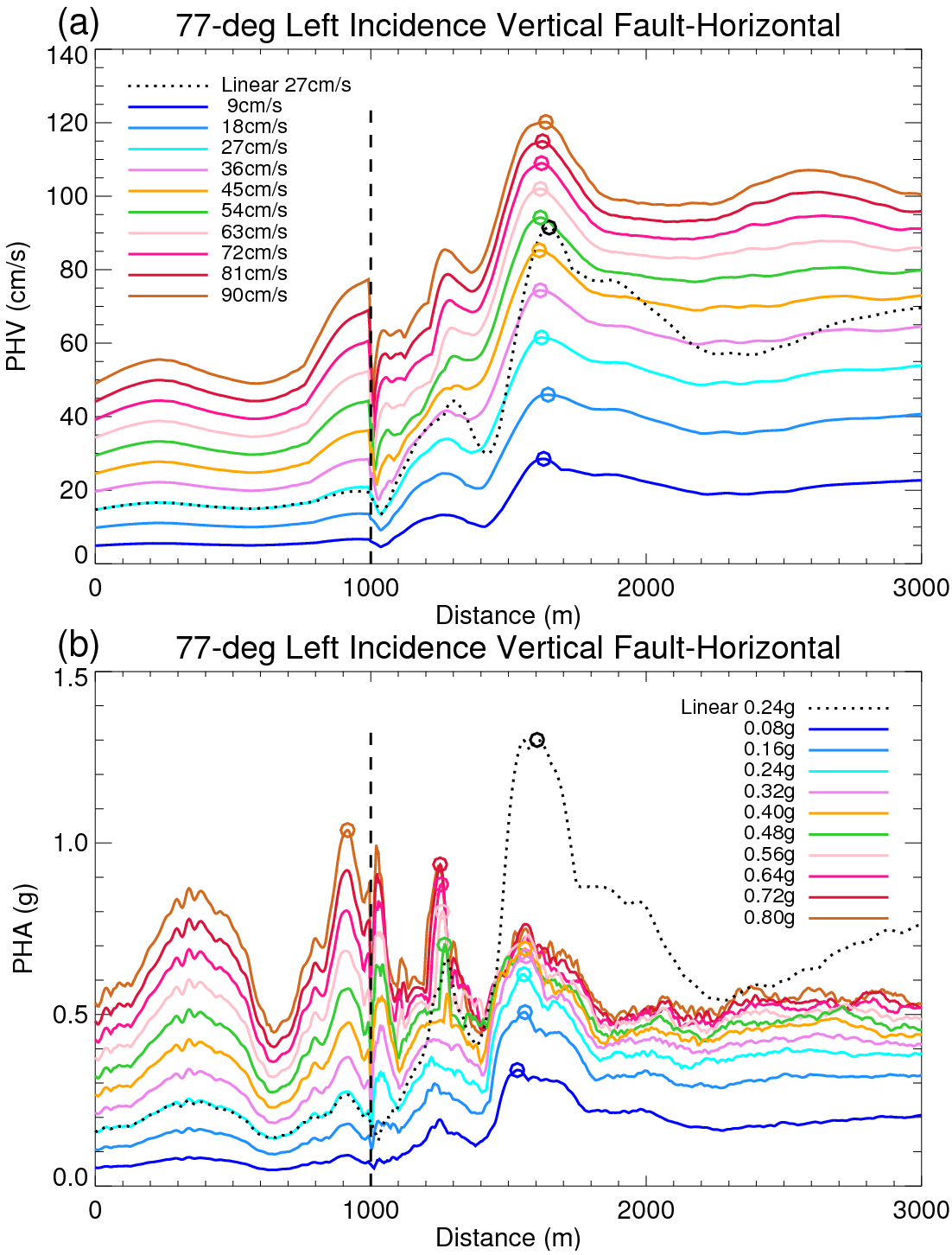

Figure 29. Incident at 77-degrees from the left with vertical-basin-edge 2D velocity model PHV (a) and PHA (b) as a function of horizontal position color-coded by corresponding uniform rock surface amplitude. The basin edge is located at 1000 m as indicated by the vertical dashed lines in (a) and (b), with the basin to the right. The maximum amplitude for each input amplitude curves within or close to the basin is indicated by circles color-coded by peak input amplitude.

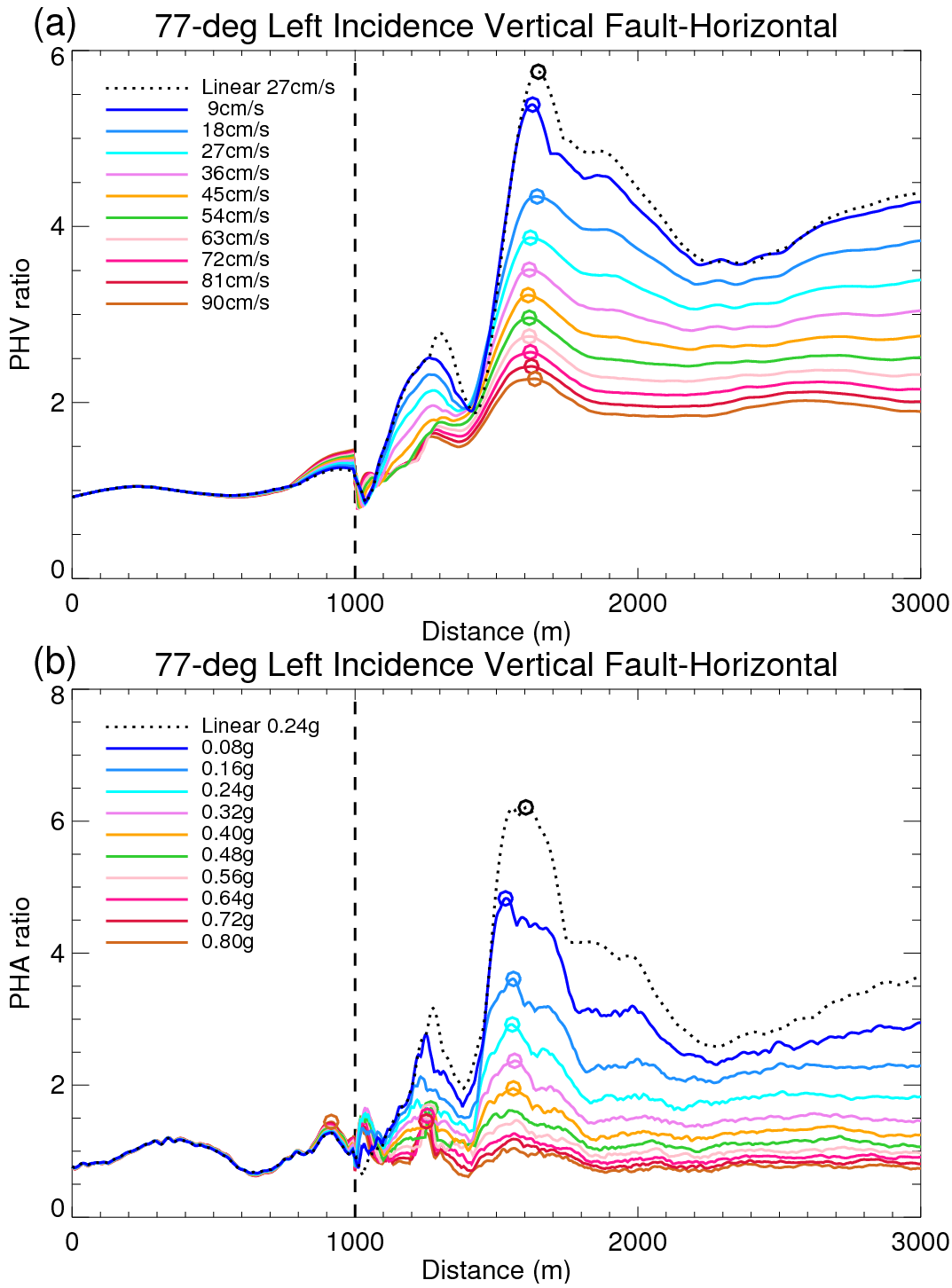

Figure 30. Incident at 77-degrees from the left with vertical-basin-edge 2D velocity model PHV ratio relative to linear rock (a) and PHA ratio relative to linear rock (b) as a function of horizontal position color-coded by corresponding uniform rock surface amplitude. The basin edge is located at 1000 m as indicated by the vertical dashed lines in (a) and (b), with the basin to the right. The maximum amplitude for each input amplitude curves is indicated by circles color-coded by peak input amplitude.

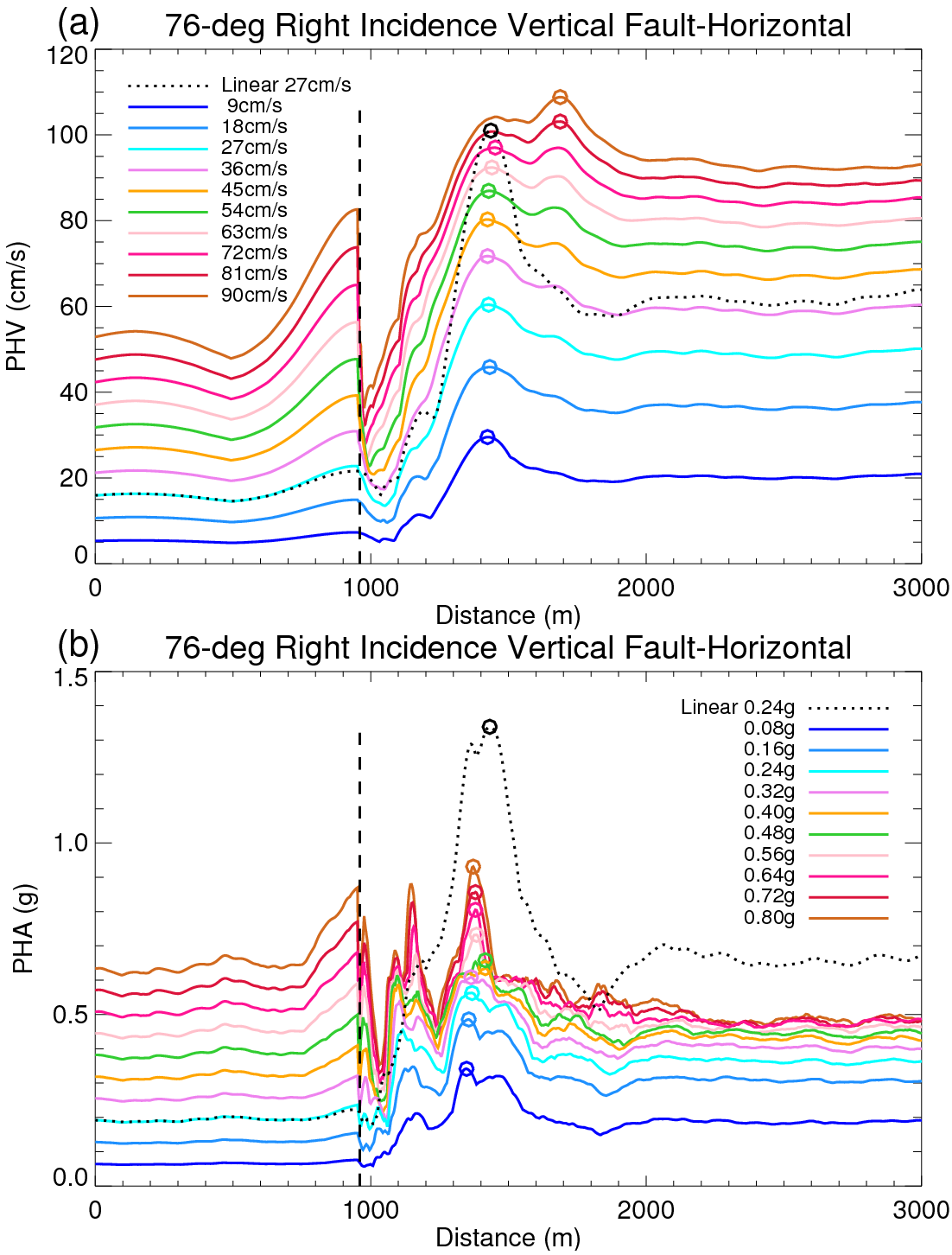

Figure 31. Incident at 76-degrees from the right with vertical-basin-edge 2D velocity model PHV (a) and PHA (b) as a function of horizontal position color-coded by corresponding uniform rock surface amplitude. The basin edge is located at 960 m as indicated by the vertical dashed lines in (a) and (b), with the basin to the right. The maximum amplitude for each input amplitude curves within or close to the basin is indicated by circles color-coded by peak input amplitude.

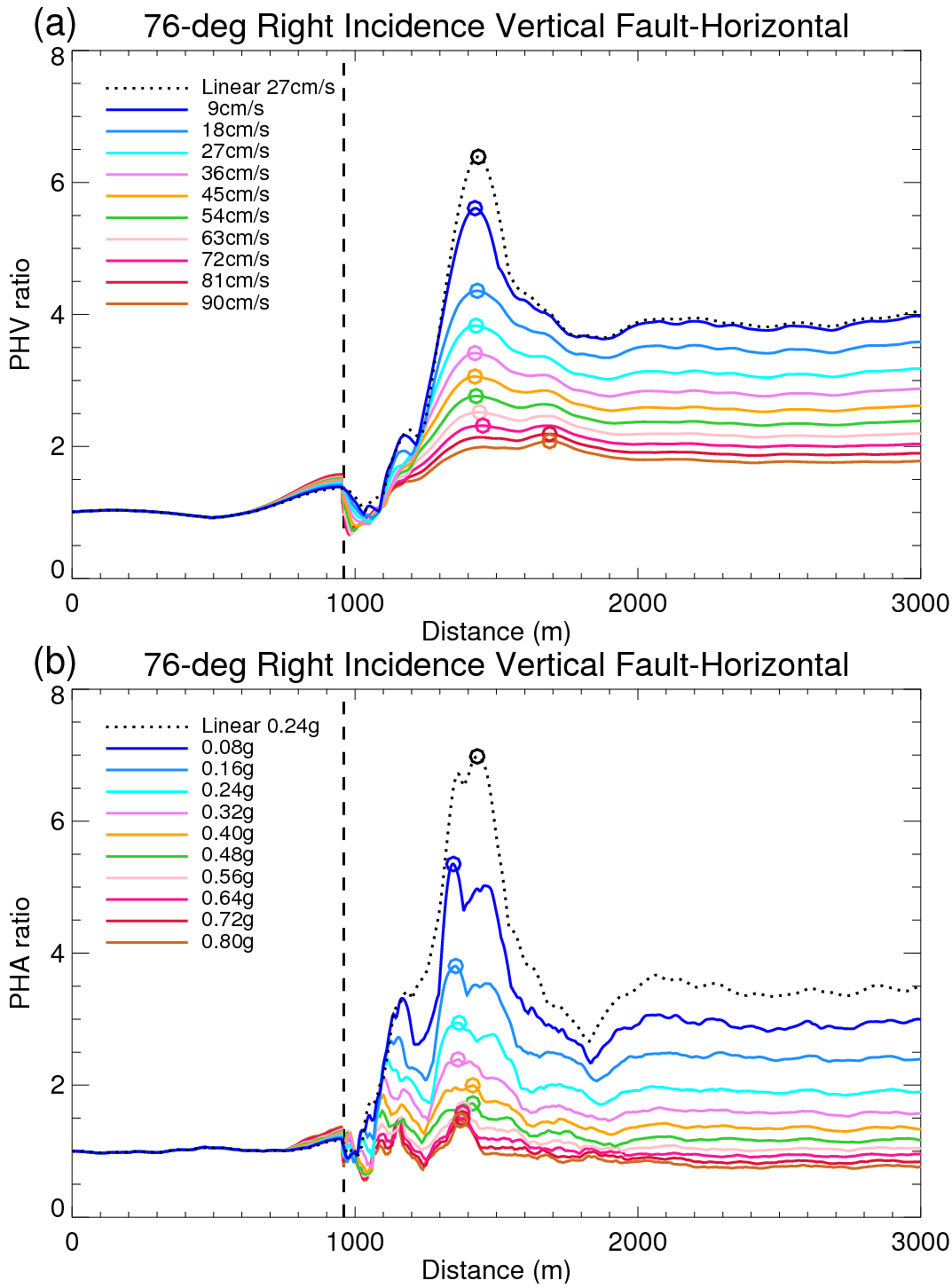

Figure 32. Incident at 76-degrees from the right with vertical-basin-edge 2D velocity model PHV ratio relative to linear rock (a) and PHA ratio relative to linear rock (b) as a function of horizontal position color-coded by corresponding uniform rock surface amplitude. The basin edge is located at 960 m as indicated by the vertical dashed lines in (a) and (b), with the basin to the right. The maximum amplitude for each input amplitude curves is indicated by circles color-coded by peak input amplitude.

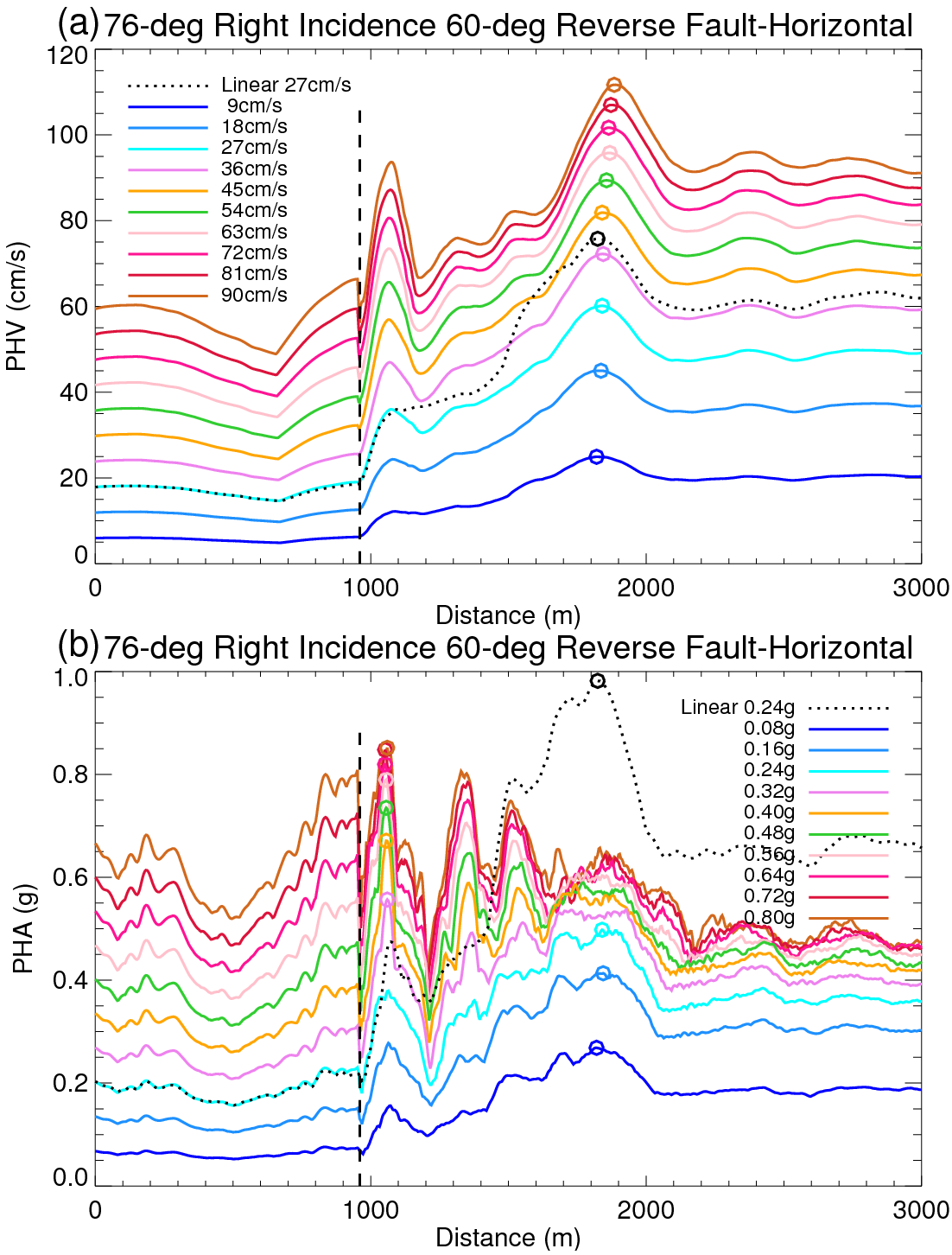

Figure 33. Incident at 76-degrees from the right with a 60-degree-dip reverse fault 2D velocity PHV (a) and PHA (b) as a function of horizontal position color-coded by corresponding uniform rock surface amplitude. The basin edge is located at 960 m as indicated by the vertical dashed lines in (a) and (b), with the basin to the right. The maximum amplitude for each input amplitude curves within or close to the basin is indicated by circles color-coded by peak input amplitude.

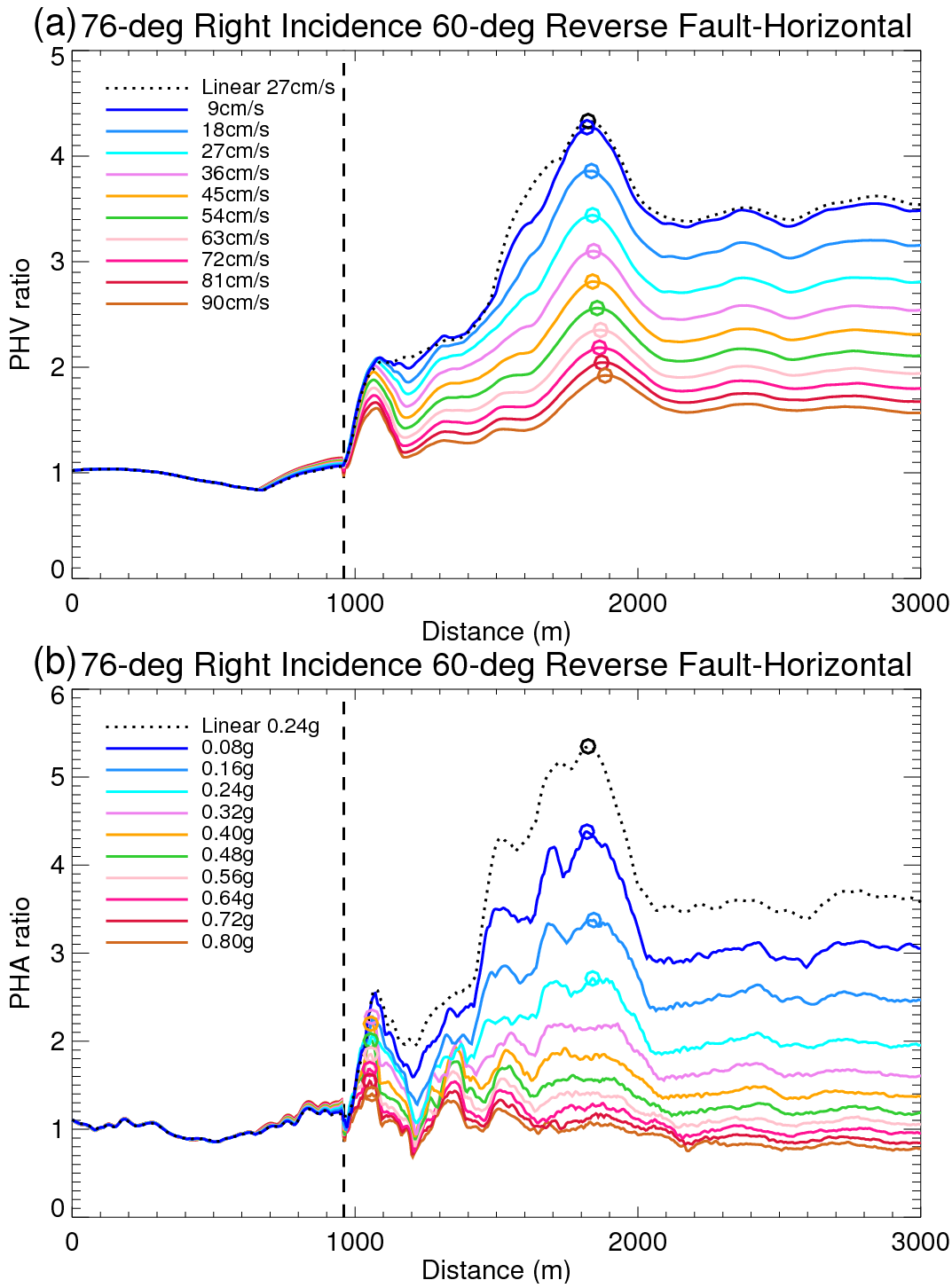

Figure 34. Incident at 76-degrees from the right with a 60-degree-dip reverse fault 2D velocity PHV ratio relative to linear rock (a) and PHA ratio relative to linear rock (b) as a function of horizontal position color-coded by corresponding uniform rock surface amplitude. The basin edge is located at 960 m as indicated by the vertical dashed lines in (a) and (b), with the basin to the right. The maximum amplitude for each input amplitude curves is indicated by circles color-coded by peak input amplitude.

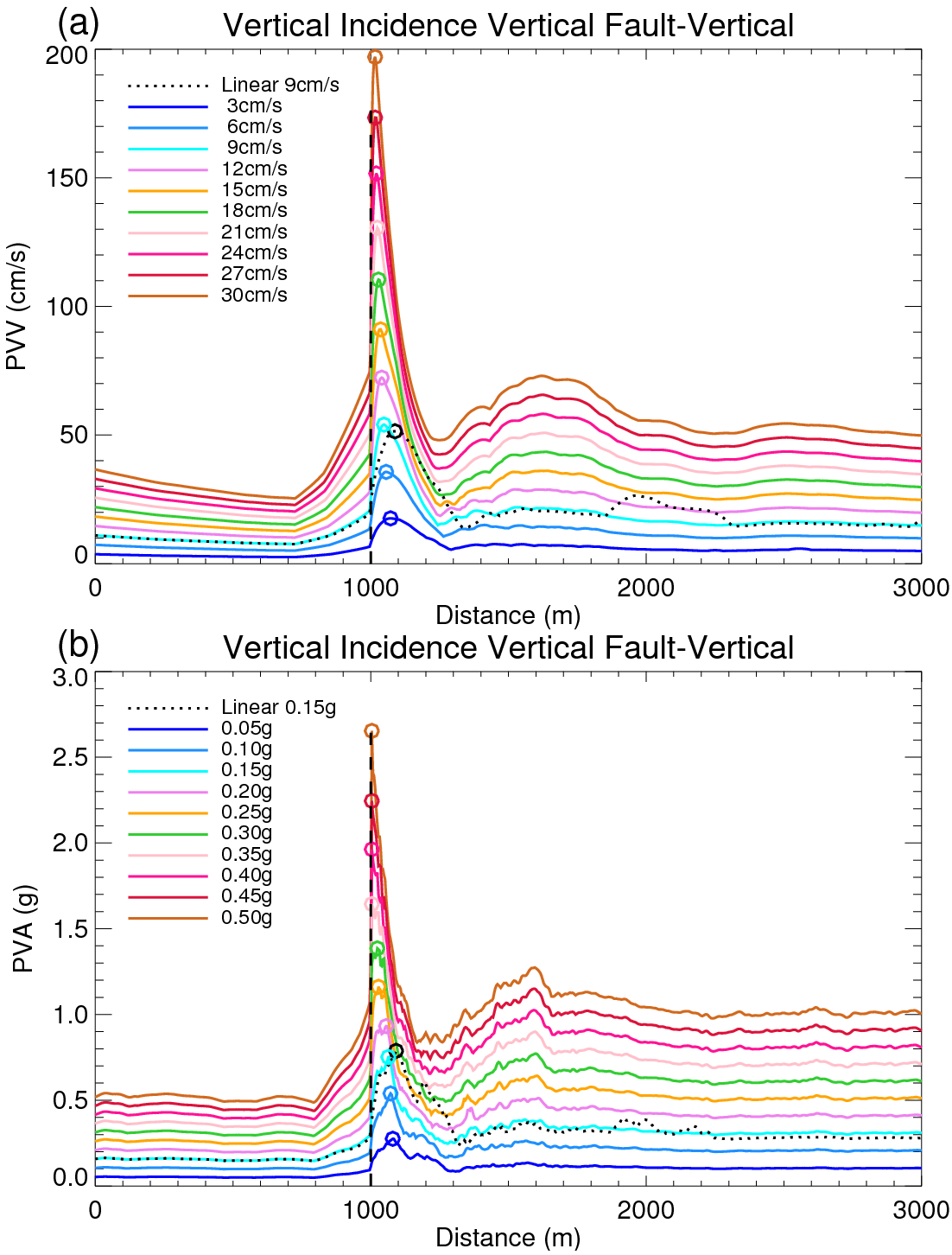

Figure 35. Vertically incident vertical-basin-edge 2D velocity model PVV (a) and PVA (b) as a function of horizontal position color-coded by corresponding uniform rock surface amplitude. The basin edge is located at 1000 m as indicated by the vertical dashed lines in (a) and (b), with the basin to the right. The maximum amplitude for each input amplitude curves within or close to the basin is indicated by circles color-coded by peak input amplitude.

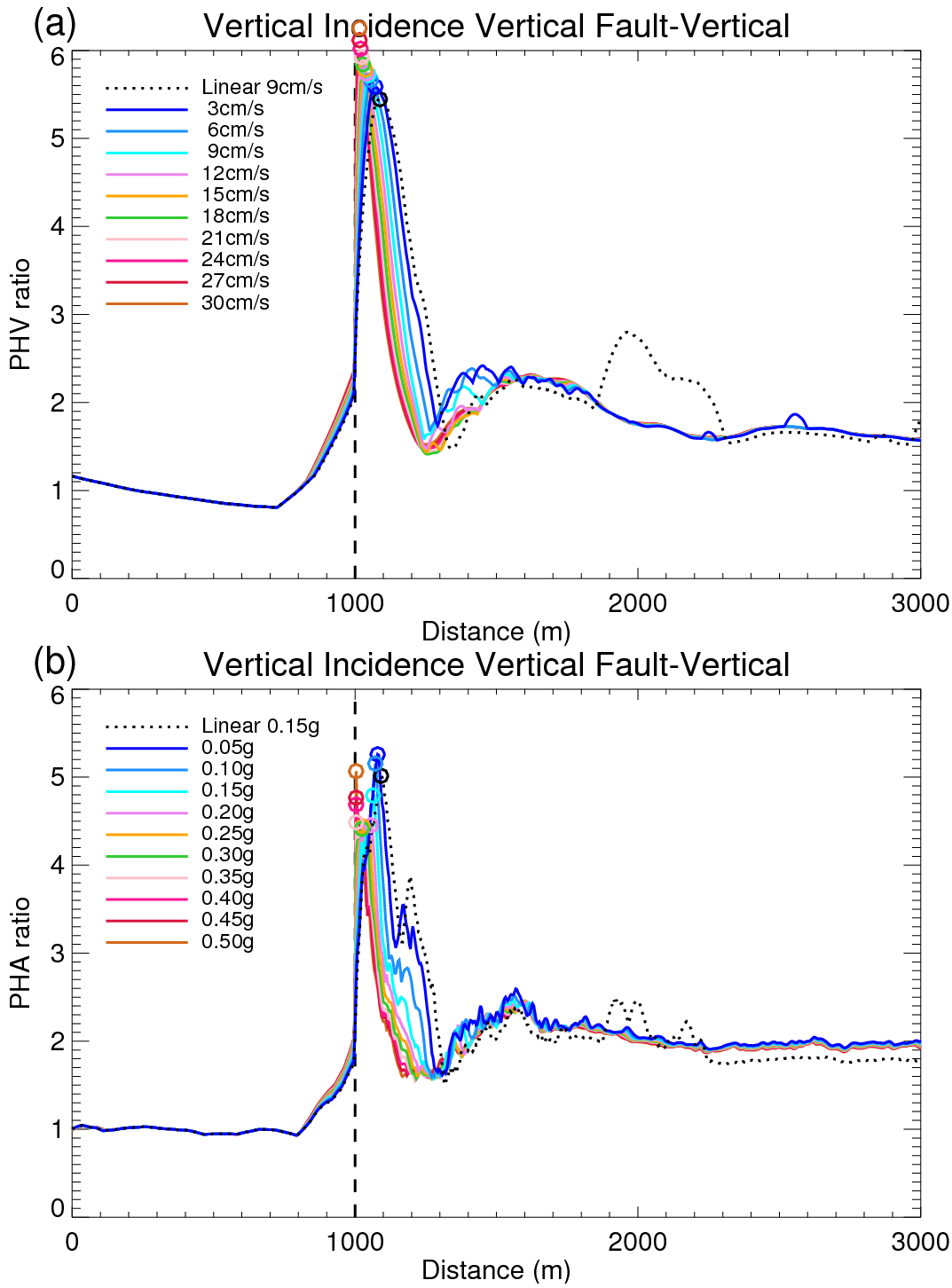

Figure 36. Vertically incident vertical-basin-edge 2D velocity model PVV ratio relative to linear rock (a) and PVA ratio relative to linear rock (b) as a function of horizontal position color-coded by corresponding uniform rock surface amplitude. The basin edge is located at 1000 m as indicated by the vertical dashed lines in (a) and (b), with the basin to the right. The maximum amplitude for each input amplitude curves within or close to the basin is indicated by circles color-coded by peak input amplitude.

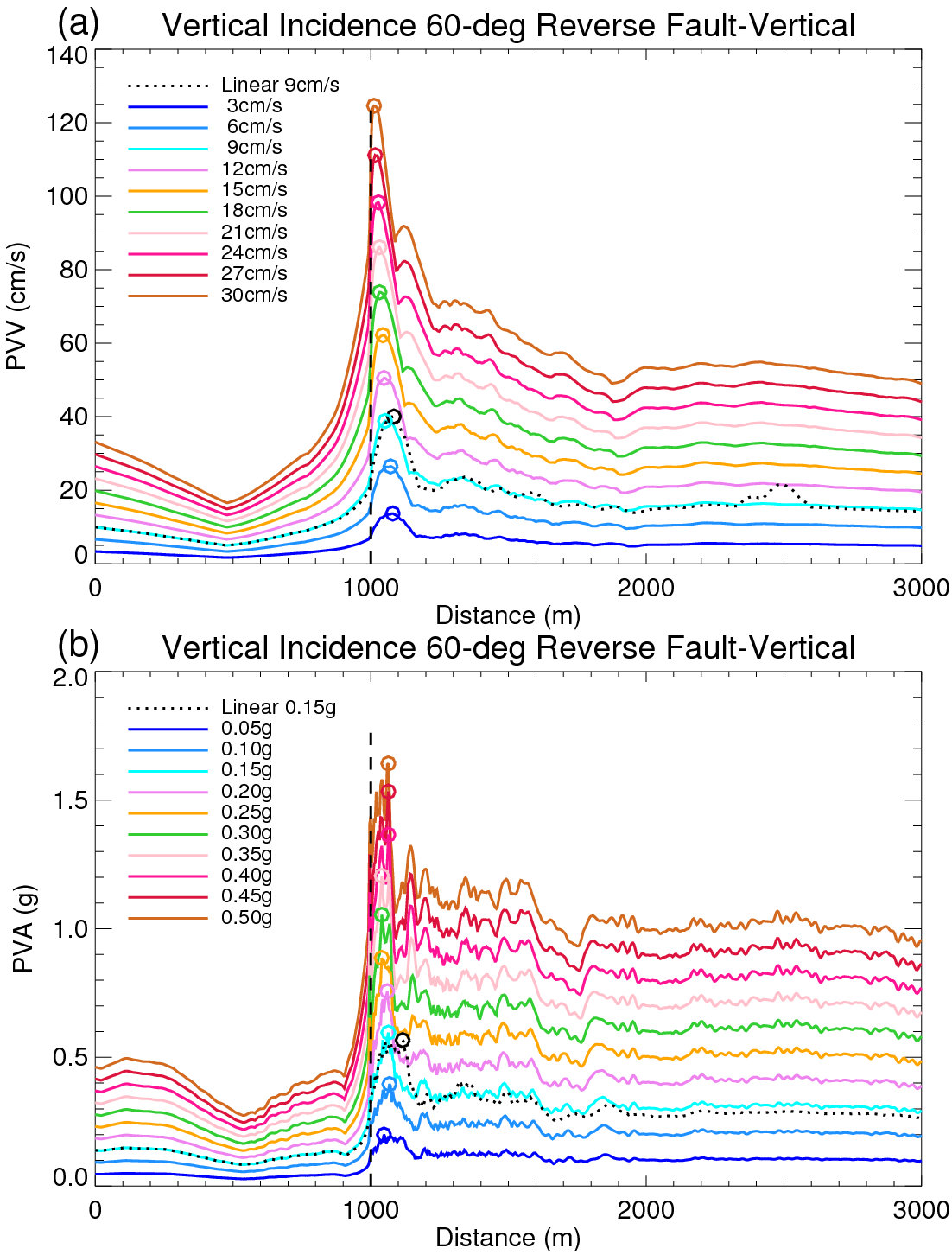

Figure 37. Vertically-incident 60-degree-dip reverse fault 2D velocity PVV (a) and PVA (b) as a function of horizontal position color-coded by corresponding uniform rock surface amplitude. The basin edge is located at 1000 m as indicated by the vertical dashed lines in (a) and (b), with the basin to the right. The maximum amplitude for each input amplitude curves within or close to the basin is indicated by circles color-coded by peak input amplitude.

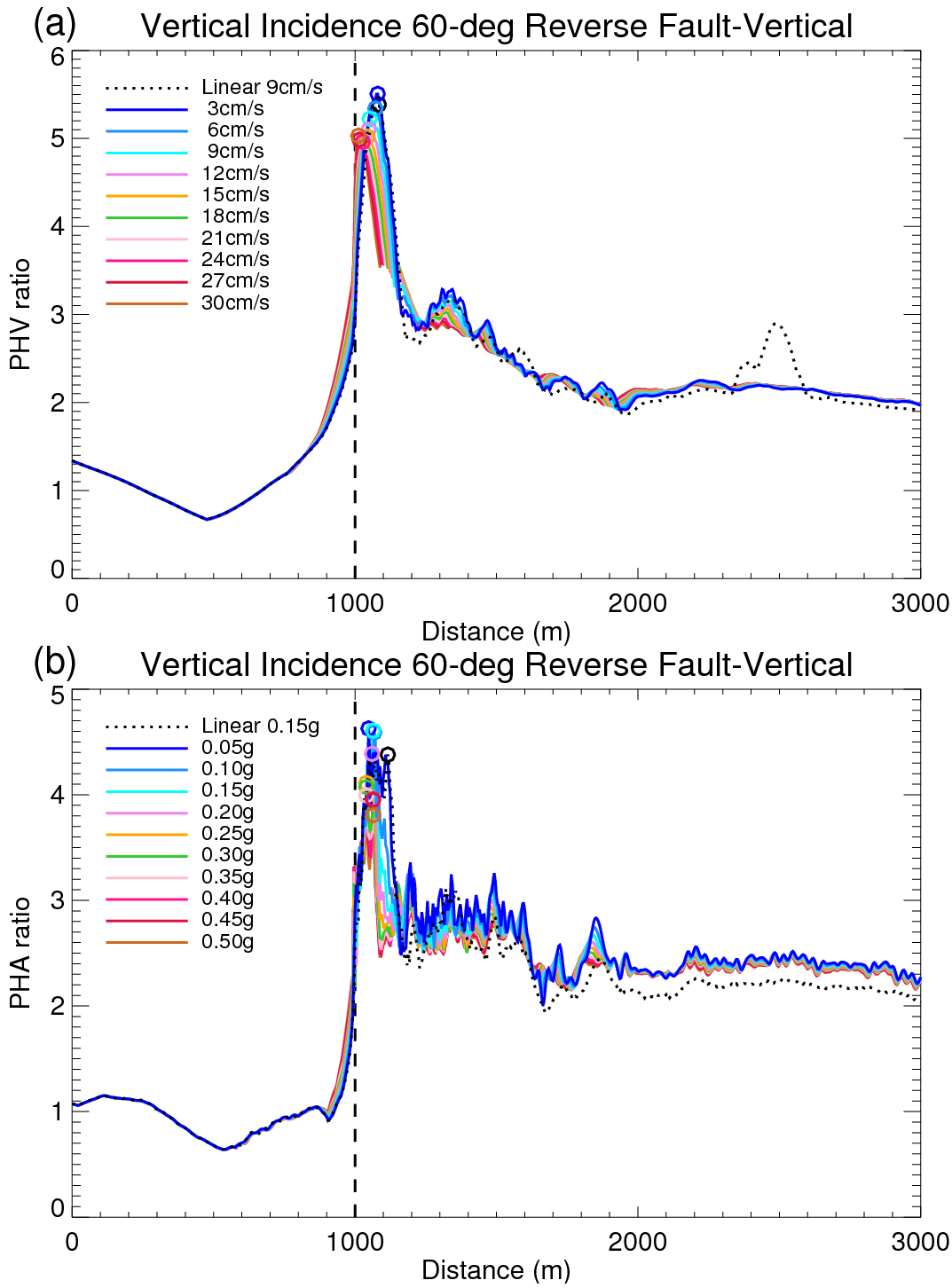

Figure 38. Vertically-incident 60-degree-dip reverse fault 2D velocity PVV ratio relative to linear rock (a) and PVA ratio relative to linear rock (b) as a function of horizontal position color-coded by corresponding uniform rock surface amplitude. The basin edge is located at 1000 m as indicated by the vertical dashed lines in (a) and (b), with the basin to the right. The maximum amplitude for each input amplitude curves within or close to the basin is indicated by circles color-coded by peak input amplitude.

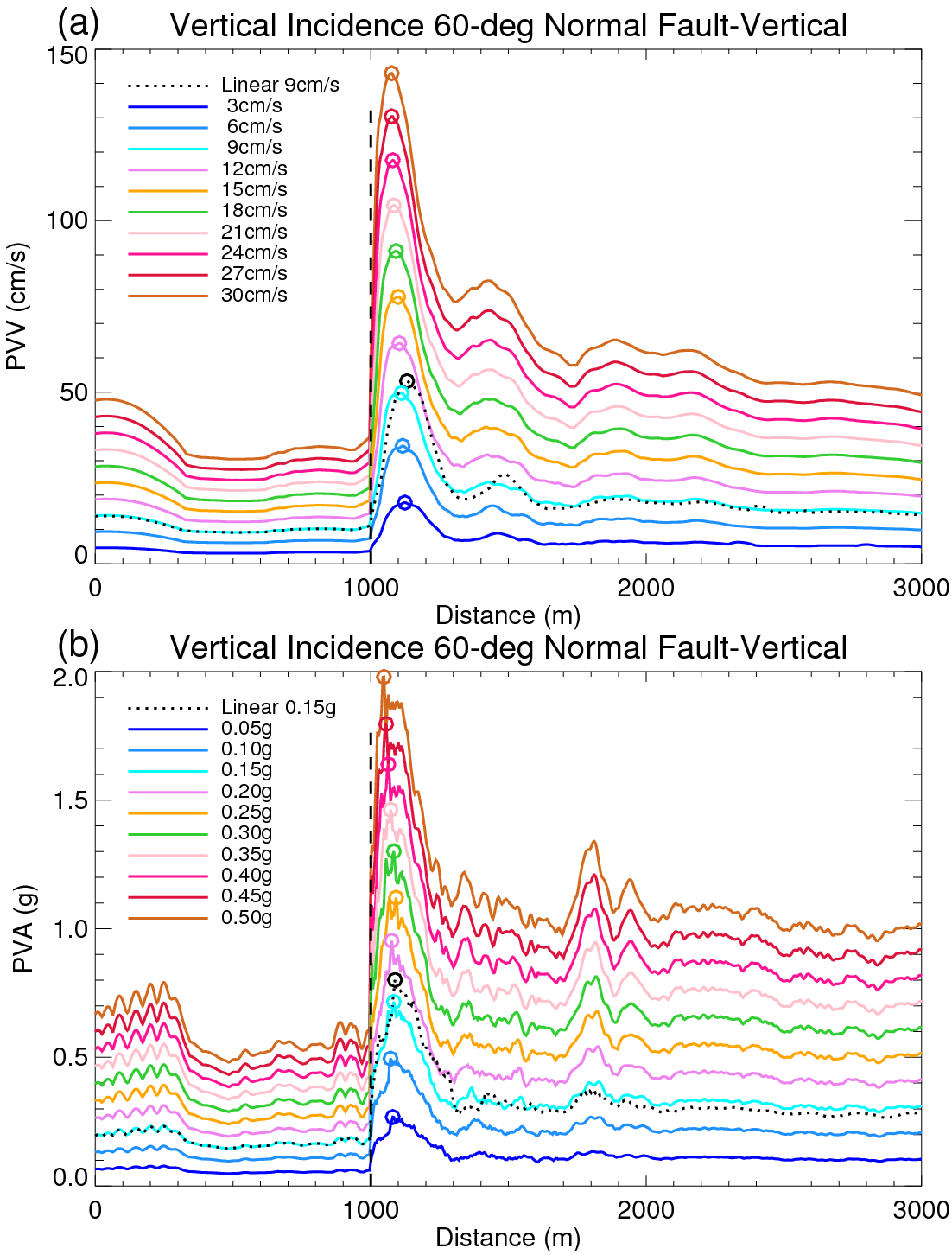

Figure 39. Vertically-incident 60-degree-dip normal fault 2D velocity model PVV (a) and PVA (b) as a function of horizontal position color-coded by corresponding uniform rock surface amplitude. The basin edge is located at 1000 m as indicated by the vertical dashed lines in (a) and (b), with the basin to the right. The maximum amplitude for each input amplitude curves within or close to the basin is indicated by circles color-coded by peak input amplitude.

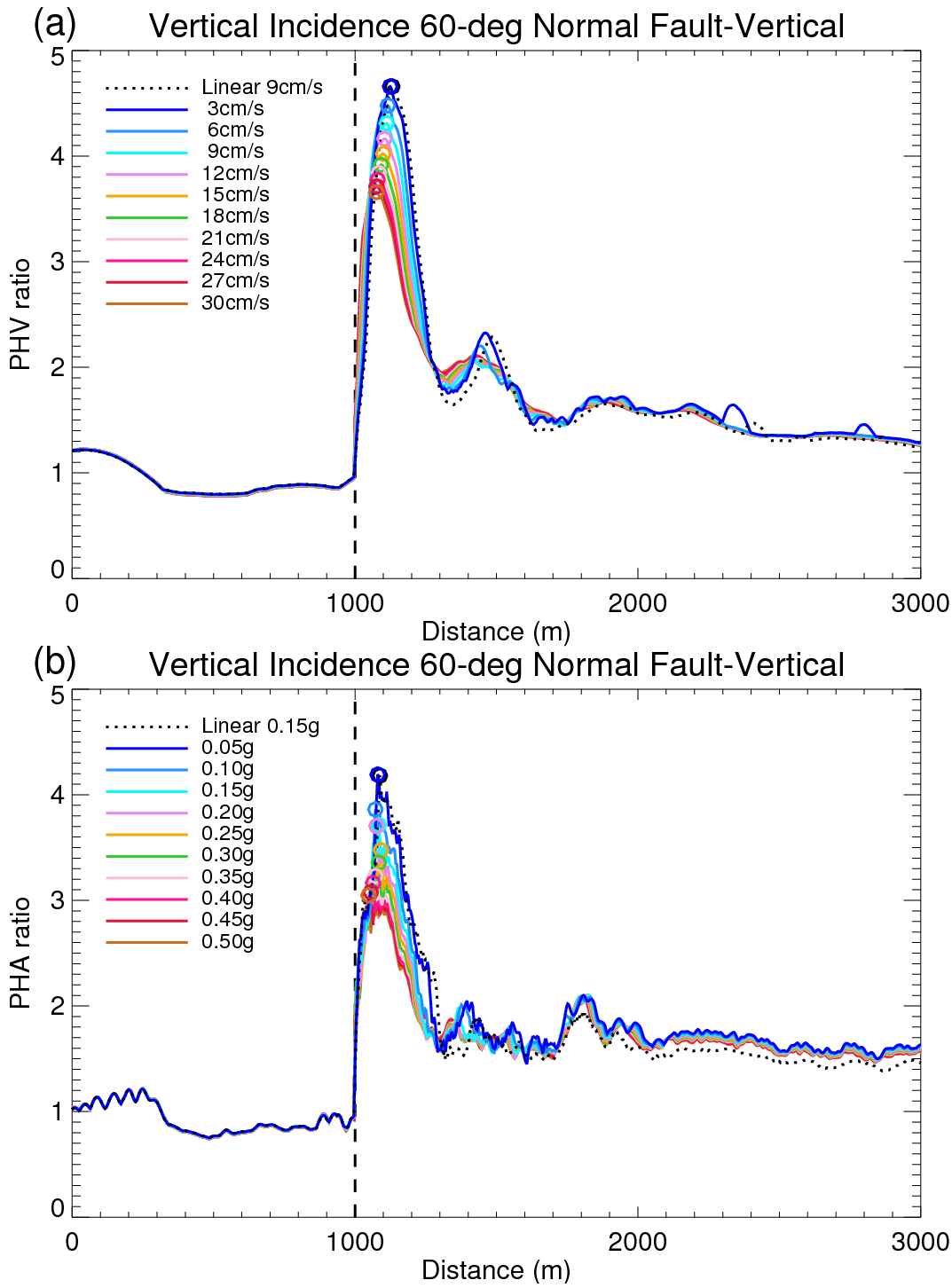

Figure 40. Vertically-incident 60-degree-dip normal fault 2D velocity model PVV ratio relative to linear rock (a) and PVA ratio relative to linear rock (b) as a function of horizontal position color-coded by corresponding uniform rock surface amplitude. The basin edge is located at 1000 m as indicated by the vertical dashed lines in (a) and (b), with the basin to the right. The maximum amplitude for each input amplitude curves within or close to the basin is indicated by circles color-coded by peak input amplitude.

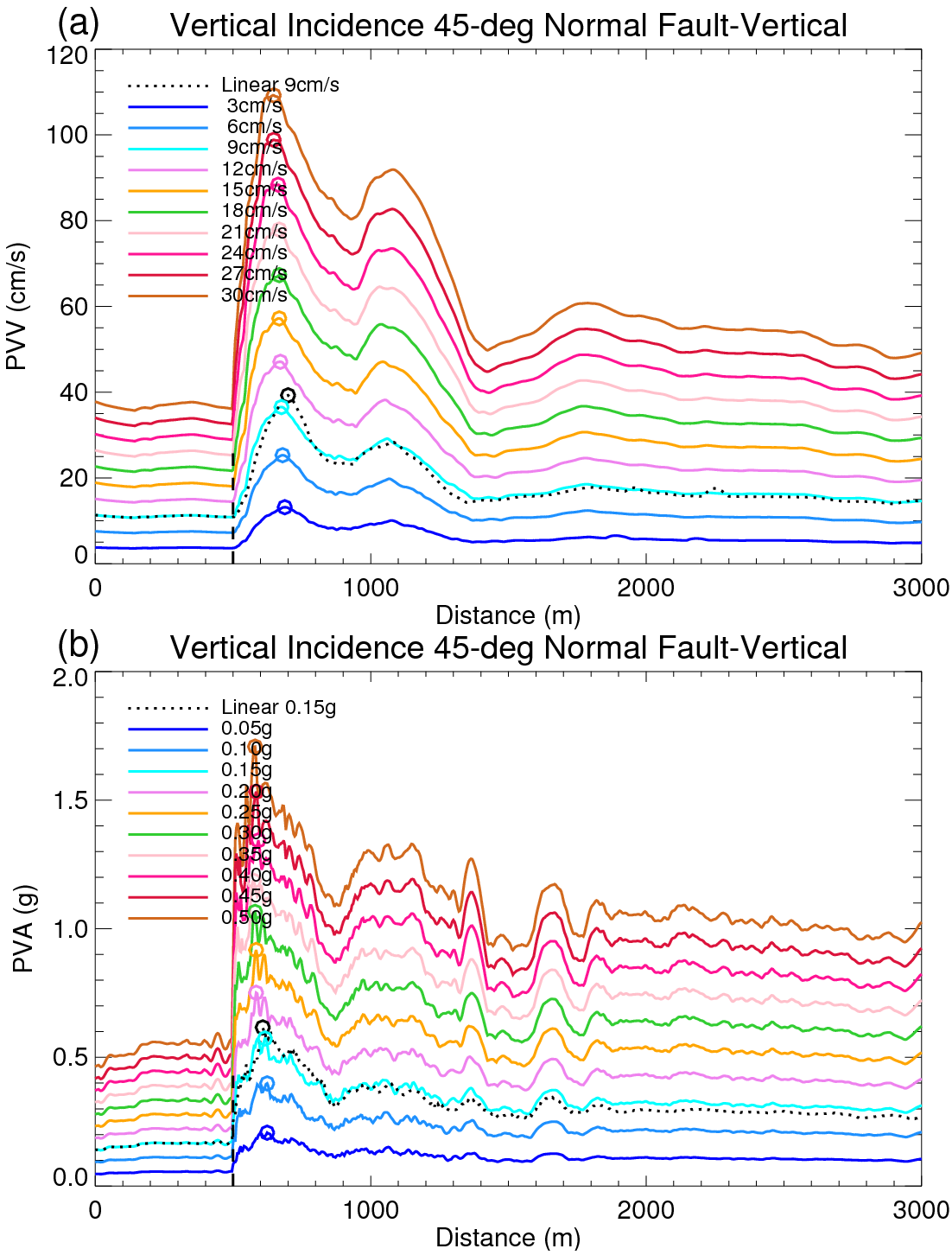

Figure 41. Vertically-incident 45-degree-dip normal fault 2D velocity model PVV (a) and PVA (b) as a function of horizontal position color-coded by corresponding uniform rock surface amplitude. The basin edge is located at 500 m as indicated by the vertical dashed lines in (a) and (b), with the basin to the right. The maximum amplitude for each input amplitude curves within the basin is indicated by circles color-coded by peak input amplitude.

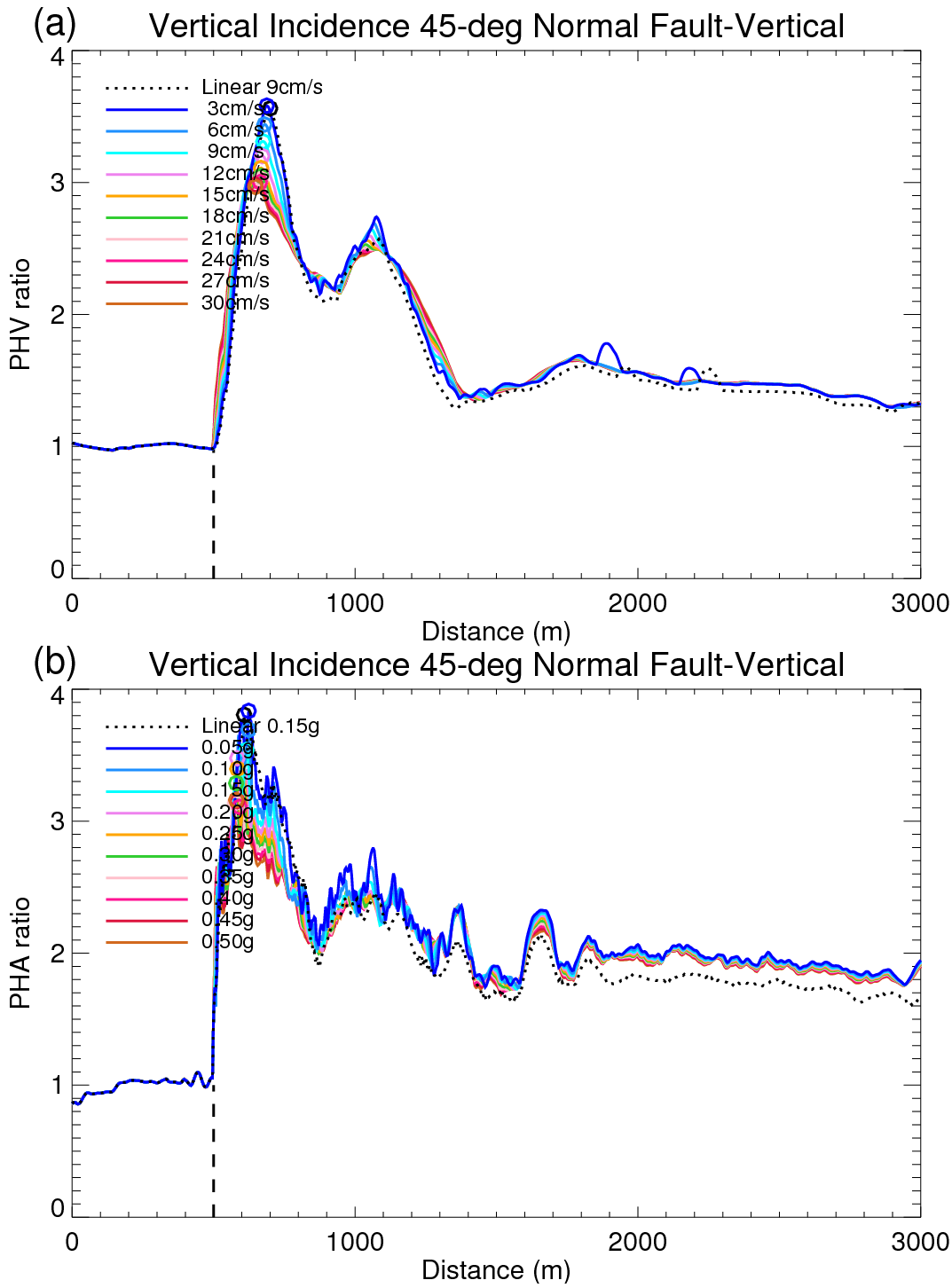

Figure 42. Vertically-incident 45-degree-dip normal fault 2D velocity model PVV ratio relative to linear rock (a) and PVA ratio relative to linear rock (b) as a function of horizontal position color-coded by corresponding uniform rock surface amplitude. The basin edge is located at 500 m as indicated by the vertical dashed lines in (a) and (b), with the basin to the right. The maximum amplitude for each input amplitude curves within the basin is indicated by circles color-coded by peak input amplitude.

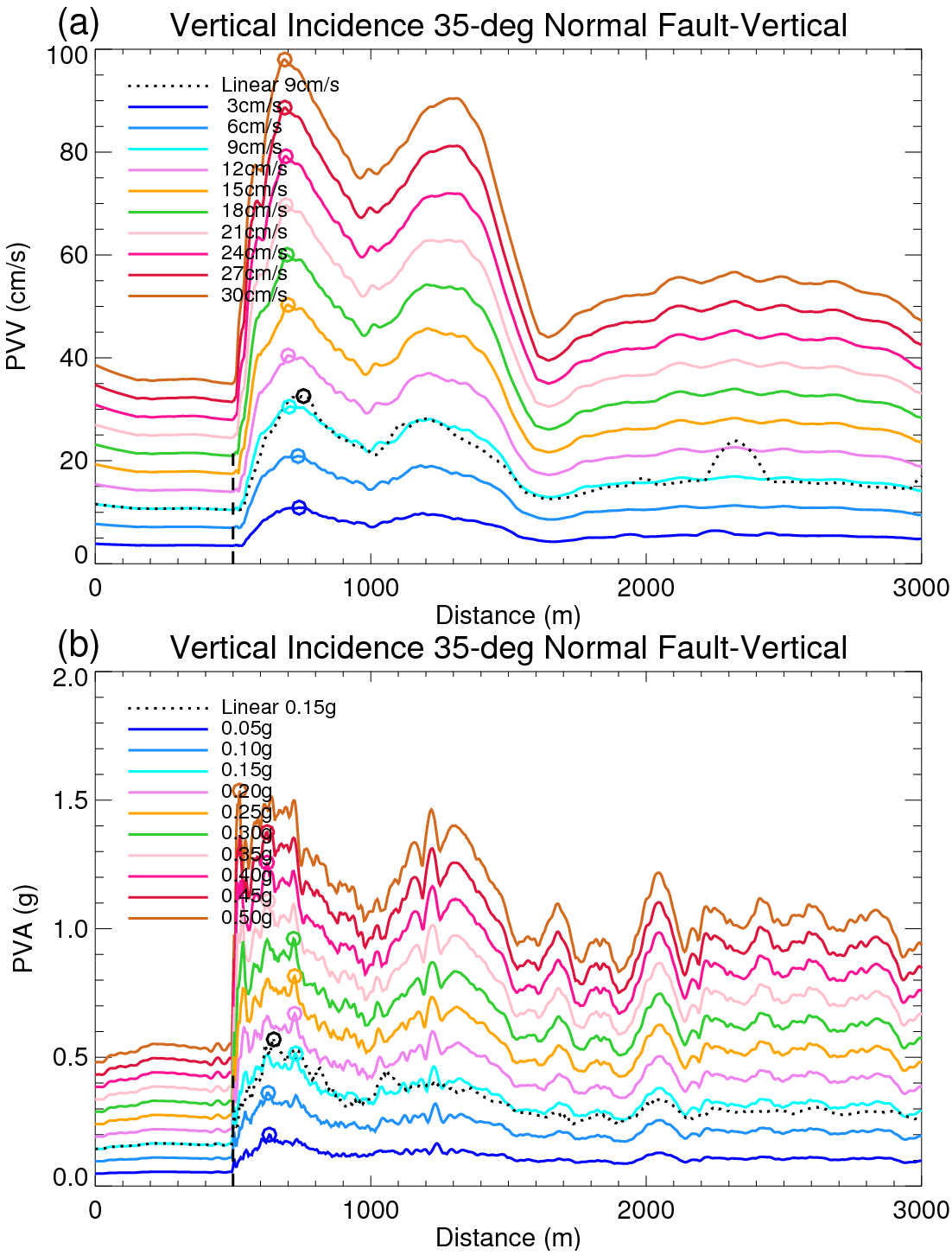

Figure 43. Vertically-incident 35-degree-dip normal fault 2D velocity model PVV (a) and PVA (b). See Figure 6 for details. The basin edge is located at 500 m as indicated by the vertical dashed lines in (a) and (b), with the basin to the right. The maximum amplitude for each input amplitude curves within the basin is indicated by circles color-coded by peak input amplitude. The maximum nonlinear PVA migrates toward the fault as input PVA increases in (b).

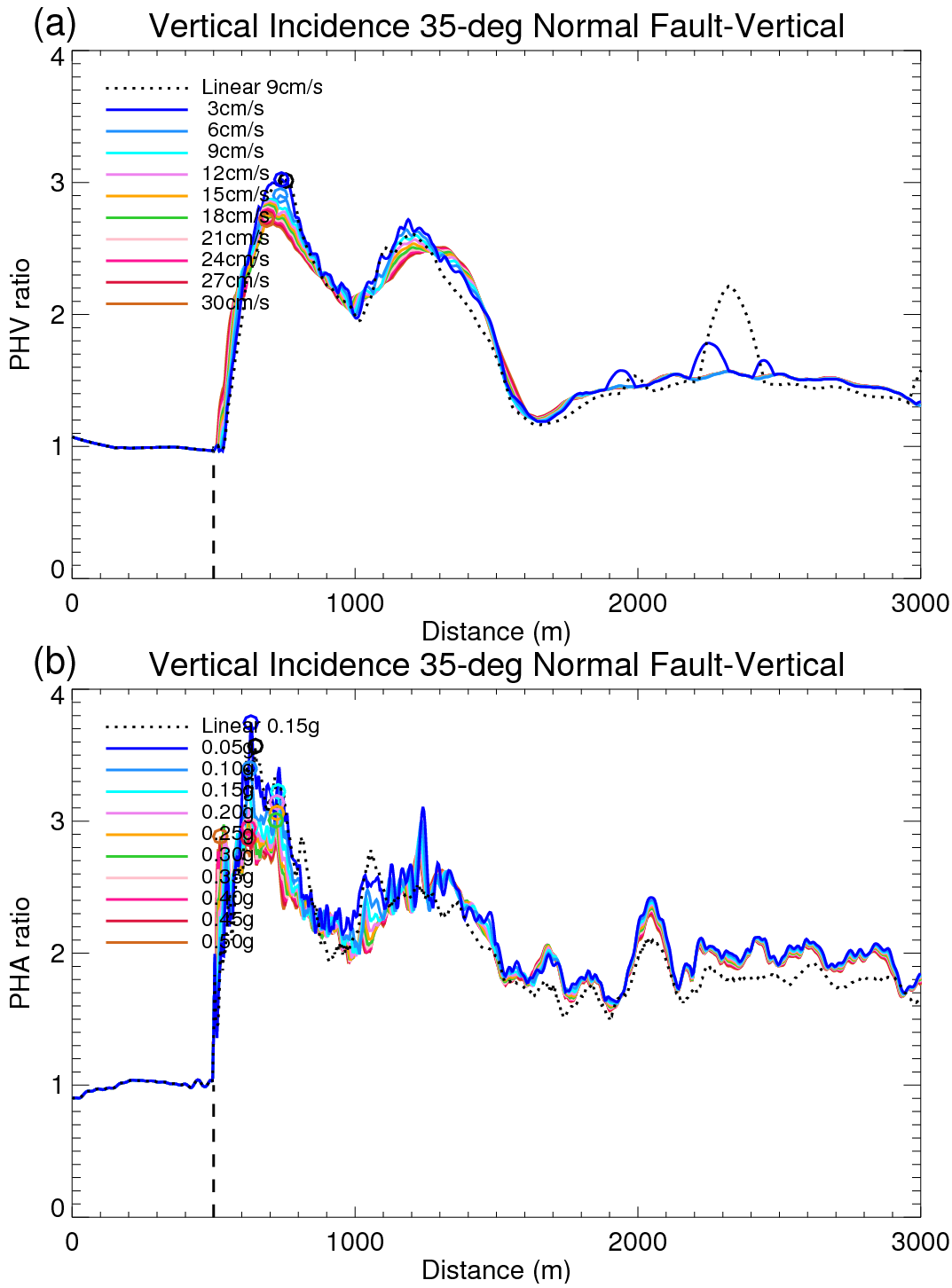

Figure 44. Vertically-incident 35-degree-dip normal fault 2D velocity model PVV ratio relative to linear rock (a) and PVA ratio relative to linear rock (b). The basin edge is located at 500 m as indicated by the vertical dashed lines in (a) and (b), with the basin to the right. The maximum amplitude for each input amplitude curves within the basin is indicated by circles color-coded by peak input amplitude.

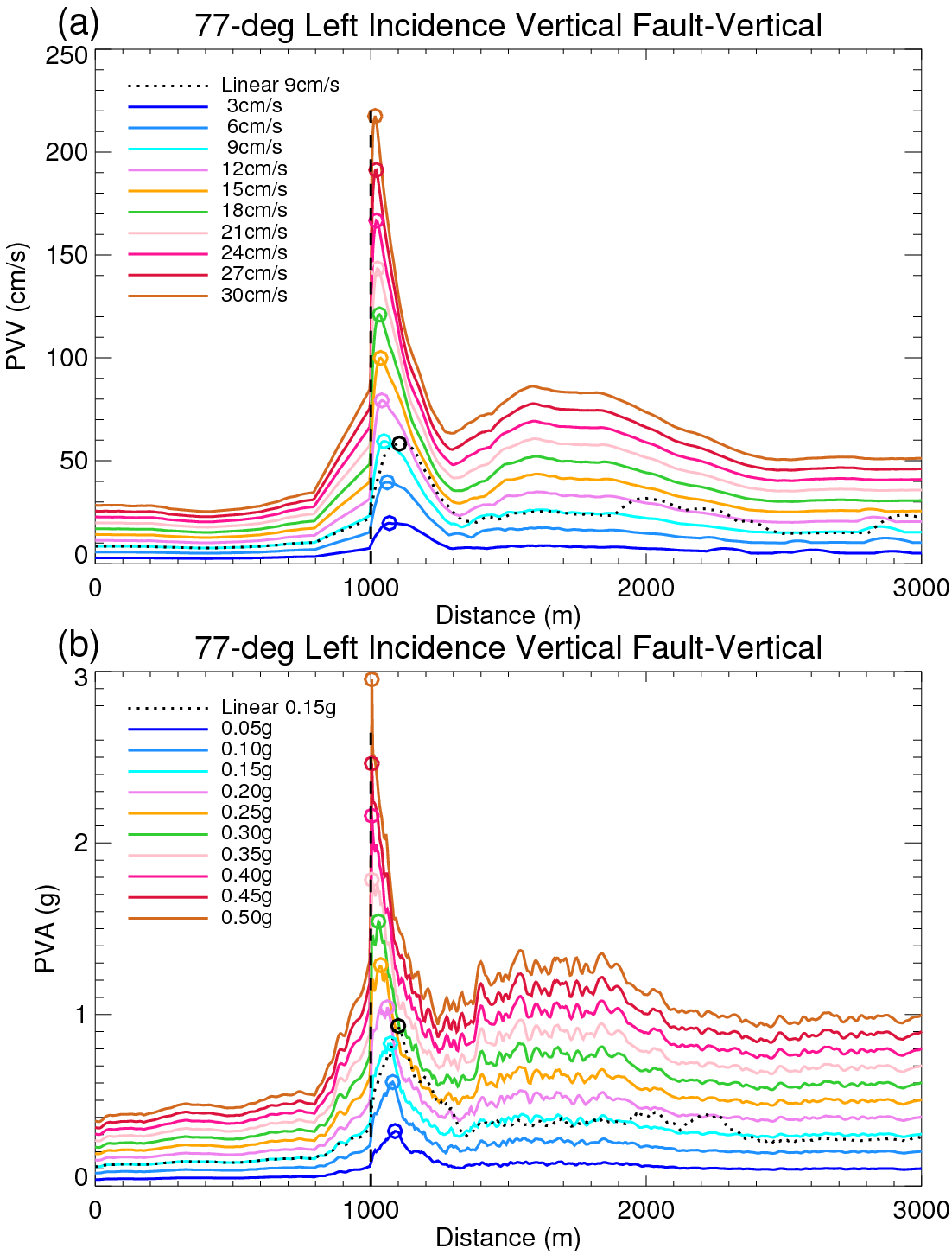

Figure 45. Incident at 77-degrees from the left with vertical-basin-edge 2D velocity model PVV (a) and PVA (b) as a function of horizontal position color-coded by corresponding uniform rock surface amplitude. The basin edge is located at 1000 m as indicated by the vertical dashed lines in (a) and (b), with the basin to the right. The maximum amplitude for each input amplitude curves within or close to the basin is indicated by circles color-coded by peak input amplitude.

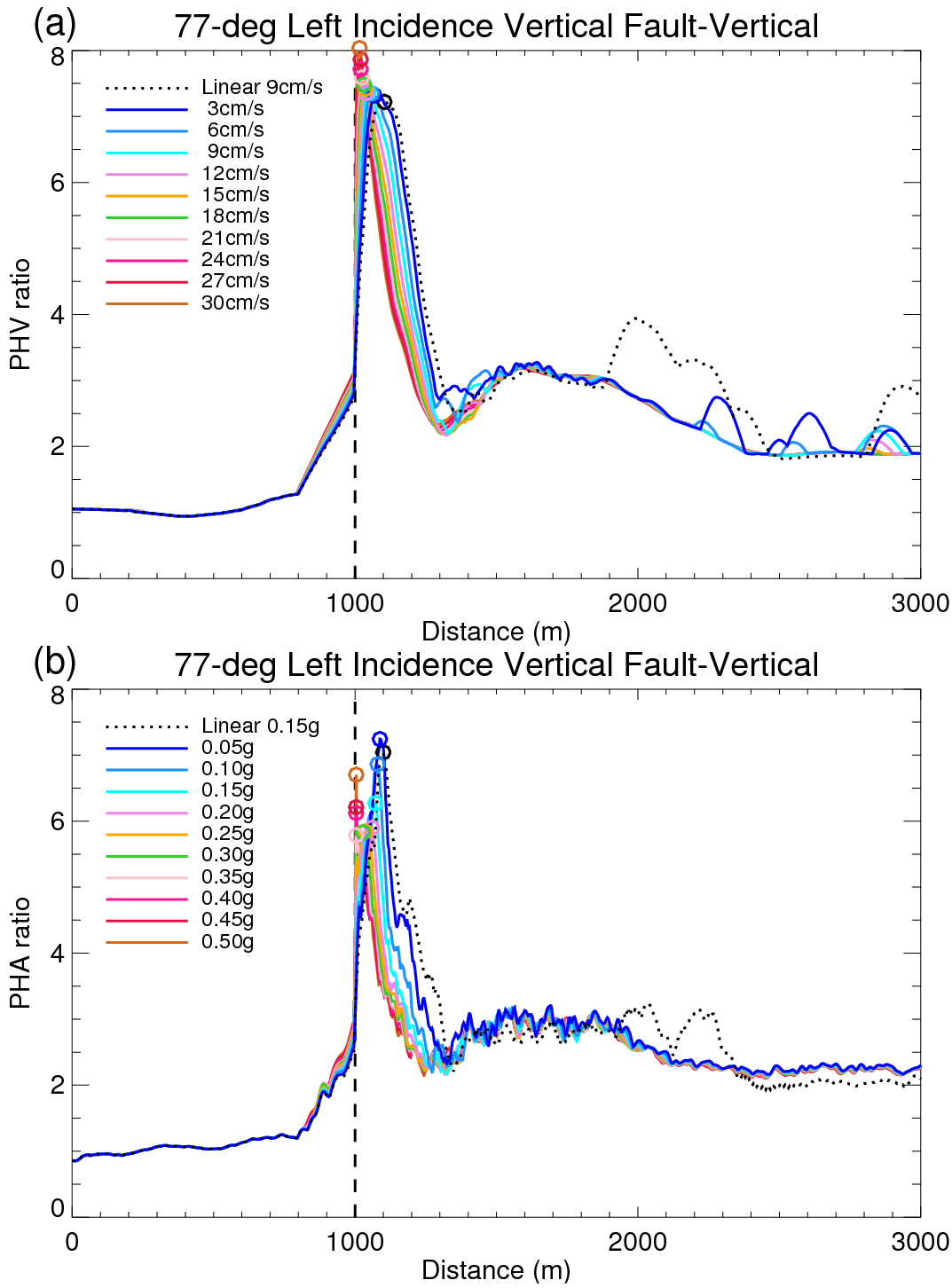

Figure 46. Incident at 77-degrees from the left with vertical-basin-edge 2D velocity model PVV ratio relative to linear rock (a) and PVA ratio relative to linear rock (b) as a function of horizontal position color-coded by corresponding uniform rock surface amplitude. The basin edge is located at 1000 m as indicated by the vertical dashed lines in (a) and (b), with the basin to the right. The maximum amplitude for each input amplitude curves is indicated by circles color-coded by peak input amplitude.

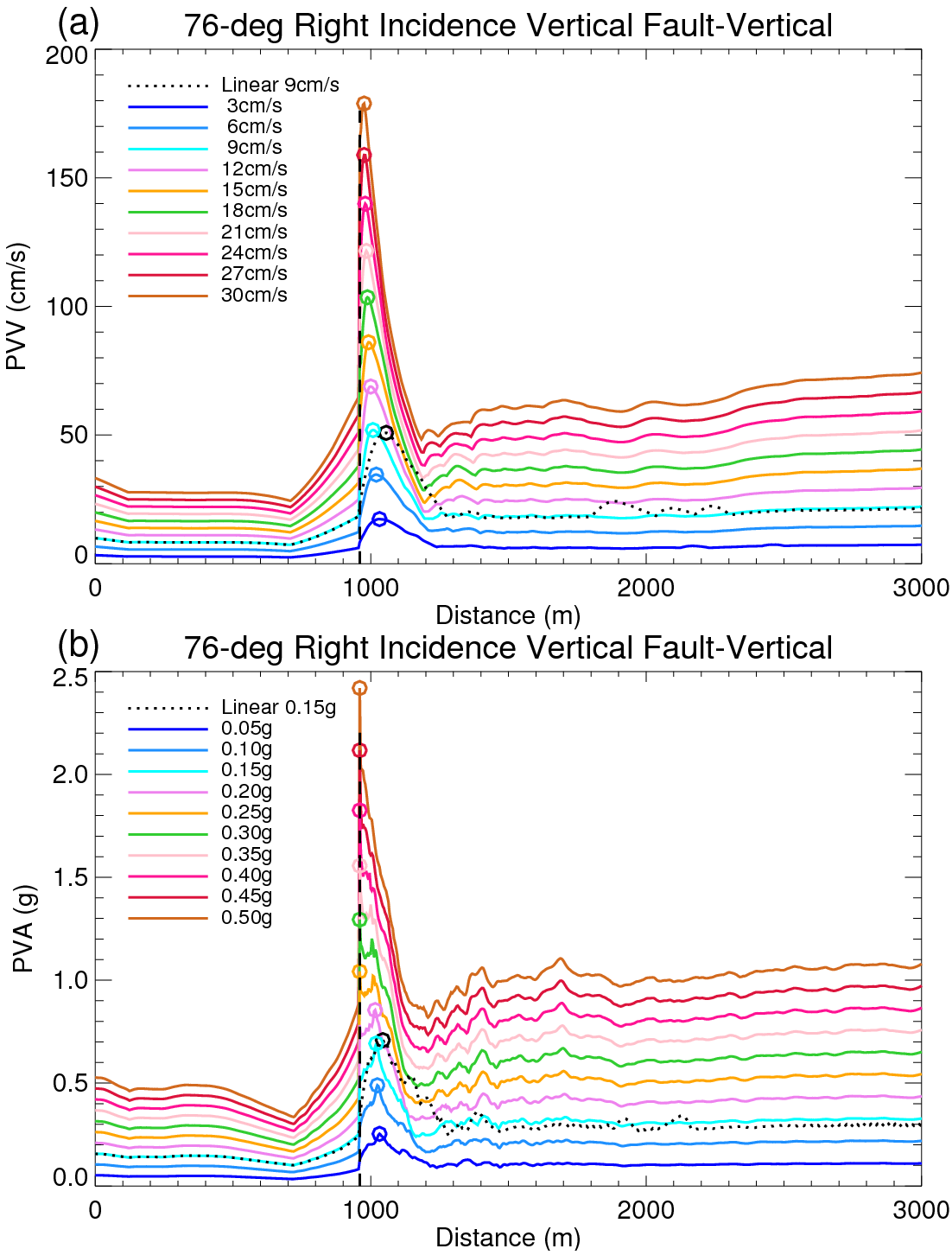

Figure 47. Incident at 76-degrees from the right with vertical-basin-edge 2D velocity model PVV (a) and PVA (b) as a function of horizontal position color-coded by corresponding uniform rock surface amplitude. The basin edge is located at 960 m as indicated by the vertical dashed lines in (a) and (b), with the basin to the right. The maximum amplitude for each input amplitude curves within or close to the basin is indicated by circles color-coded by peak input amplitude.

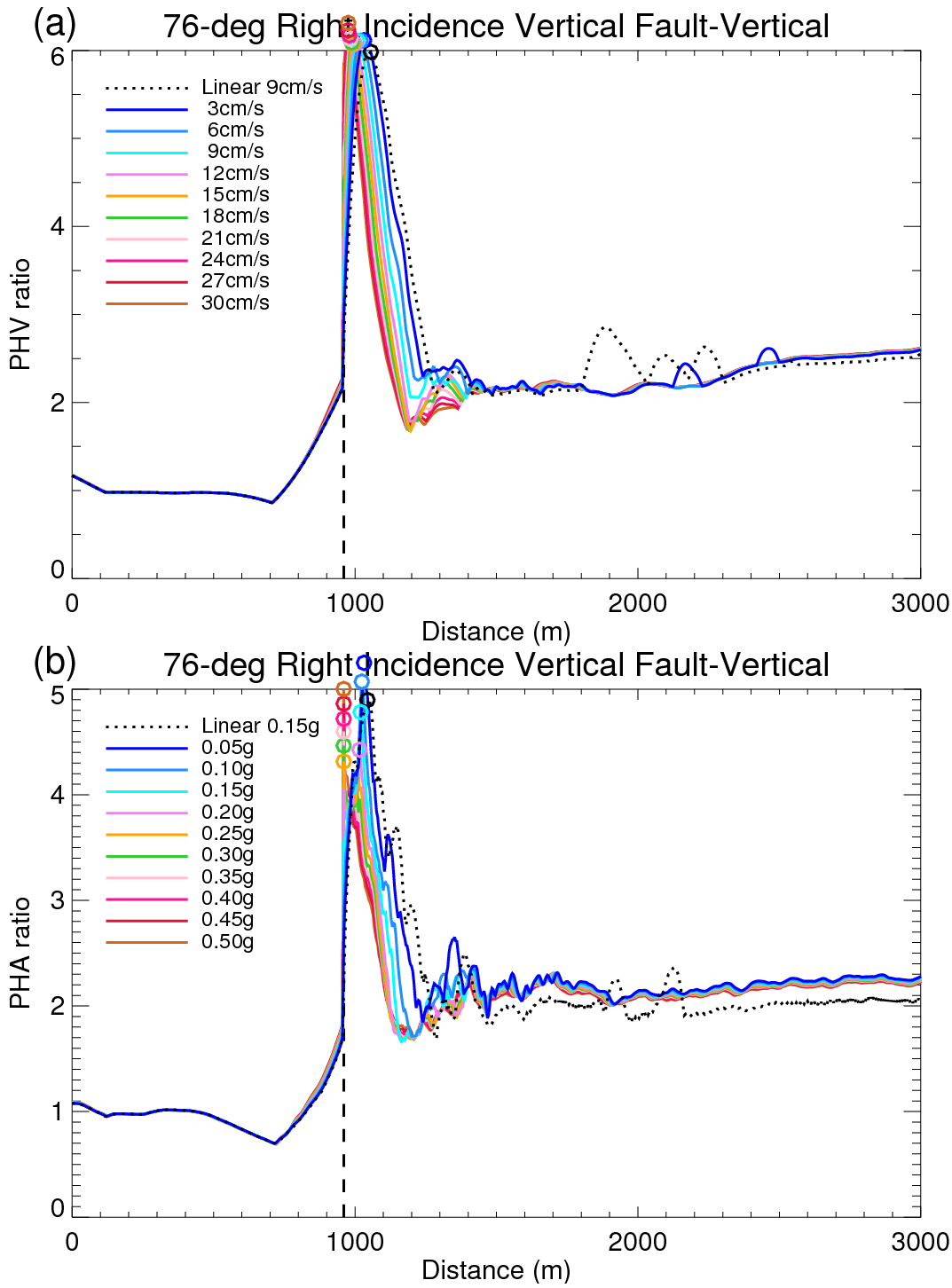

Figure 48. Incident at 76-degrees from the right with vertical-basin-edge 2D velocity model PVV ratio relative to linear rock (a) and PVA ratio relative to linear rock (b) as a function of horizontal position color-coded by corresponding uniform rock surface amplitude. The basin edge is located at 960 m as indicated by the vertical dashed lines in (a) and (b), with the basin to the right. The maximum amplitude for each input amplitude curves is indicated by circles color-coded by peak input amplitude.

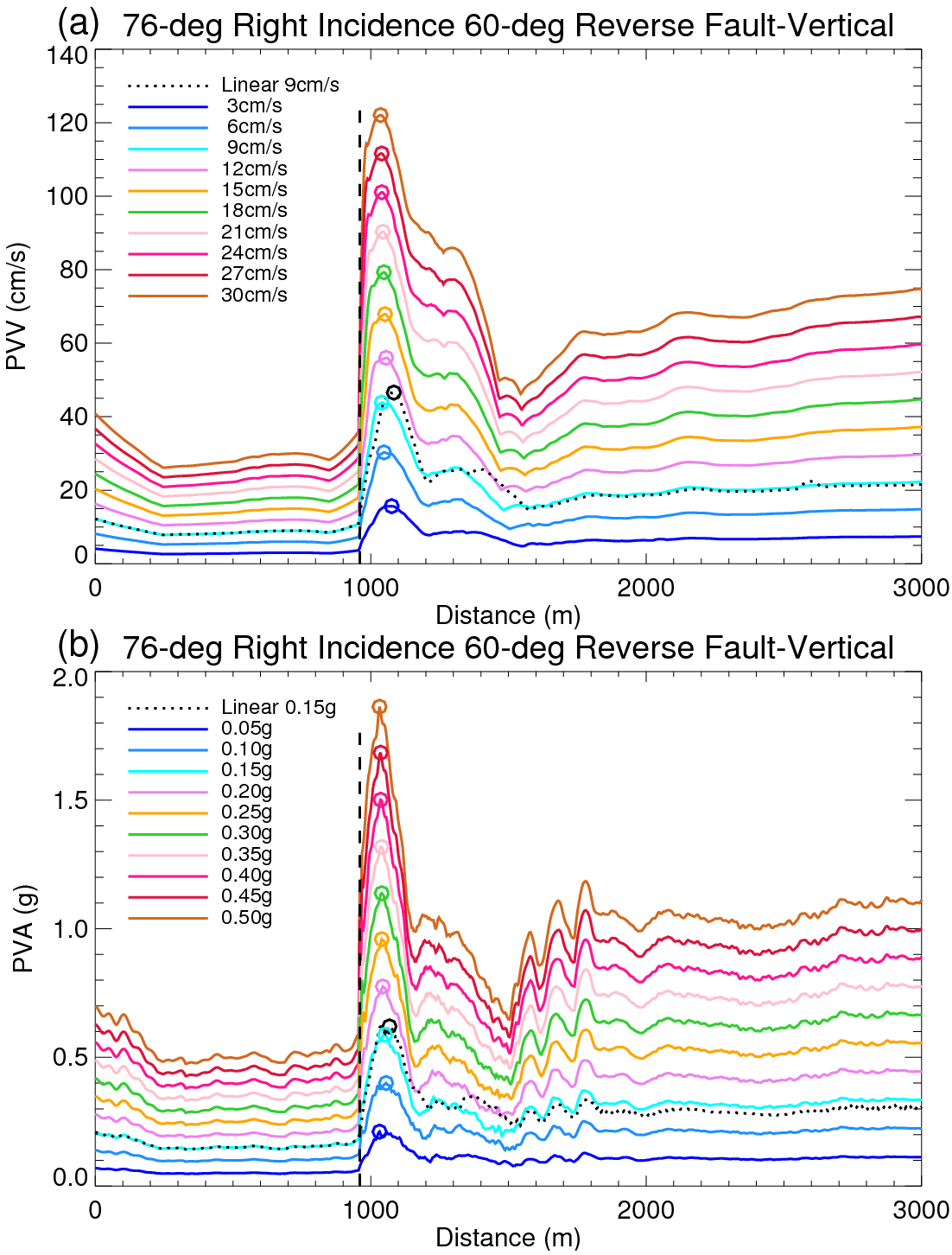

Figure 49. Incident at 76-degrees from the right with a 60-degree-dip reverse fault 2D velocity PVV (a) and PVA (b) as a function of horizontal position color-coded by corresponding uniform rock surface amplitude. The basin edge is located at 960 m as indicated by the vertical dashed lines in (a) and (b), with the basin to the right. The maximum amplitude for each input amplitude curves within or close to the basin is indicated by circles color-coded by peak input amplitude.

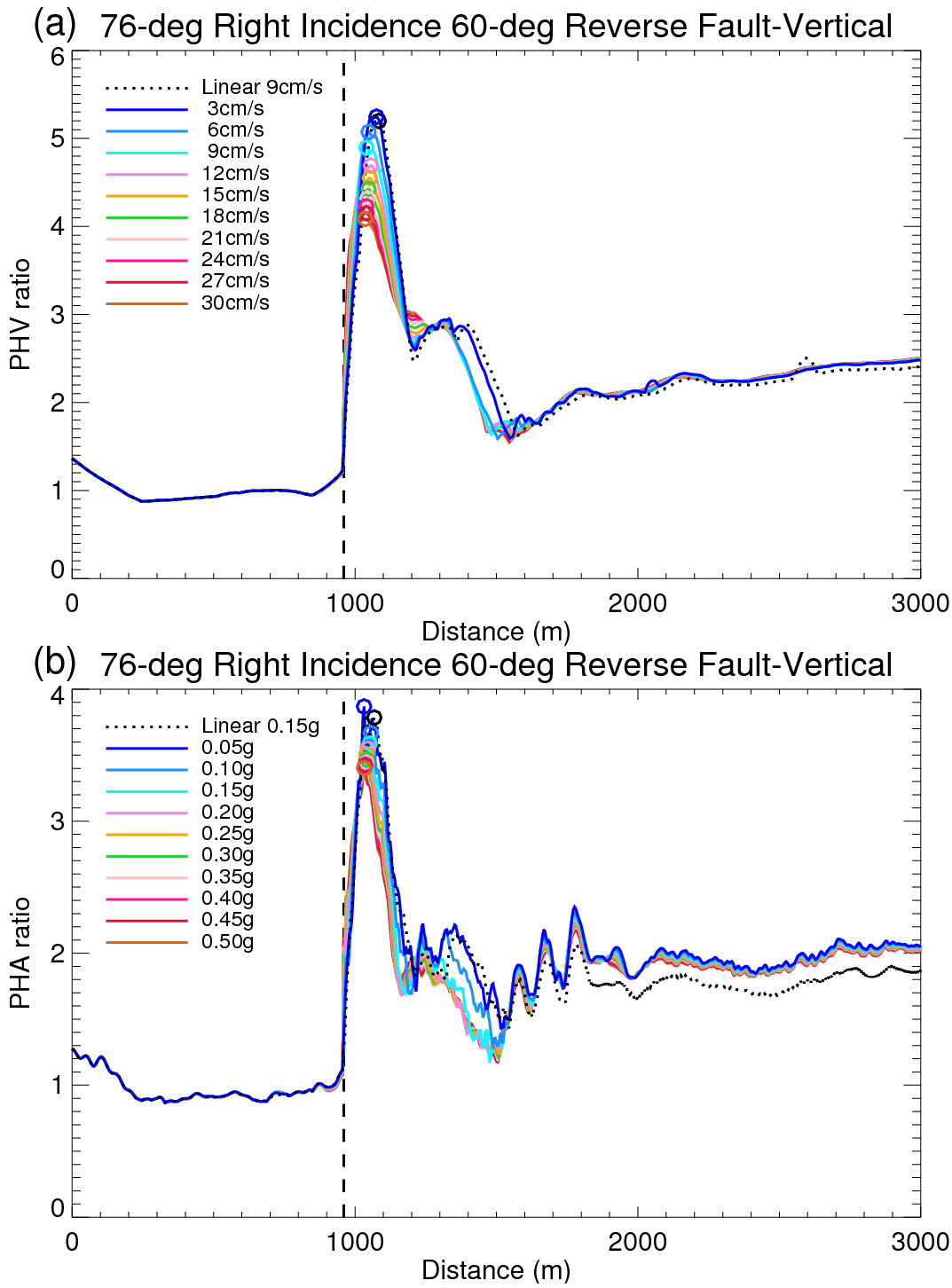

Figure 50. Incident at 76-degrees from the right with a 60-degree-dip reverse fault 2D velocity PVV ratio relative to linear rock (a) and PVA ratio relative to linear rock (b) as a function of horizontal position color-coded by corresponding uniform rock surface amplitude. The basin edge is located at 960 m as indicated by the vertical dashed lines in (a) and (b), with the basin to the right. The maximum amplitude for each input amplitude curves is indicated by circles color-coded by peak input amplitude.

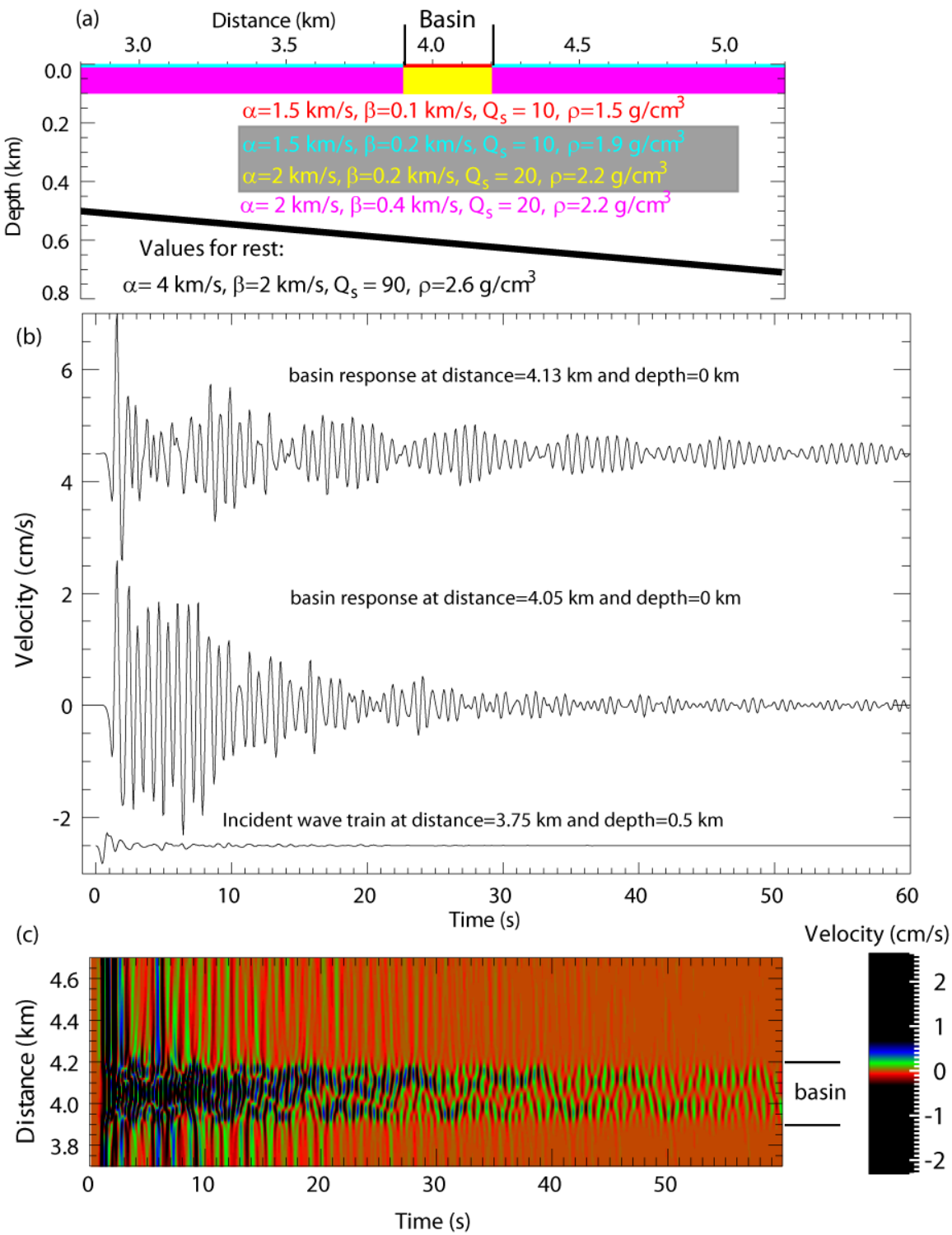

Figure 51. Color-coded Jackson Lake Dam velocity structure (a) with the thick line showing the incident SV plane wave. The incident waveform at a depth of 0.5 km modified by internal reverberations is shown at the bottom of (b) along with two surface waveforms from sites located within the basin as labeled. Color-coded horizontal velocity time histories for surface sites located at distances from 3.7 km to 4.7 km (c).

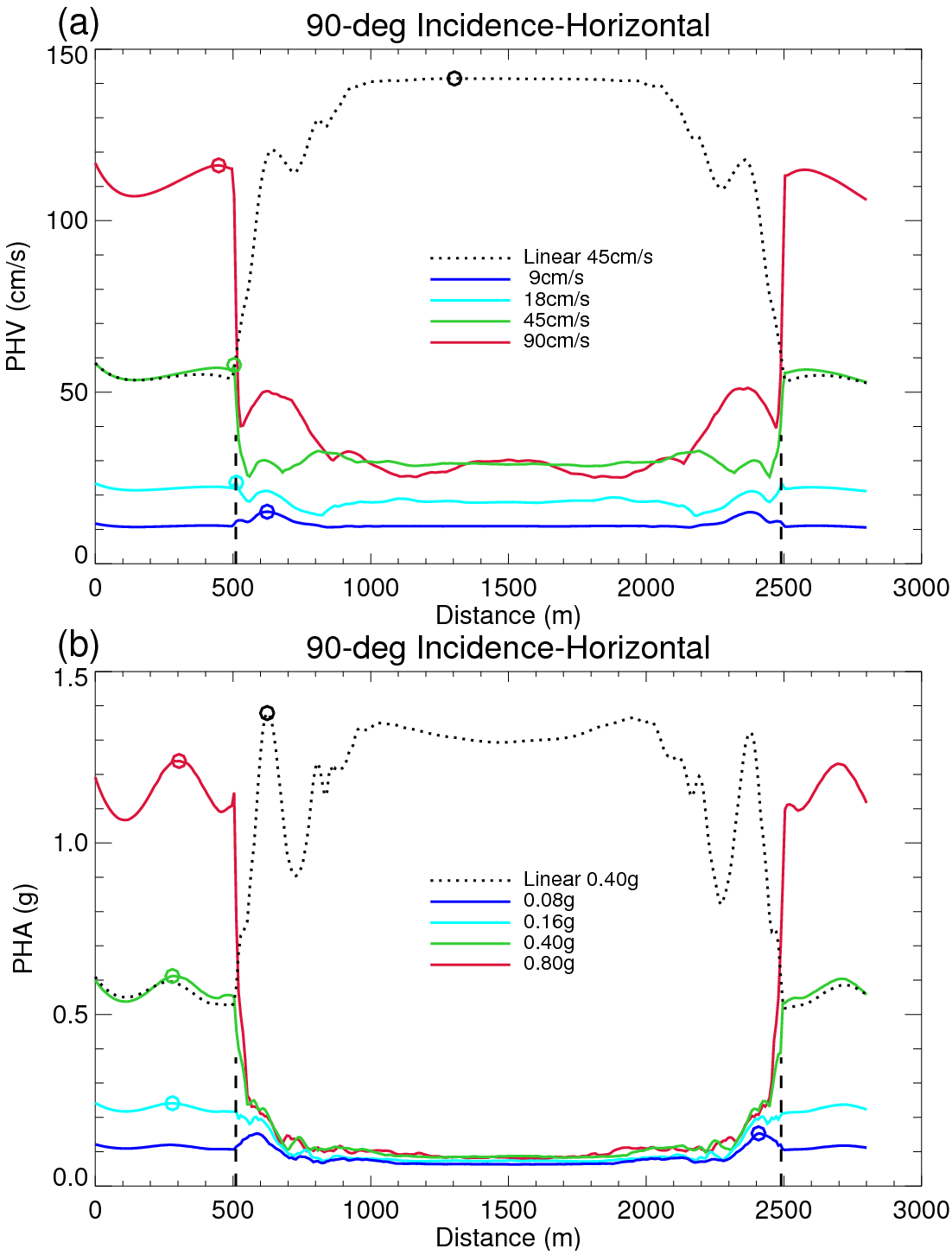

Figure 52. Horizontal peak velocities (a) and accelerations (b) for a vertically-incident P-SV plane wave as a function of incident amplitude. Short vertical dashed lines denote the margins of the low velocity basin that extends from 500 m to 2500 m distance.

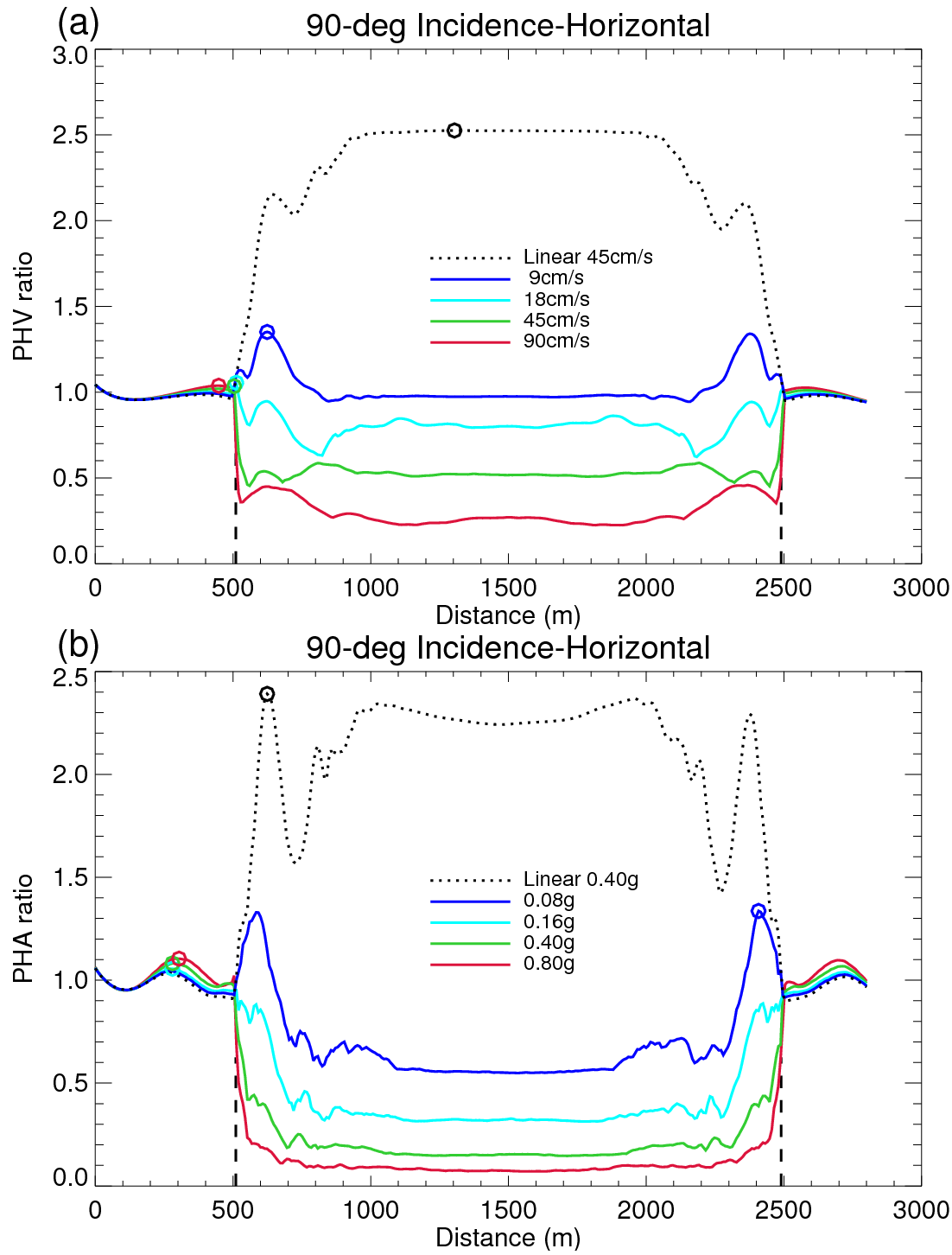

Figure 53. Horizontal peak velocity (a) and acceleration (b) ratios relative to linear homogenous rock for a vertically-incident P-SV plane wave as a function of incident amplitude. Short vertical dashed lines denote the margins of the low velocity basin that extends from 500 m to 2500 m distance.

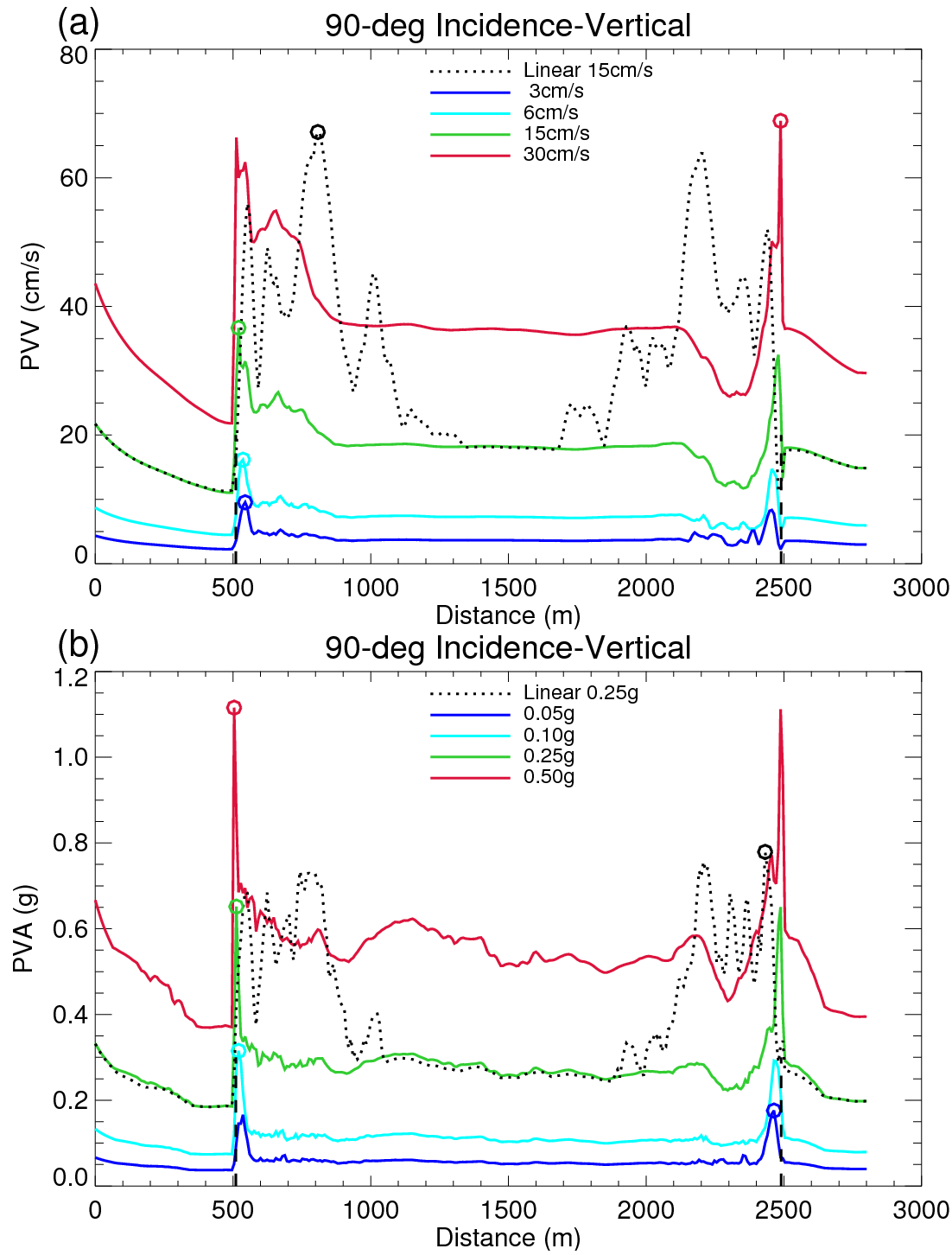

Figure 54. Vertical peak velocities (a) and accelerations (b) for a vertically-incident P-SV plane wave as a function of incident amplitude. Short vertical dashed lines denote the margins of the low velocity basin that extends from 500 m to 2500 m distance.

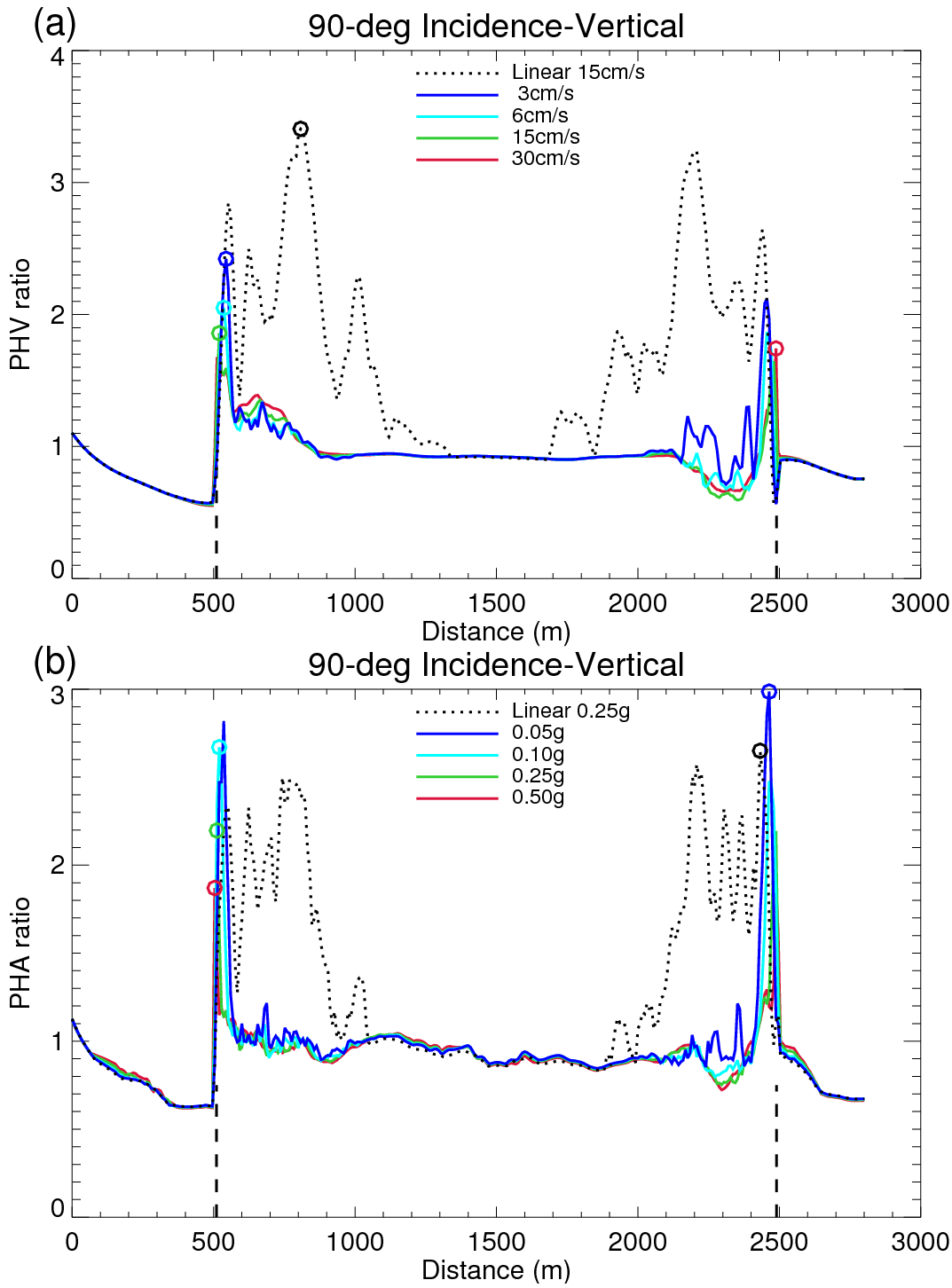

Figure 55. Vertical peak velocity (a) and acceleration (b) ratios relative to linear homogenous rock for a vertically-incident P-SV plane wave as a function of incident amplitude. Short vertical dashed lines denote the margins of the low velocity basin that extends from 500 m to 2500 m distance.

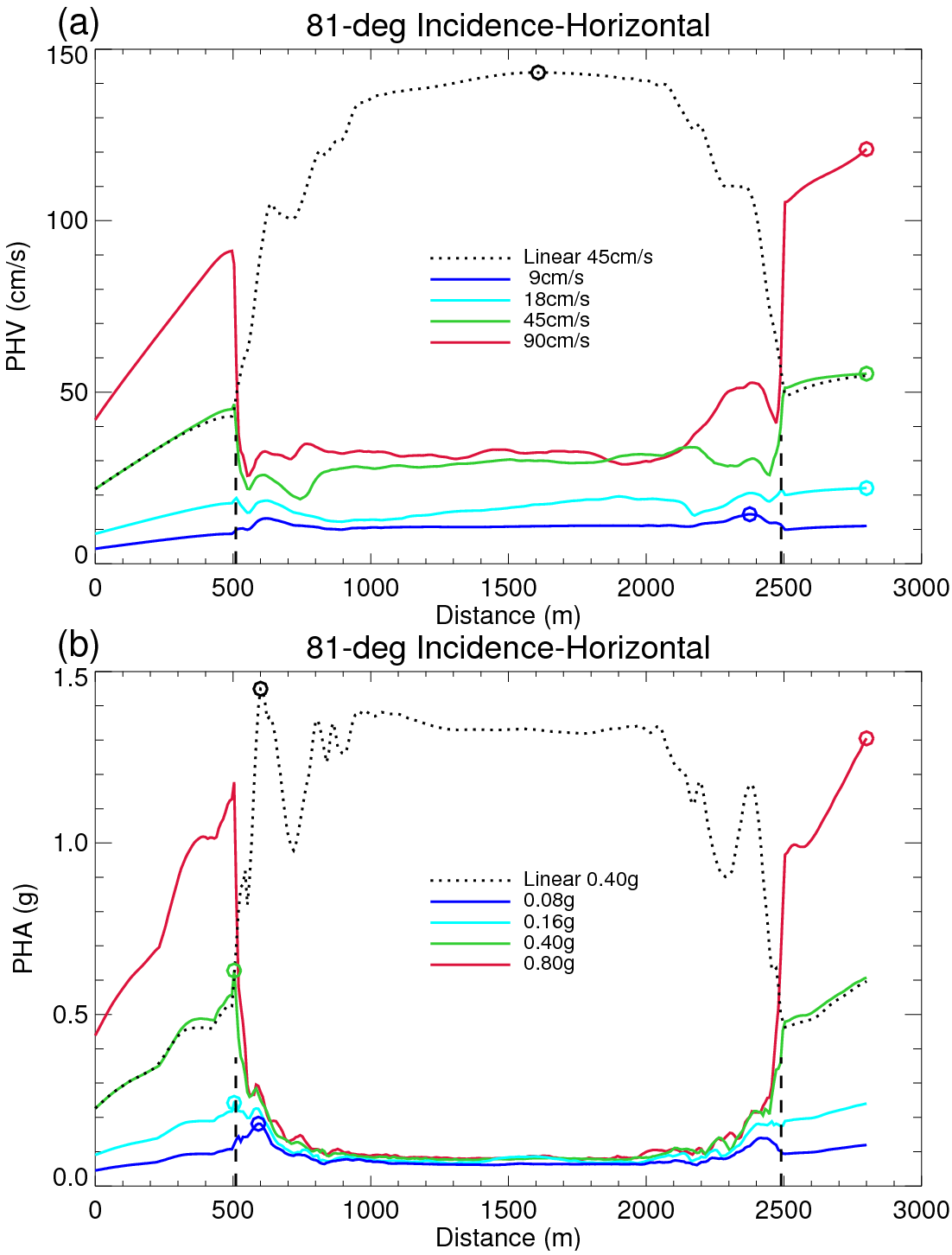

Figure 56. Horizontal peak velocities (a) and accelerations (b) for a 81-degree-incident P-SV plane wave from the left as a function of incident amplitude. Short vertical dashed lines denote the margins of the low velocity basin that extends from 500 m to 2500 m distance.

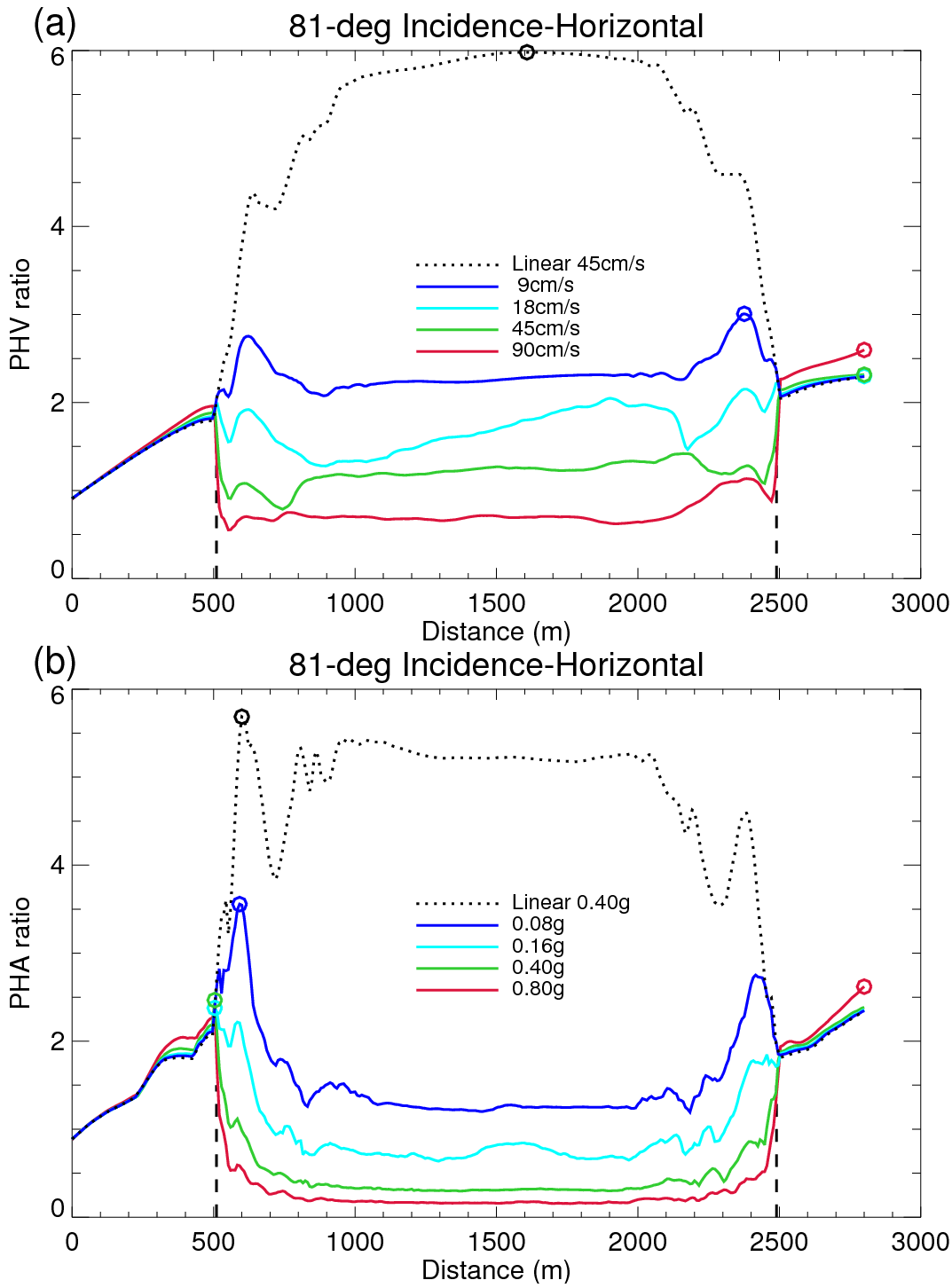

Figure 57. Horizontal peak velocity (a) and acceleration (b) ratios relative to linear homogenous rock for a 81-degree-incident P-SV plane wave from the left as a function of incident amplitude. Short vertical dashed lines denote the margins of the low velocity basin that extends from 500 m to 2500 m distance.

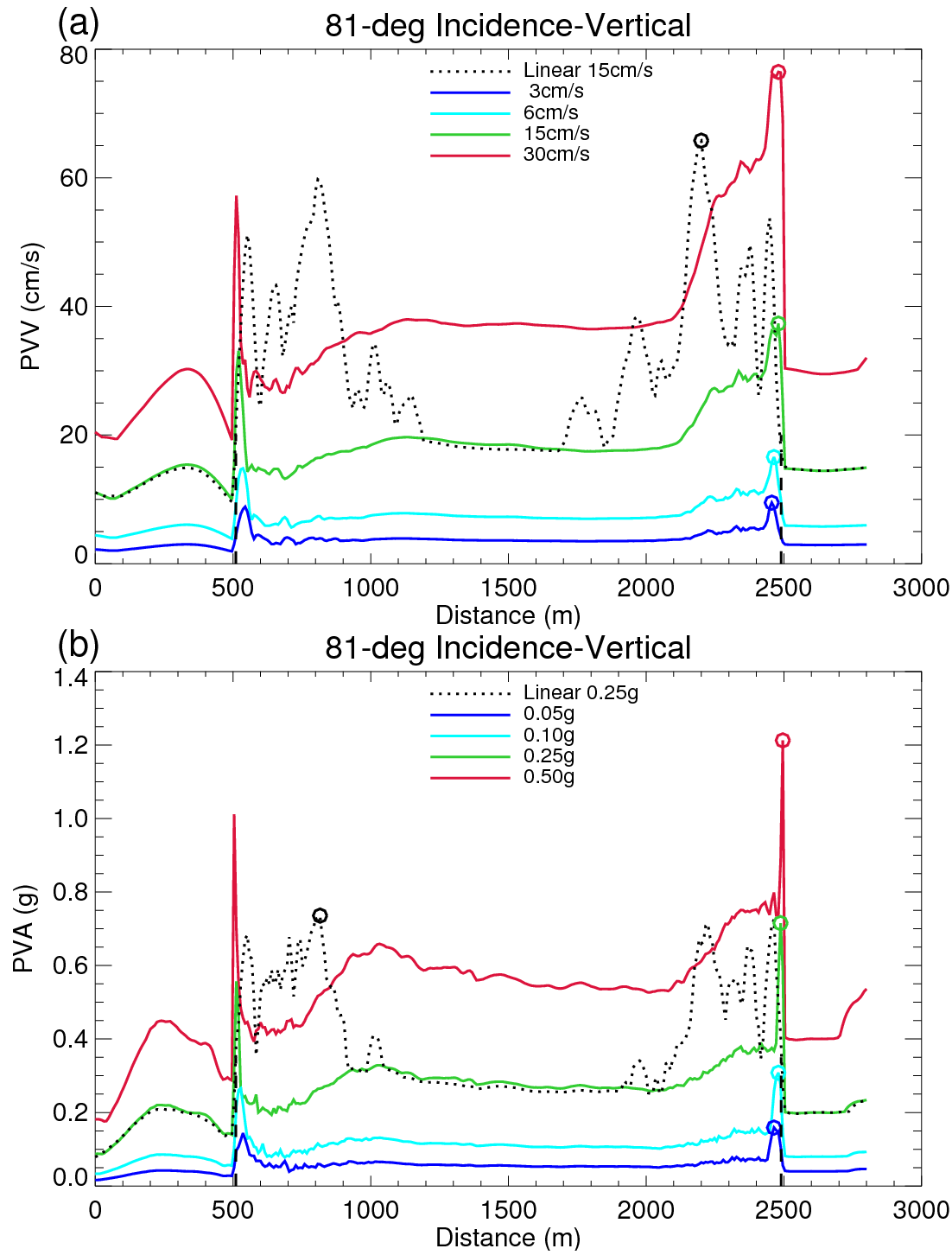

Figure 58. Vertical peak velocities (a) and accelerations (b) for a 81-degree-incident P-SV plane wave from the left as a function of incident amplitude. Short vertical dashed lines denote the margins of the low velocity basin that extends from 500 m to 2500 m distance.

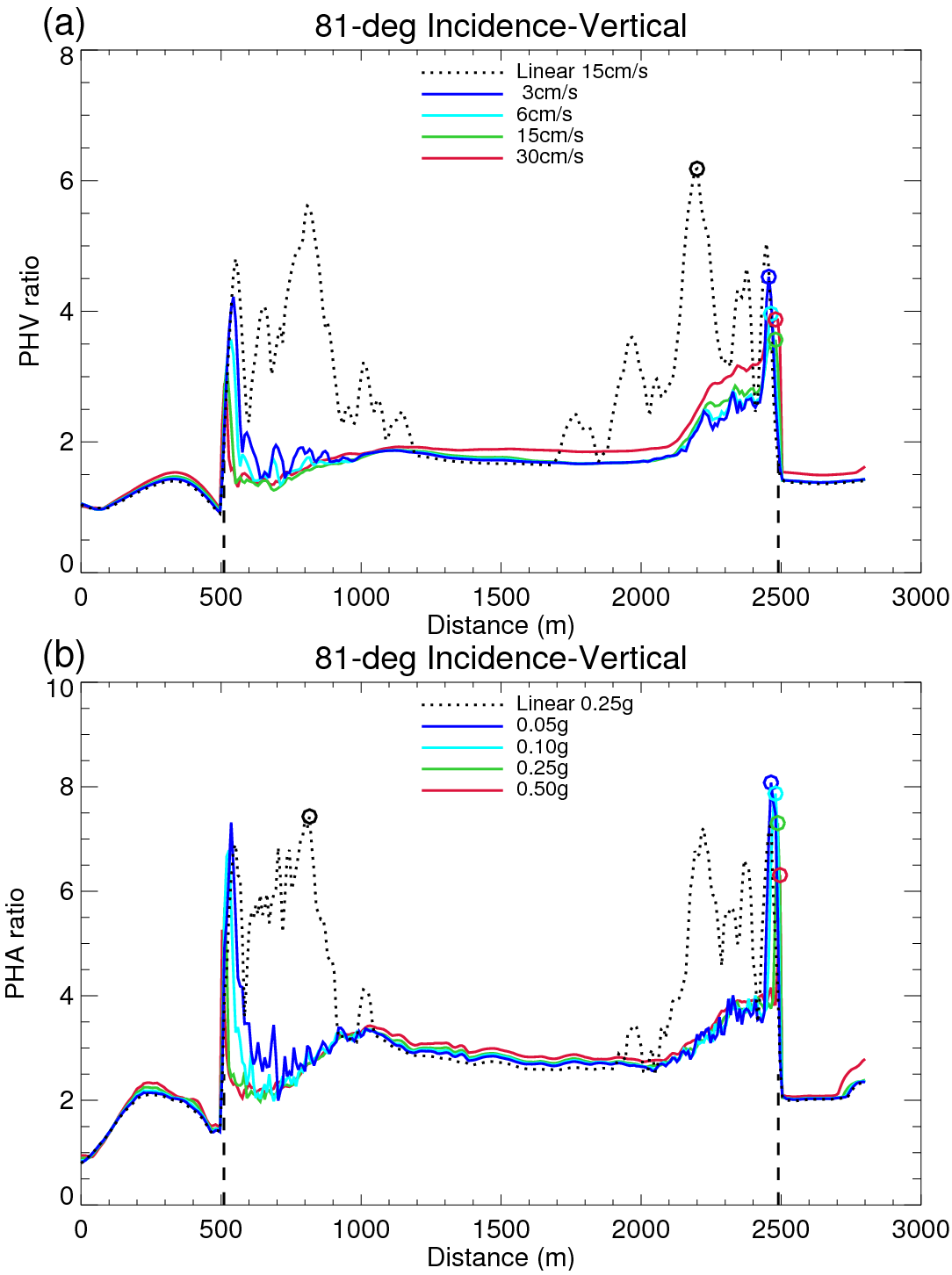

Figure 59. Vertical peak velocity (a) and acceleration (b) ratios relative to linear homogenous rock for a 81-degree-incident P-SV plane wave from the left as a function of incident amplitude. Short vertical dashed lines denote the margins of the low velocity basin that extends from 500 m to 2500 m distance.